

THE PEOPLE'S DEMOCRATIC REPUBLIC OF ALGERIA
MINISTRY OF HIGHER EDUCATION AND SCIENTIFIC RESEARCH



UNIVERSITY SAAD DAHLAB OF BLIDA 1
FACULTY OF TECHNOLOGY
DEPARTMENT OF MECHANICAL ENGINEERING

Dissertation submitted in fulfillment of the requirements
FOR THE MASTER OF SCIENCE
IN
MECHANICAL ENGINEERING
OPTION: POWER PLANTS AND TURBOMACHINERY

**Numerical Prediction of Flow Separation
in an overexpanded nozzle**

Presented by:

SINKALA Happy
HEBABCHA Abderrahmane

Defended on July 7th, 2020 before the following jury:

President: Dr. M ROUDANE	Associate Professor A	University of Blida 1
Examiner: Dr. M SAHLI	Associate Professor A	University of Blida 1
Supervisor: Prof. A BENAROUS	Professor	University of Blida 1

Dedications

I dedicate this dissertation to my family and friends.

A special feeling of gratitude to my uncle and aunt, Dominic and Lillian Chama for their love, countless sacrifices, words of encouragement and endless support. I would not have made it this far in my academic career without their constant support and reassurance that I have the ability and potential to reach greater heights.

To my late parents, George and Doreen Sinkala although they are no longer around, the memories of their love with no bounds live on.

My siblings and cousins, Precious, Ivwananji, Exildah, Robson, Vanessa, Lillian, Mapalo, Gift and pequenina Purity. This is for you too, you are an important part of my life.

To my dear friends who have supported me throughout this process in different ways. Their words of encouragement kept me going and I will always appreciate all that they have done.

To my colleagues at the University of Blida 1, Abderraouf, Abderrhamane Seman, Abderrhamane Hebabcha and Souad who have never left my side.

Last but not least I would also like to dedicate this work and give many thanks to a very special person Clean Ethel Mutale for her understanding and continual support in every way possible while asking for nothing in return.

Happy

Dedications

My deepest gratitude goes to God who has taken care of everything that would have stopped me in my tracks and strengthened me even through my most difficult times.

I am dedicating this thesis to all beloved people who have meant and continue to mean so much to me,

To my loving parents, ZOUBIR and FARIDA whose words of encouragement and push for tenacity ring in my ears.

My sister Ahlem and my brother Ryadh have never left my side and are very special,

To my colleagues at the University of Blida 1, Happy Sinkala, Abderrhamane Seman, who have never left my side,

I also dedicate this dissertation to my dear friend Walid,

I am also grateful too for my fiancée Khaoula for her endless encouragement and emotional support during the realization of this project.

Abderrahmane

Acknowledgements

We welcome this opportunity to express our sincere gratitude and appreciation to our supervisor Prof. BENAROUS Abdallah (University Saad Dahlab of Blida 01), without whose guidance, patience and support this work would not be possible. We would also like to thank NEDJARI Mohammed (University Djillali liabes of Sidi Bel Abbas) for his suggestions and remarks.

We would also like to acknowledge the Head of department, Prof. TEMMAR Mustapha and senior lecturers in the mechanical engineering department, University Saad Dahlab of Blida 01.

Abstract

A rocket engine nozzle is a propelling nozzle through which combustion gases are expanded and accelerated to supersonic velocities. For high thrust performance, the energy released by the propellants in the combustion chamber is converted into kinetic energy which leads to extremely high heat flux levels and temperature. These heat loads and temperatures may damage the nozzle wall and lead to loss in performance of the engine. Additionally, when the gases are expanded through the nozzle from subsonic to supersonic conditions, the flow undergoes many forms of unique phenomena including flow separation and its associated shock system, unsteadiness, flow mixing etc. Some of these phenomena may lead to pressure loss, thereby reduce the overall thrust generated by the nozzle. The present work aims to provide a numerical analysis of flow separation in an overexpanded nozzle and the influence of wall temperature on a free shock-induced separation and thrust performance. The numerical method used is based on a finite volume scheme where the equations of Navier-Stokes, energy and turbulence were averaged in a Favre form using Ansys-Fluent®.

Keywords: overexpanded nozzle, loss, thrust, flow separation, wall temperature, shock.

Résumé

Une tuyère d'un moteur fusé est une tuyère propulsive dans laquelle les gaz brûlés se détendent et accélérés aux vitesses supersoniques. Pour une bonne performance de poussée, l'énergie libérée à partir des propergols dans la chambre de combustion est convertie en énergie cinétique qui entraîne des flux de chaleur et températures élevés. La montée en température qui en résulte peut conduire à l'endommagement de la paroi de la tuyère et à la perte de performance. En plus, lorsque les gaz se détendent à travers la tuyère des conditions subsoniques aux conditions supersoniques, l'écoulement subit des différents phénomènes par exemple décollement, chocs, déséquilibres, mélange d'écoulement. Ces phénomènes provoquent une perte de pression ainsi que la poussée globale générée par la tuyère. Le présent travail porte l'analyse physique et la simulation numérique de l'écoulement turbulent décollé dans les tuyères supersoniques, fonctionnant en régime de surdétente et aussi l'influence de la température pariétale sur la position du point de décollement dans la tuyère et la poussée. La méthode numérique employée est basée sur un schéma de type volumes finis dont les équations de Navier-Stokes, d'énergie et de la turbulence sont moyennées au sens de Favre à l'aide du solveur Ansys-Fluent.

Mots clé : tuyère surdétendue, pertes, poussée, décollement, température pariétale, choc.

المخلص

فوهة (أنبوب متغير مساحة المقطع) محرك الصواريخ هي فوهة دافعة يتم من خلالها تمديد غازات الاحتراق وتسريعها إلى سرعات تفوق سرعة الصوت. للحصول على أداء ودفع عاليين، يتم تحويل الطاقة التي تطلقها المواد الدافعة في غرفة الاحتراق إلى طاقة حركية تؤدي إلى مستويات تدفق حرارة عالية للغاية وارتفاع درجة الحرارة. هذه الأحمال الحرارية ودرجات الحرارة قد تتلف جدار الفوهة وتؤدي إلى فقدان أداء المحرك. بالإضافة إلى ذلك، عندما يتم توسيع الغازات من خلال الفوهة من دون سرعة الصوت إلى الظروف الأسرع من الصوت، يذهب التدفق تحت العديد من الأشكال من الظواهر الفريدة بما في ذلك فصل التدفق ونظام الصدمة المرتبط به، وعدم الثبات، وخط التدفق وما إلى ذلك. قد تؤدي بعض هذه الظواهر إلى فقدان الضغط، وبالتالي تقليل الدفع الكلي الناتج عن الفوهة. يهدف العمل الحالي إلى تحليل فصل التدفق في فوهة التمدد بشكل مفرد وتأثير درجة حرارة الجدار على الفصل الحر الناتج عن الصدمة وأداء الدفع. تعتمد الطريقة العددية المستخدمة على مخطط حجم محدود حيث تم حساب متوسط معادلات *Navier-Stokes* والطاقة والاضطراب في شكل *Favre* باستخدام *Ansys-Fluent®*.

الكلمات المفتاحية: فوهة مفردة التوسيع، خسارة، دفع، فصل التدفق، درجة حرارة الجدار، الصدمة.

Table of content

Dedications	
Acknowledgements	
Abstract	
Table of content	
List of tables	
List of figures	
Nomenclature	
General introduction	1
CHAPTER I: Technological study and bibliographical analysis.....	4
1.1 Nozzle conception and manufacturing.....	4
1.2 Physics of compressible flows within nozzles.....	12
1.3 Test campaigns on nozzle flow.....	22
1.4 Numerical investigations on nozzle flow.....	25
1.5 Regenerative cooling on overexpanded nozzles.....	27
1.6 Performance losses due to shocks, separation and cooling.....	30
CHAPTER II: Modelling and governing equations.....	32
2.1 Governing equations of fluid flow.....	32
2.2 Equations of conservation in compressible flows.....	36
2.3 Thrust coefficient.....	42
2.4 Turbulence modelling (Spalart-Allmaras model).....	43
2.5 Finite volume formulation [62].....	44
2.6 Discretization schemes for convective terms (Roe) [59]:.....	50
CHAPTER III: Results and discussions.....	55
3.1 Baseline model description.....	55
3.2 Experimental operating conditions.....	57
3.3 Prediction of nozzle flow conditions.....	57
3.4 Flow regime across the nozzle.....	63
3.5 Nozzle theoretical performances.....	64
3.6 Numerical calculations.....	65
3.7 Parametric Analysis.....	80
Conclusion and perspectives.....	95
References.....	97

List of tables

Table 3.1: Geometric properties of the DRL-TIC nozzle [1].....	56
Table 3.2: Physical boundary conditions.....	67
Table 3.3: Wall pressure and shear stress values.....	78
Table 3.4: Wall thermal configurations.....	81
Table 3.5: Wall thermal configuration A.....	81
Table 3.6: Separation location.....	84
Table 3.7: Wall thermal configuration B.....	86
Table 3.8: Separation location.....	89
Table 3.9: Wall thermal configuration C.....	90
Table 3.10: Separation location.....	93

List of figures

Figure 1.1: Construction of an early regenerative cooled tubular thrust chamber [3].....	5
Figure 1.2: Definition of a supersonic nozzle [4].....	5
Figure 1.3: The principal regions of a supersonic nozzle [5].....	7
Figure 1.4: Examples of different convergent profiles [6].....	8
Figure 1.5: Initial expansion region, kernel [4].....	9
Figure 1.6.a: Basic flow structures in an ideal nozzle [4].....	10
Figure 1.6.b: Left and right running characteristics for an ideal nozzle. $M_{\text{Design}}=4.6$, $\gamma=1.2$, $L\approx 50r_t$ [4].....	10
Figure 1.7: Definition of conical nozzle [4].....	11
Figure 1.8: Left and right running characteristic lines in a truncated ideal contoured (TIC) nozzle. Obtained by truncating the ideal nozzle given in figure 1.6.b at $x/r_t\approx 18$ [4].....	11
Figure 1.9: Basic TOP nozzle geometry [4].....	12
Figure 1.10: Evolution of pressure in the nozzle [14].....	14
Figure 1.11: Ideal expanded flow [15].....	14
Figure 1.12: Underexpanded flow [15].....	15
Figure 1.13: Overexpanded flow [15].....	16
Figure 1.14: Shock induced boundary layer separation in an overexpanded nozzle, Déclery [16].....	18
Figure 1.15: Phenomenological sketch of free shock separation (FSS) [19].....	19
Figure 1.16: Shock pattern of supersonic flow with free shock separation inside an axisymmetric convergent-divergent nozzle [20].....	20
Figure 1.17: Phenomenological sketch of restricted shock separation (RSS) [19].....	20
Figure 1.18: Cap shock pattern (left) and Mach disk (right) in the plume of the Vulcain engine [4].....	24
Figure 1.19: Exhaust plume patterns for nozzles, a) truncated ideal nozzle, with Mach disk, P6 TIC DLR [1], c) TOP ONERA [19].....	24
Figure 1.20: a) Cold gas subscale test facility P6.2 and b) ONERA R2Ch blowdown wind tunnel.....	25
Figure 1.21: CFD calculated Mach number distribution in Volvo S1 nozzle [4].....	27
Figure 1.22: Cross-sections view of tubes [3].....	28
Figure 1.23: Cross-sectional view of a thrust chamber with regenerative cooling.....	28
Figure 1.24: Schematic views for dual regenerative cooling.....	29
Figure 1.25: Heat transfer schematic for regenerative cooling.....	29
Figure 2.1: Grid.....	44
Figure 2.2: v Staggered grid.....	49
Figure 3.1: Acrylic glass TIC nozzle with transducer ports [1].....	56
Figure 3.2: Geometric model for the DRL-TIC nozzle.....	56
Figure 3.3: Experimental operating conditions.....	57
Figure 3.4.a: Nozzle domain with boundary conditions.....	66
Figure 3.4.b: Computational domain and boundary conditions.....	66
Figure 3.5: 100X100 structured mesh for the nozzle.....	68
Figure 3.6: Computational domain mesh.....	68
Figure 3.7: Distribution of wall Y^+	70
Figure 3.8.a: Distribution of Mach number.....	70
Figure 3.8.b: Sketch of the Mach disc Schlieren image [1].....	71

Figure 3.9: Shock and evolution of Mach number.....	72
Figure 3.10: Axial Mach number.....	72
Figure 3.11: Evolution of static pressure on the nozzle centerline.....	73
Figure 3.12: Axial static pressure.....	74
Figure 3.13: Computed and experimental wall pressures.....	75
Figure 3.14: Radial evolution of Mach number.....	76
Figure 3.15.a: Axial velocity contours.....	77
Figure 3.15.b: Recirculation zone.....	77
Figure 3.16: Evolution of axial wall shear stress.....	78
Figure 3.17: 1D thrust coefficients for different conditions.....	80
Figure 3.18: Axial Mach number (Config.A).....	82
Figure 3.19: Mach number computed from the near wall (Config.A).....	82
Figure 3.20: Wall pressures (Config.A).....	83
Figure 3.21: Evolution of axial wall shear stress (Config.A).....	84
Figure 3.22: Recirculation zone size (Config. A).....	85
Figure 3.23: Thrust coefficient (Config.A).....	86
Figure 3.24: Axial Mach number (Config.B).....	87
Figure 3.25: Wall pressures (Config.B).....	88
Figure 3.26: Evolution of axial wall shear stress (Config.B).....	88
Figure 3.27: Thrust coefficient (Config.B).....	89
Figure 3.28: Axial Mach number (Config.C).....	90
Figure 3.29: Wall pressures (Config.C).....	91
Figure 3.30: Evolution of axial wall shear stress (Config.C).....	92
Figure 3.31: Separation location (Config.C).....	92
Figure 3.32: Recirculation zone size (Config.C).....	93
Figure 3.33: Thrust coefficient (Config.C).....	94

Nomenclature

Abbreviation

CD	: Convergent divergent
CFD	: Computational fluid dynamics
CNES	: Centre National d'Etudes Aérospatiale
DRL	: Deutsches Zentrum für Luft- und Raumfahrt, <i>German Aerospace Center</i>
ESTEC	: European Space Research and Technology Centre
FOI	: Totalförsvarets Forskningsinstitut (Swedish Defense Research Agency)
FSCD	: Flow Separation Control Device
FSS	: Free Shock Separation
FVM	: Finite Volume Method
LEA	: Laboratoire d'Etudes Aérodynamiques
MOC	: Method of Characteristic
NPR	: Nozzle Pressure Ratio
ONERA	: Office National d'Etudes et de Recherches Aérospatiales
RSS	: Restricted Shock Separation
SNECMA	: Société Nationale d'Etude et Conceptions de Moteurs Aéronautiques
SWBLI	: Shock Wave/Boundary Layer Interaction
TDK	: Two Dimensional Kinetics
TIC	: Truncated Ideal Contour
TOC	: Thrust Optimized Contour
TOP	: Thrust Optimized Parabolic

Symbols

a	: Speed of sound	[m/s]
A	: Section area	[m ²]

c_p	: Specific heat at constant pressure	[J/kg.K]
C_f	: Friction coefficient	
C_F	: Thrust coefficient	
e	: Internal energy (per unit mass)	[J/kg]
F	: Thrust force	[N]
f	: body weight, damping function	[N]
h	: Specific enthalpy	[J/kg.K]
I	: Origin of interaction	
L	: Length	[mm]
M	: Mach number, molar mass	[mole/kg]
\dot{m}	: Mass flow rate	
p	: Pressure	[Bar]
q	: Heat flux	[W/m ²]
R	: Universal gas constant	[J/mol.K]
r	: radius, specific gas constant	[mm], [J/kg.K]
Re	: Reynolds number	
T	: Temperature	[K]
V	: Velocity vector of u, v, w components in x, y, z directions	
\tilde{V}	: Control volume	
y^+	: Non – dimensional distance from the 1st wall – adjacent grid point to the wall	

Greek symbols

μ_t	: Turbulent viscosity	[kg/m.s]
\emptyset	: Diameter	[mm]
γ	: Isentropic ratio	
ε	: Area ratio	
ρ	: Density	[kg/m ³]

μ	: Dynamic viscosity [kg/m.s]
τ_w	: Wall shear stress [N/m ²]
ϑ	: Kinematic viscosity [kg/m.s]
δ	: Displacement thickness [mm]

Indices

c	: Chamber
cv	: Convergent
div	: Divergent
in	: Inlet
0	: Stagnation conditions
I	: Start of interaction.
i	: Incident flow
r	: Recirculation
s	: Separation
t	: Throat
(*)	: Sonic conditions
e	: Exit
a	: Ambient
p	: Plateau
aw	: Adiabatic wall
wg	: Wall gas side
w	: Wall

General introduction

Introduction

The Convergent Divergent (CD) nozzle is a major design configuration within a jet propulsion system that plays a vital role for a vehicle operating under supersonic conditions. It is used in many applications in the aerospace industry, including high-speed military and combat jets, rocket nozzles and missiles. The traditional CD nozzle is a relatively simple device used commonly among most jets and rocket nozzles.

In a liquid propellant rocket engine, the energy released by the propellants is contained inside the thrust chamber and accelerated through the nozzle to extract the thrust. This normally leads to higher pressures in the combustion chamber and therefore higher thermal loads in the engine. Extremely high heat flux levels and temperature gradients are present not only in the immediate vicinity of the injector head, but also in the nozzle region. These heat loads and temperatures in rocket nozzles are significantly above the material failure limit of recent available materials. Therefore, efficient cooling methods are necessary in order to reduce thermal loads and insure reliability of rocket engines. Different cooling techniques such as, regenerative cooling, radiation cooling, film cooling, transpiration cooling and ablation have led to improvements in thrust chamber thermal protection. Regenerative and film cooling technology are the most favorable thermal protection methods used in the cooling of the divergent section of rocket nozzles.

In addition, when the gas is expanded through a CD nozzle supersonically, the flow undergoes many forms of unique phenomena, including flow separation, unsteadiness, flow mixing, turbulence, shock-induced boundary layer separation and Mach Shock Diamonds. Some of these phenomena lead to energy loss, thereby reducing the overall thrust generated by the nozzle. The thrust loss due to shock waves and boundary layer separations generated internally in the nozzle region still remains a major challenge in the field of aerospace sciences.

General introduction

Other than thermal protection, cooling of the divergent section of rocket nozzles may improve engine performance in that it can also be used to control flow separation and providing thrust in the high Mach number domain.

Problem Statement

In this present work, we develop a series of CFD simulation scenarios to investigate flow dynamics in an axisymmetric overexpanded rocket nozzle with respect to prediction of flow separation and the influence of cooling of the nozzle wall on a free shock-induced separation through the analysis of wall temperature properties. Of interest is the location of the separation, recirculation zone size and thrust performance, C_F .

Methodology

The key parameter of interest in this present work is the thrust force provided by the nozzle part of the propulsive chamber, under different conditions. To do this, different approaches to the problem are employed.

First, a theoretical approach is taken where the flow is considered to be a quasi-one-dimensional. Carrying out thermodynamic calculations using basic gas dynamics equations, operating parameters and ideal nozzle performance (C_F), are determined.

Secondly, the system of equations governing the flow is solved on the model [1] using the finite volume method (FVM) in structured grid. The governing equations are averaged in a Favre form using Ansys-Fluent® [2] as the solver. In this approach, the boundary layer and turbulence effects are not ignored. To provide a reference datum to check the influence of wall temperature on flow dynamics in overexpanded nozzles, a fully adiabatic nozzle wall is first studied in the case of model validation.

The third approach consists of computational fluid dynamics (CFD) scenarios with wall cooling in the presence of a free shock-induced separation. In this case, the divergent section of the nozzle wall or part of the wall is treated as isothermal with a fixed wall temperature T_w . Finally, the numerical results are studied and analyzed in terms of flow separation and thrust efficiency.

General introduction

Organization of manuscript

The present document is organized in three (03) chapters.

The first chapter is dedicated to a technological study and biographical analysis of nozzle design and compressible flow theory. Focusing mainly on overexpanded nozzles and the physical phenomenon encountered in such nozzles, that is, flow separation and its associated shock system. In addition, experimental campaigns and numerical studies performed on nozzle flow are provided. Regenerative cooling as one of the most widely used cooling technique in nozzles is explained. Finally, losses in performance due to flow separation, shocks and cooling are outlined.

Chapter 2 covers the governing equations of fluid flow on which the simulations in this numerical work are based.

Chapter 3 covers the main objective of the present work. It provides a discussion of the obtained results from the computational work. First, thermodynamic calculations are carried out to predict the flow conditions and estimate the ideal performance of the nozzle under the given conditions. Then CFD simulations are run on the DRL-TIC nozzle model and a comparative study is carried out where the obtained results are compared with the experimental data [1] for validation. The last part of the work consists of series of simulation scenarios with different wall configurations (modification of wall boundary conditions) of the divergent section of the nozzle wall. The numerical results are then discussed and analyzed to check the influence of the wall cooling on flow dynamics and nozzle performance.

Finally, conclusions, as well as perspectives are recapitulated at the end of this thesis.

CHAPTER I: Technological study and bibliographical analysis

Introduction

Extensive studies have been done through the years to understand flow separation phenomena in overexpanded rocket nozzles. A better understanding could lead to better prevention or control of flow separation. This chapter is dedicated to the study of the physical phenomena related to boundary layer separation and separation criteria characterized by the evolution of wall pressure in the separation zone. This study requires basic knowledge of nozzle design as the internal flow field determines the characteristics of the nozzle flow behavior and performance, and compressible flows in nozzles with respect to shock formation and operating regimes (adaptation, underexpansion and overexpansion). Included in this chapter is regenerative cooling technique which is the most commonly used technique in cooling of the divergent section of the nozzle wall. Finally, losses of performance due to separation, cooling and shocks are outlined.

1.1 Nozzle conception and manufacturing

Thrust chambers are an essential subassembly of liquid propellant rocket engines. In the thrust chamber, liquid propellants are metered, injected, atomized, vaporized, mixed, and burned to form hot reaction gaseous products, which are subsequently accelerated and ejected at supersonic velocities. Chamber assemblies (Fig.1.1) comprise one or more *injectors*, a *combustion chamber*, a *supersonic nozzle*, and various *mounting provisions*.

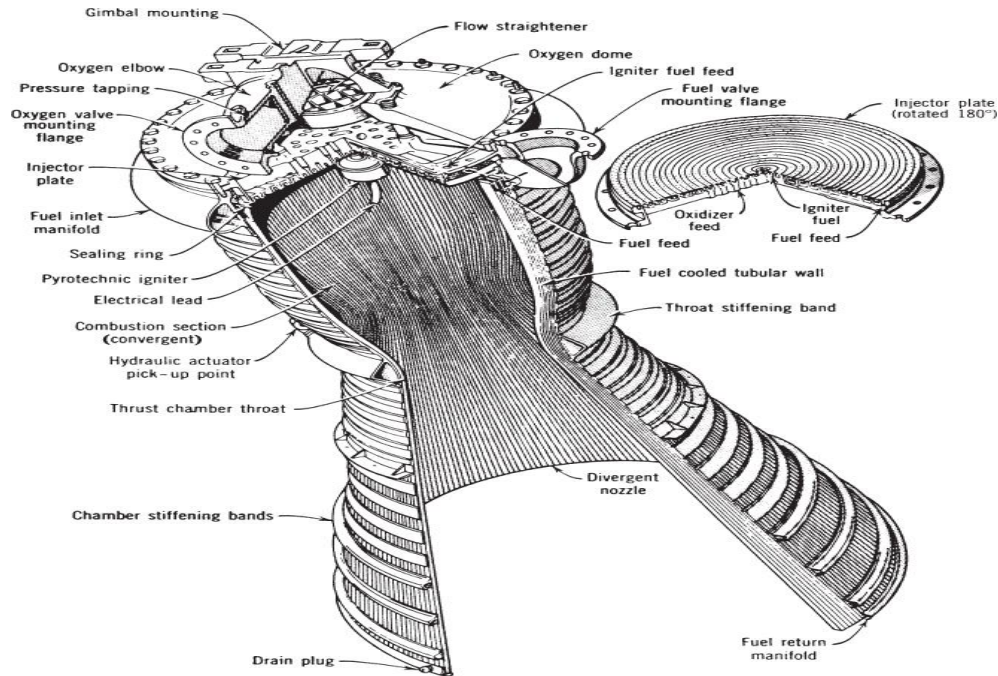


Figure 1.1: Construction of an early regenerative cooled tubular thrust chamber [3]

Typically, the combustion chamber is a constant diameter duct into which propellants are injected, mixed and burned. Its length is sufficient to allow complete combustion of the propellants before the nozzle accelerates the gas products. The *nozzle* is said to begin at the point where the chamber diameter begins to decrease. The flow area is first reduced giving a subsonic (Mach number < 1) acceleration of the gas. The area decreases until the minimum or throat area is reached. Here the gas velocity corresponds to a Mach number of one. Then the nozzle accelerates the flow supersonically (Mach number > 1) by providing a path of increasing flow area.

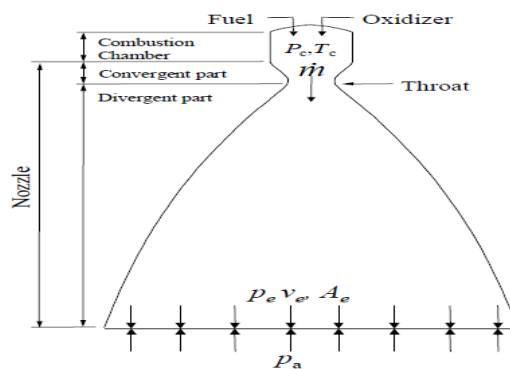


Figure 1.2: Definition of a supersonic nozzle [4]

CHAPTER I: Technological study and bibliographical analysis

Simply stated, the role of the supersonic nozzle is to use the low velocity, high pressure, and high temperature gas in the combustion chamber, to increase *thrust* by accelerating the combustion gas to a high supersonic velocity.

$$\text{Steady thrust; } F = \dot{m}v_e + (p_e - p_a)A_e = C_F p_c A_t = \dot{m}I_{sp} \quad (1.1)$$

Where \dot{m} is the engine mass flow rate, C_F is the thrust coefficient (dimensionless) and I_{sp} the specific impulse [m/s]. v_e and p_e are average values of the velocity and pressure over the nozzle exit area.

C_F gives the amplification of the thrust due to the gas expansion in the rocket nozzle compared to the thrust that would have been obtained if the chamber pressure only acted over the throat area only.

The specific impulse I_{sp} is a measure of how efficiently a given flow rate of propellant is turned into thrust.

$$\text{Specific impulse; } I_{sp} = F / \dot{m} \quad (1.2)$$

Another fundamental parameter that is frequently used in nozzle design and theory is the expansion ratio i.e. the ratio of the exit cross-sectional area to the throat cross-sectional area:

$$\text{Area ratio; } \mathcal{E} = \frac{A_e}{A_t} \quad (1.3)$$

If one assumes that the flow in a rocket nozzle is one-dimensional and isentropic, then the only important geometric variable is the area ratio. However, real nozzle flows are never truly one-dimensional, and the shape of the nozzle walls can be quite important. The design of an actual nozzle requires the specification of the entire nozzle shape and generally takes into account variations in velocity and pressure on surfaces normal to the streamlines. In addition, the influence of friction, heat transfer, composition change, or shocks must be considered.

Traditionally, the supersonic nozzle is divided into two (2) parts (Fig.1.2), the subsonic portion called the convergent and supersonic portion called the divergent. However, in supersonic nozzle

design, the conventional two-dimensional nozzle is usually considered to consist of several regions as shown in figure 1.3. These are;

- i. the contraction or convergent, in which the flow is entirely subsonic,
- ii. the throat region, in which the flow accelerates from a high subsonic to a low supersonic speed,
- iii. an initial expansion region, where the slope of the contour increases up to its maximum value,
- iv. the straightening or 'Buseman' region in which the cross sectional area increases but the wall slope decreases to zero, and
- v. the test section, where the flow is uniform and parallel to the axis.

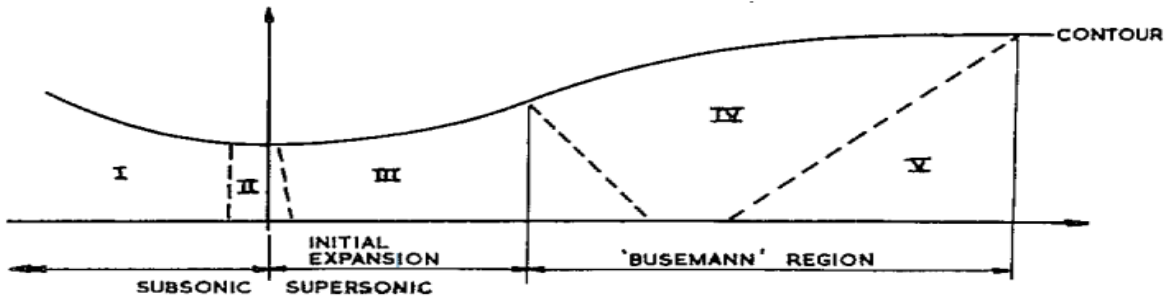


Figure 1.3: The principal regions of a supersonic nozzle [5]

In supersonic flow, the Euler equations are hyperbolic i.e. the flow is only determined by the upstream conditions. In this case the method of characteristics (MOC) can be used to calculate the nozzle flow field. This method is the most commonly used in the rocket nozzle society for generating nozzle contours and determining loads and performances.

1.1.1 Convergent region

To date, very little consideration has been given to the flow in the subsonic part of the nozzle and the wall shape is usually prescribed by any convenient smooth curve. The reasonable flow uniformity achieved with nozzles designed on this basis seems to indicate that the precise shape of the wall is not of great importance, excepting of course the region immediately upstream of the throat. However, adverse pressure gradients should be avoided as far as possible because these may be strong enough to provoke separation of the boundary layers, and although

reattachment is likely to occur upstream of the throat, there is the possibility of non-uniformity of the flow downstream of the throat. Hence, it is important to consider the shape of the wall near the throat. Otherwise, in a region of favorable pressure gradient, almost any reasonably smooth contour provides a good subsonic flow.

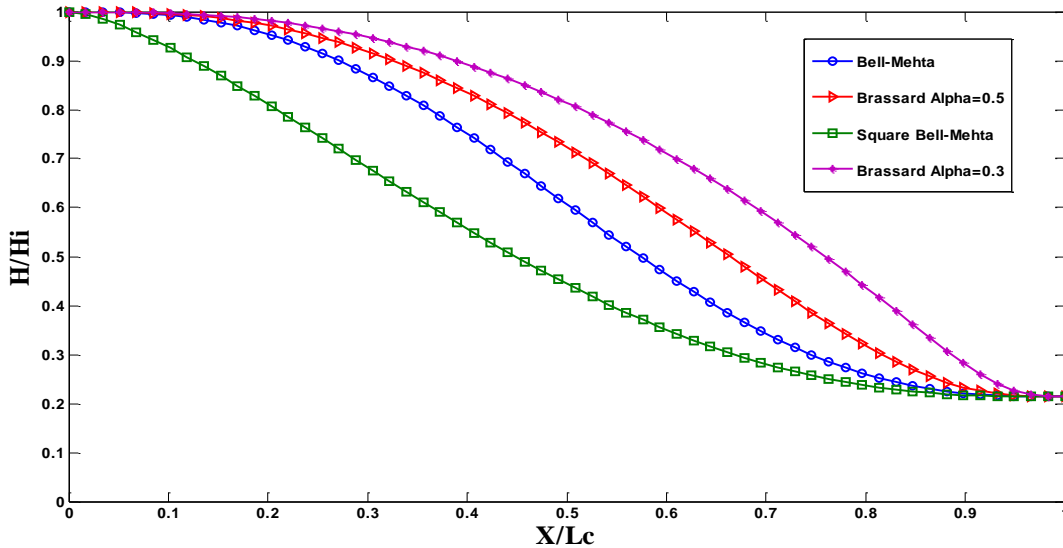


Figure 1.4: Examples of different convergent profiles [6]

1.1.2 Throat region

For the throat, quite a number of design methods have assumed for convenience that the flow is sonic along a straight line normal to the nozzle axis at the throat. Bershader [7] (1949) had shown that this assumption is only valid when the curvature of the wall at the throat is zero. Although this is possible it is difficult to realize in practice. If the curvature were zero any small error in the boundary layer correction would be sufficient to cause a substantial movement of the effective throat.

1.1.3 Initial expansion region

In a nozzle, the initial expansion occurs along contour TN (Fig.1.5), and this determines the character of the downstream flow field. In rocket application, a sharp corner downstream the throat are generally avoided due to chemical kinetics effects. Basically, a wall contour TN

having a radius of curvature equal to 0.5 times the throat radius i.e. $r_{td}=0.5r_t$, are widely used. Using a transonic-flow analysis, a constant Mach-number line TO can be defined at the throat. Given the flow condition along TO and the solid boundary TN, a kernel flow field TNKO can be generated with the method of characteristics. The flow in the kernel is entirely determined by the throat conditions and constitutes the expansion zone. This kernel is the basis in all MOC design methods.

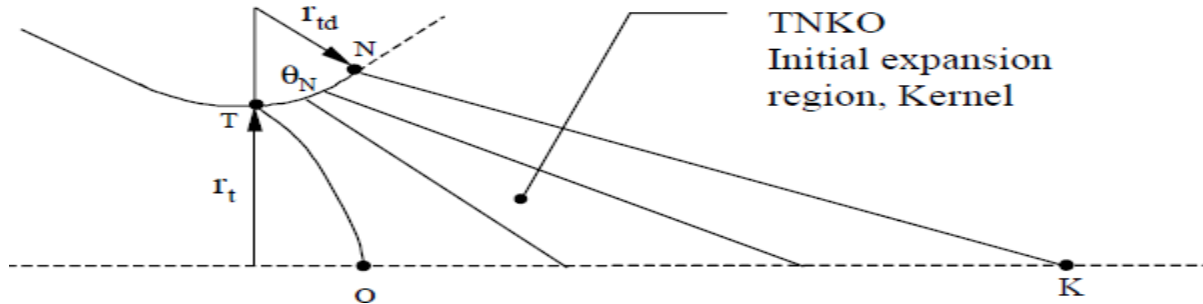


Figure 1.5: Initial expansion region, kernel [4]

1.1.4 Divergent region

As stated, the exact shape of the subsonic or converging portion of the nozzle is not, within limits, a matter of great importance. On the other hand, the shape of the supersonic or diverging portion of the nozzle is important since, even in the absence of boundary layer effects, improper shaping can result in shock formation and substantial performance loss.

Consider the basic flow structure in an ideal nozzle shown in figure 1.6.a. Basically, an ideal nozzle is a nozzle that produces uniform exit flow conditions. The nozzle contour, which achieves this, can be designed with MOC.

Contour TNE is the diverging portion of the nozzle. After the initial expansion TN, the contour NE turns the flow over to axial direction. TN also defines the Mach number at K, which is equal to the design Mach number obtained at the exit. With the Mach line NK defined it is possible to construct the streamline between N and E with the use of MOC which patches the flow to become uniform and parallel at the exit and thus complete the nozzle design. Figure 1.6.b shows the left and right running characteristics for an ideal nozzle. The design Mach number is $M=4.6$

and the gas properties are $\gamma=1.2$ with a molecular mass =13.63 g/mole. The Two-Dimensional Kinetics nozzle performance code (TDK) can be used to generate the starting line TO.

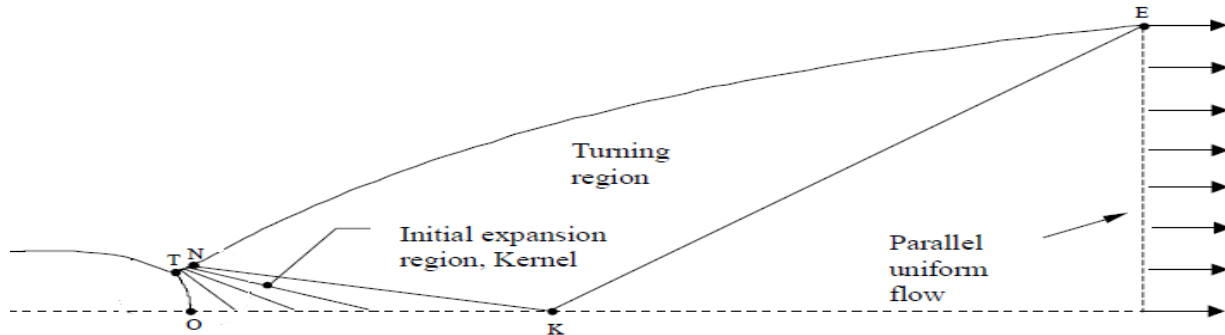


Figure 1.6.a: Basic flow structures in an ideal nozzle [4]

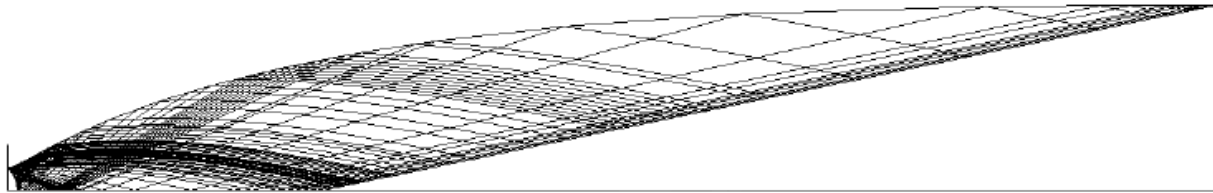


Figure 1.6.b: Left and right running characteristics for an ideal nozzle. $M_{Design}=4.6$, $\gamma=1.2$, $L \approx 50r_t$ [4]

1.1.5 Different types of nozzle contours.

Different types of conventional convergent-divergent rocket nozzles exist, each producing their own specific internal flow field. Before analyzing flow separation behavior it is essential to understand the features of the different contour types.

1.1.5.1 Conical contour nozzles

The first rocket engine nozzles were typically conical in shape as this made for easier design and manufacturing [8]. The exhaust velocity of a conical nozzle is essentially equal to the one-dimensional value corresponding to the expansion ratio, with the exception that the flow directions are not all axial. Hence, there is a performance loss due to the flow divergence. Due to its high divergence or geometrical losses, the conical nozzle is nowadays mainly used for solid rocket boosters with small expansion ratios and small thrusters where simple fabrication methods

are preferred. Nevertheless, a 15° conical nozzle is often used as a reference in comparing lengths and performance of other types of nozzles.

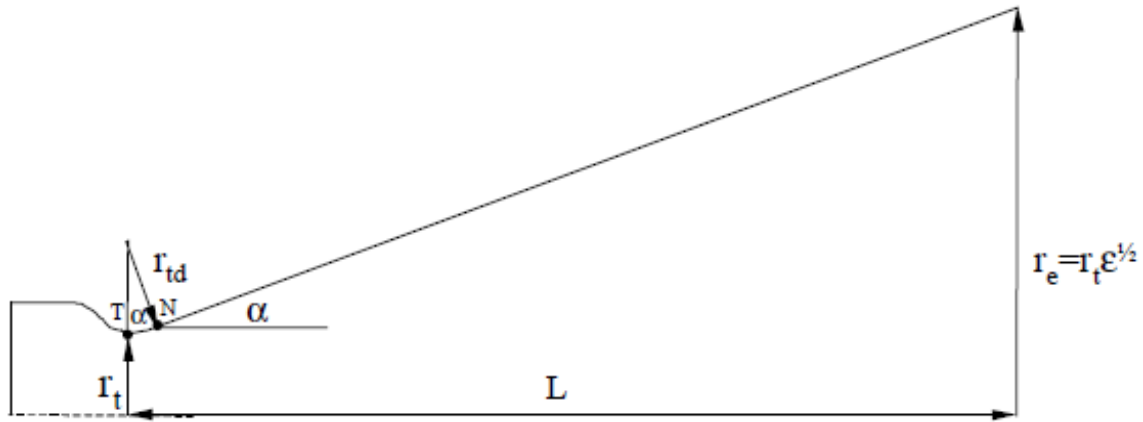


Figure 1.7: Definition of conical nozzle [4]

1.1.5.2 Truncated ideal contoured (TIC) nozzles

An “ideal” nozzle contour (Fig.1.6.a) can be created with the aid of method of characteristics (MOC). These contours provide an isentropic and shock-free supersonic gas expansion with a uniform exit velocity profile. However, these nozzles are extremely long and consequently heavy and difficult to install [9]. The huge length is necessary to produce a one-dimensional exhaust profile. However, the thrust contribution of the last part of the contour is negligible due to the small wall slopes. Shortening such a nozzle proves to be a good way to reduce weight without suffering significant thrust losses; these nozzles are called truncated ideal contoured nozzles, or TIC nozzles. As an example, the right and left running characteristics of a truncated ideal nozzle obtained by truncating the ideal nozzle given in figure 1.6.b are shown in the figure below.

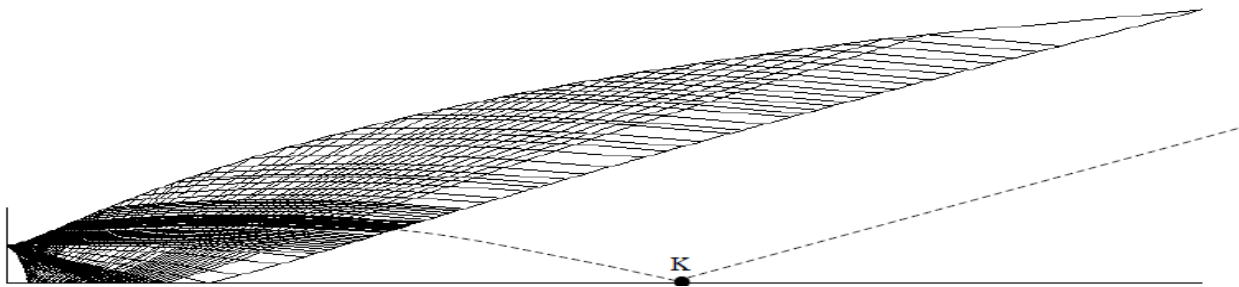


Figure 1.8: Left and right running characteristic lines in a truncated ideal contoured (TIC) nozzle. Obtained by truncating the ideal nozzle given in figure 1.6.b at $x/r_t \approx 18$ [4]

1.1.5.3 Thrust optimized parabolic (TOP) nozzles

Guderley and Hantsch [10] formulated the problem of finding the exit area and nozzle contour by using calculus of variables to produce the optimum thrust for prescribed values of the nozzle length and the ambient pressure. However, the method was not widely adopted until the complicated solution method was simplified significantly by Rao [11]. These nozzles, usually referred to as thrust optimized contoured nozzles (TOC), significantly increased geometrical efficiency compared to a 15° half angle conical nozzle with the same expansion ratio. Rao later proposed a skewed parabolic-geometry approximation to TOC nozzle contour from the inflection point to the nozzle exit [12], referred to as thrust optimized parabolic (TOP) nozzles. The TOC nozzle produces weak compression waves along the wall which coalesce into an internal shock wave further away from the wall. In comparison, TOP nozzles produce an internal shock at the wall due to a discontinuity formed at the intersection between a circular arc at the throat and the parabolic curve that defines the rest of the divergent section. Interestingly, this leads to increased wall pressure in TOP nozzles compared to TOC nozzles, giving TOP nozzles a higher resistance to flow separation [9]. TOP nozzles are commonly used on rocket engines and were employed on the American Space Shuttle Main Engine and the European Vulcain engine [9].

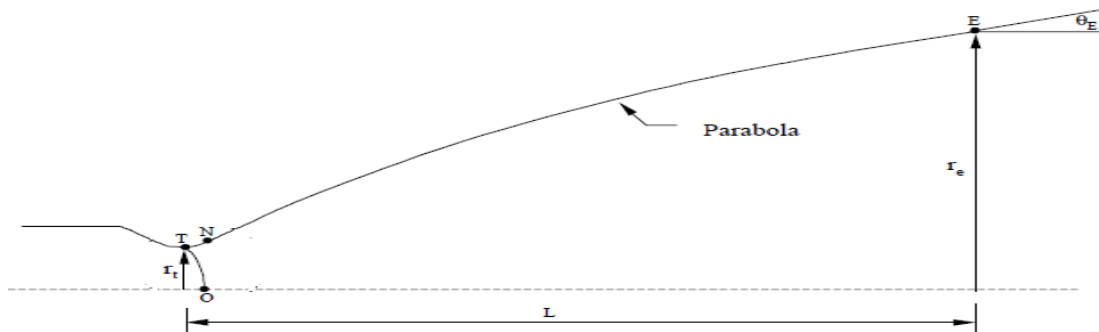


Figure 1.9: Basic TOP nozzle geometry [4]

1.2 Physics of compressible flows within nozzles

As shown in the previous section, the performance of rocket engines highly depends on the aerodynamic design of the expansion nozzle, the main design parameters being contours design and the area ratio.

CHAPTER I: Technological study and bibliographical analysis

Anderson demonstrates in his book *Modern Compressible Flow with Historical Perspective* [13], the following equation can be derived from quasi one-dimensional flow equations:

$$dA/A = (M^2 - 1) du/u \quad (1.4)$$

This equation called the area-velocity relation tells that for $M > 1$ i.e. supersonic flow, an *increase* in velocity is associated with an *increase* in area, and vice versa. Hence an obvious way to increase the payload of propulsion systems would be to increase the area ratio of the core nozzle engine, however this will at the same time reduce the nozzle exit pressure.

1.2.1 Flow conditions in nozzles

Flow conditions in supersonic nozzles are determined by the *operating pressure ratio*, the ratio of the ambient pressure to the inlet stagnation pressure. Figure 1.10 shows the evolution of the pressure along the nozzle. The first critical point corresponds to the case where the throat becomes sonic, and the mass flux reaches a maximum. The nozzle flow is subsonic, including the exit jet, and $p_e = p_a$. The pressure ratio above the first critical, the exit jet is subsonic and the nozzle throat is not choked while below this critical the diverging flow is entirely supersonic, including the jet flow. A nozzle operating at the *design pressure ratio*, the exit pressure is equal to the surrounding pressure ($p_e = p_a$). Further lowering the pressure ratio would result in the formation of internal shocks, overexpanded flow or underexpanded flow depending on the operating pressure ratio.

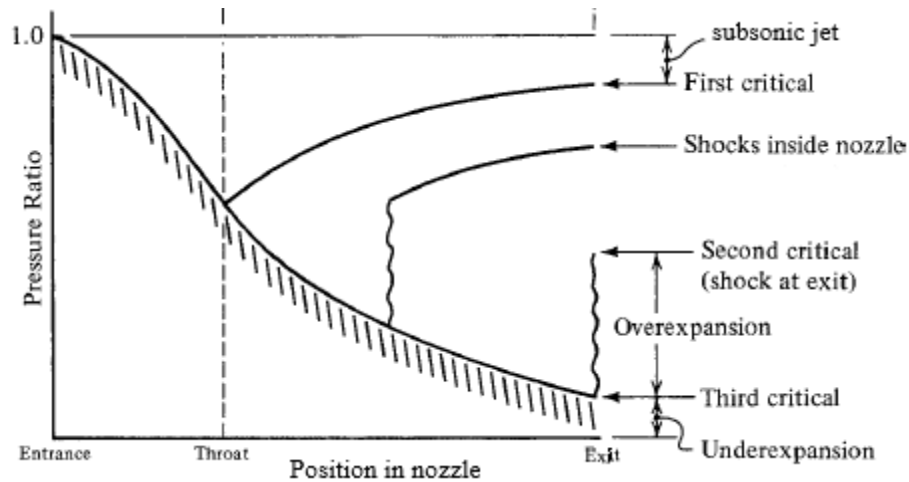


Figure 1.10: Evolution of pressure in the nozzle [14]

In both underexpansion and overexpansion cases there is a system of compression and expansion waves around the exiting jet, with consequent density discontinuities, which gradually achieves a match between the pressure in the jet and that of the surrounding. It is customary to describe the conditions for off-design supersonic discharge from the theoretical value, which is given as the *ratio of the design exit pressure to the ambient pressure*.

1.2.1.1 Adaptation

An ideal or adapted nozzle, i.e. the nozzle producing the maximum possible thrust, is a nozzle where the exit pressure is adapted to the ambient pressure ($p_e = p_a$). By definition an ideal nozzle expands the throat flow isentropically and produces a parallel uniform exit flow at a prescribed exit Mach or area ratio as shown in figure 1.6.a. and figure 1.11. This is called an ideal expanded flow or optimum expansion.

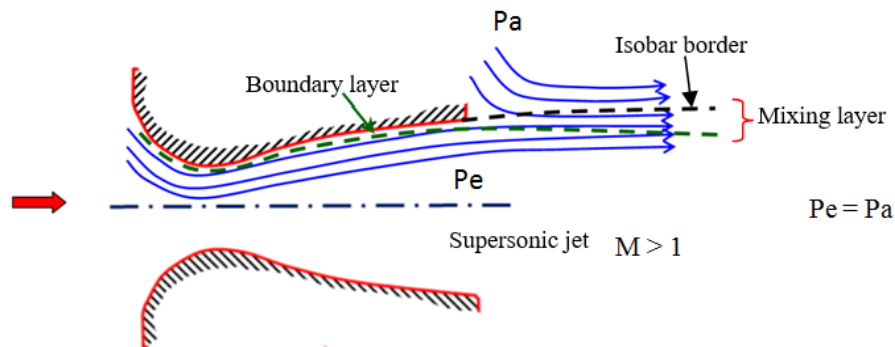


Figure 1.11: Ideal expanded flow [15]

However, most part of the operational time of a rocket engine, the supersonic discharge from the nozzle occurs under off-design conditions, where the nozzle exit pressure, p_e , differs from that of the atmosphere, p_a . Here both the overexpansion of the gas in the nozzle ($p_e < p_a$) and underexpansion ($p_e > p_a$) are possible.

1.2.1.2 Underexpansion

In the case of underexpansion, the flow leaving this nozzle has a pressure greater than the ambient pressure due to a small exit area and the flow is parallel to the axis. The expansion of the fluid is therefore incomplete within the nozzle and continues outside resulting in a system of expansion waves. Due to the high exit pressure, there is an enlargement of the supersonic jet and a divergence of the isobar border which separates the supersonic jet of the fluid from the outside environment.

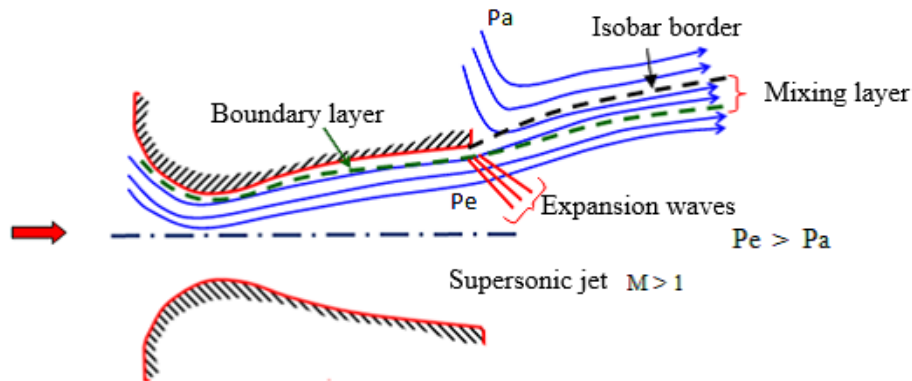


Figure 1.12: Underexpanded flow [15]

1.2.1.3 Overexpansion

For overexpanded flows, the ambient pressure is higher than the exit pressure. In this case there is need of a compression process at the exit in order for the flow to end up at the ambient pressure. However, a normal shock at the exit will produce too strong a compression. What is needed is a shock process that is weaker than a normal shock, and the oblique shock has been shown to be just this. Thus, at the exit an oblique shock emanates into the flowfield at an appropriate angle to achieve a match between the exit pressure and the ambient pressure, $p_e =$

p_a . Across the oblique shock, the flow is always deflected away from a normal to the shock front, and thus the flow is no longer parallel to the centerline.

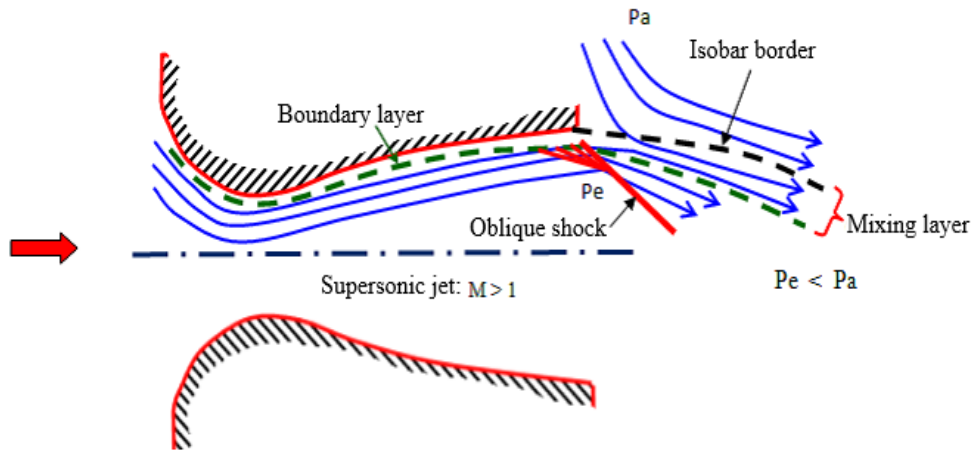


Figure 1.13: Overexpanded flow [15]

Both underexpansion and overexpansion cases are undesirable because the highest potential exhaust velocity is not achieved in underexpanded flow and, in an overexpanded flow, the second term in equation 1.1 is negative, thus decreasing the thrust. Under highly overexpanded conditions, there is a risk of flow separation in such nozzles. This is the case for example, when a rocket engine designed for altitude operation is tested at sea level. It also occurs during start transients, shut off transients, or engine throttling modes.

1.2.2 Flow separation in overexpanded nozzles

The physical problem encountered in nozzle flows is the result of boundary layer separation caused by an adverse pressure gradient which interacts with shocks and gives rise to complex phenomena. Under highly overexpanded conditions, when the nozzle theoretical wall exit pressure (the wall pressure obtained when the flow is ejected in to vacuum ambient conditions) goes down to approximately 80% to 40% of the ambient pressure, the boundary layer cannot sustain or negotiate the adverse pressure gradient imposed upon it by the inviscid outer flow, the flow then separates from the nozzle wall, causing a standing shock wave to form at the separation base. Thus, flow separation in any supersonic flow is a basic fluid-dynamics phenomenon that occurs at a certain nozzle pressure ratio (NPR) which is essentially as a result

CHAPTER I: Technological study and bibliographical analysis

of a process involving complex shock wave/boundary layer interaction (SWBLI) inside the nozzle.

It has been the subject of various experimental and numerical studies in the past. Today, with the renewed interest in supersonic flights and space vehicles, the subject has become increasingly important, especially for aerospace applications for rockets, missiles, supersonic aircraft, etc. The prime motive of which has been to improve nozzle performance under overexpanded flow conditions and to mitigate side-loads in nozzles during impulsive startup and shut down operation.

To understand the origin of the phenomenon, Figure 1.14 describes the process of flow separation by considering an incident supersonic flow. The Mach number M_i and the pressure p_i define the inviscid uniform flow. The skin friction coefficient (C_f), and the displacement thickness (δ) define the local characteristics of the boundary layer.

The adverse pressure gradient between the ambient and the wall pressure is necessarily transmitted in the upstream direction through the subsonic inner part of the attached boundary-layer. The effect of the adverse pressure is "felt" upstream at the incipient point I, which is the origin of the interaction. There is a subsequent deceleration of the fluid particles in the near-wall region and the boundary layer starts to thicken in the direction of the flow. This thickening of the boundary-layer subsonic channel resulting from a rise in pressure generates outgoing compression waves in the adjacent supersonic layer that rapidly coalesce to form a separation shock. The boundary-layer then separates at point S and the nozzle flow is directed towards the centerline by the shock while ambient air enters the separated region and flows towards the separation point until it is redirected into the shear layer and the recirculation region is developed in the vicinity of the wall.

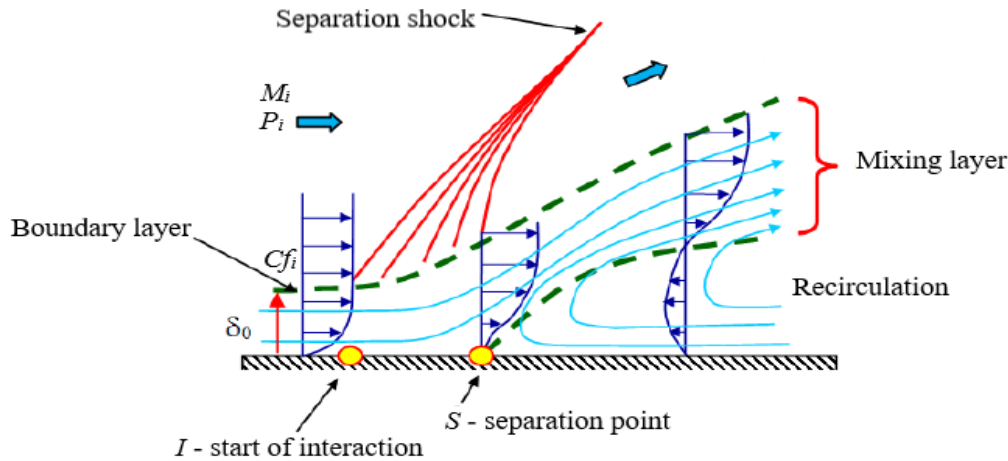


Figure 1.14: Shock induced boundary layer separation in an overexpanded nozzle, Délerly [16]

1.2.3 Structure of flow separation in overexpanded nozzles

In the 1940s, flow separation in rocket nozzles was for the first time investigated in detail [17]. It was understood that the boundary layer separated from the nozzle wall for wall pressures below a value of about one third of the ambient pressure and that the flow continued as a free stream. Today, this flow phenomenon is referred to as “Free Shock Separation”, FSS. During the development of the J-2S engine in the early 1970s [18], a second kind of flow separation was observed, where the separated flow reattached to the nozzle wall, thereby forming a closed recirculation bubble. The name “Restricted Shock Separation”, RSS, was chosen for this phenomenon, which was however only observed in sub-scale cold-gas tests and not completely understood. The existence of these two separation patterns have been corroborated by several experimental studies, performed on either subscale or full-scale optimized nozzles, and different numerical simulations in recent research.

1.2.3.1 Free Shock Separation (FSS)

In the free shock separation, the overexpanded nozzle flow fully separates from the wall at a certain ratio of wall to ambient pressure and never reattaches but continues as a free stream.

From the distribution of the wall pressure, the flow can be divided into 3 domains. The first domain is where the flow remains attached to the wall. This is the domain before the first deviation of the wall pressure. The first deviation of the wall pressure from the vacuum profile

corresponds to the incipient separation pressure, p_i (Fig.1.15), which denotes the origin of the interaction. The second is called the interaction domain. Here the wall pressure quickly rises from p_i to a plateau pressure, p_p , which is in general slightly lower than the ambient pressure p_a . The boundary layer effectively separates from the nozzle wall at x_s shortly before reaching the plateau pressure, p_p . In the recirculation zone downstream of the separation point, the wall pressure increases slowly from p_p to p_e , (Fig.1.15). This gradual pressure rise is due to the inflow and upstream acceleration of gas from the ambience into the recirculation region.

To predict the axial separation location inside a nozzle, the ratio of separation to ambient pressure $\frac{p_i}{p_a}$ must first be known. Using the vacuum wall pressure profile in the nozzle, the separation location can then easily be determined.

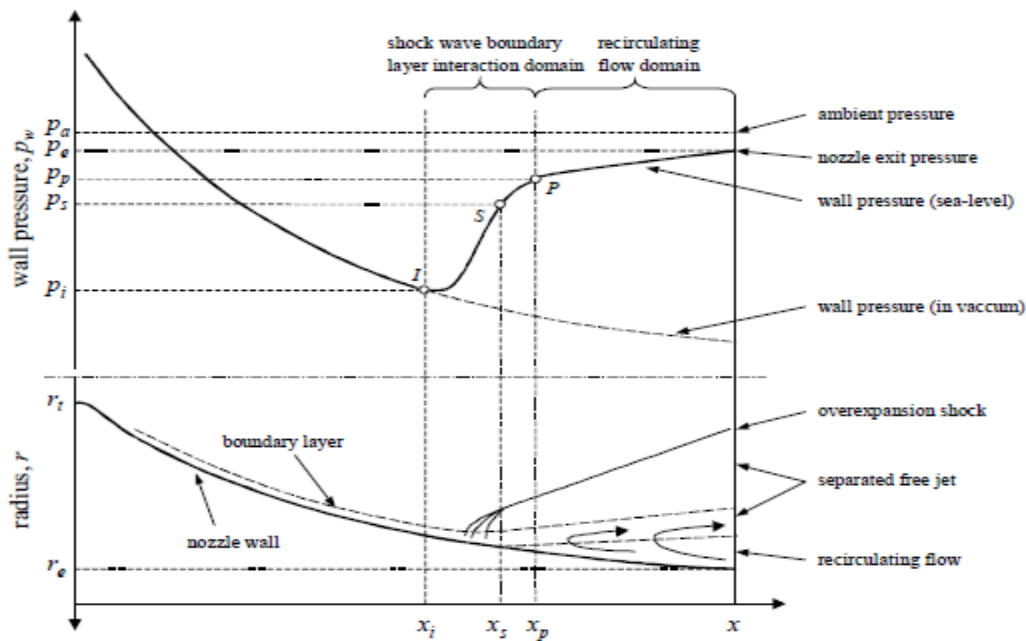


Figure 1.15: Phenomenological sketch of free shock separation (FSS) [19]

Figure 1.16 schematically shows the main features of a free shock separation. An oblique shock wave forms at the separation base creating a Mach reflection at the centerline forming the Mach disc, a shock wave normal to the incoming flow and a reflected shock called the "triple shock" where the oblique shock and the Mach disc meet. The triple shock extends into a supersonic

shear layer which envelopes the jet's core. The jet flow undergoes a series of expansion and compression waves until the jet becomes sub-sonic.

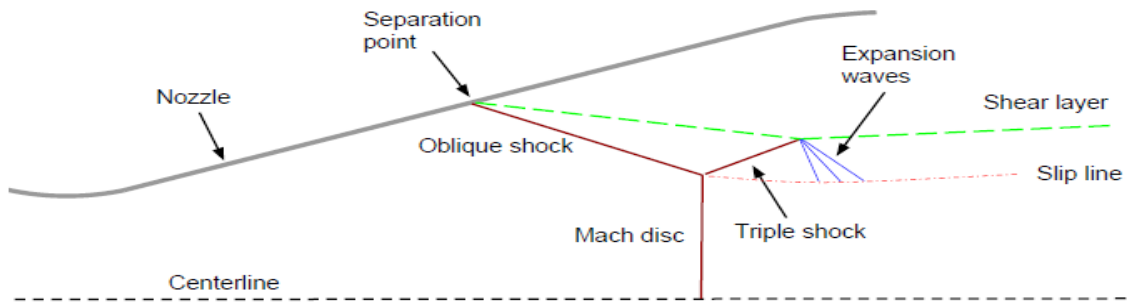


Figure 1.16: Shock pattern of supersonic flow with free shock separation inside an axisymmetric convergent-divergent nozzle [20]

1.2.3.2 Restricted Shock Separation (RSS)

In this flow regime, which only occurs at certain pressure ratios and in certain nozzles, the pressure downstream of the separation point shows an irregular behavior and partly reaches values above the ambient pressure. This is attributed to a reattachment of the separated flow to the nozzle wall, inducing a pattern of alternating shocks and expansion waves along the wall. Due to the short separated region, this flow regime is termed as restricted shock separation.

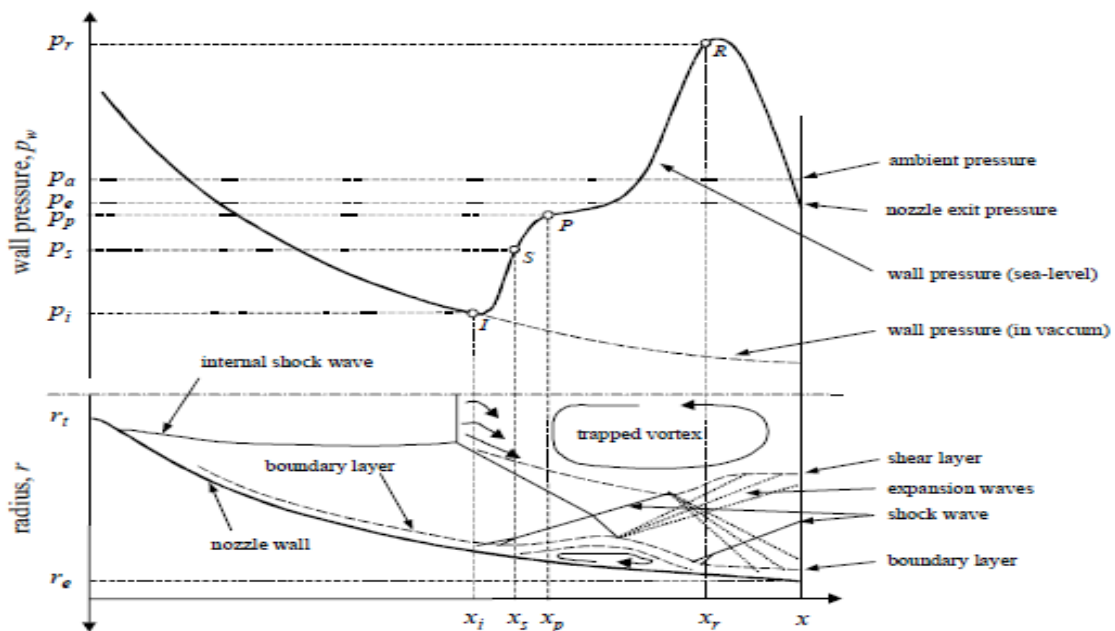


Figure 1.17: Phenomenological sketch of restricted shock separation (RSS) [19]

1.2.4 Separation criteria

In an attempt to understand and predict flow separation, a number of extended studies and experiments have been performed on overexpanded nozzles. Most of these studies are performed on conical and truncated ideal nozzles which only feature the free shock separation. The extended studies have resulted in a number of empirical and semi-empirical models to predict the separation point and the plateau pressure. These criteria present the rise in the plateau pressure p_p in function of the upstream conditions at the origin of the interaction ($M_i, p_i \dots$). In these criteria, the plateau pressure is assumed to be equivalent to the ambient pressure.

Some of the current separation point models for FSS are presented below.

1.2.4.1 Summerfield criterion

This is the most classical and simple criteria for FSS which is purely derived from nozzle testing with a pressure p_c/p_a between 15 and 20. It is based on extensive studies on the separation phenomenon in conical nozzles in the late 1940's.

$$p_i/p_p = 0.4 \quad (1.5)$$

1.2.4.2 Zukoski empirical criterion

Zukoski described the pressure ratio, p_i/p_p at the simple form,

$$\frac{p_i}{p_p} = \frac{2}{2 + M_i} \quad (1.6)$$

The criterion shows good agreement with performed experiments. But it has a drawback that all experiments were performed with air, and thus does not include the dependency of specific heats γ .

Another correlation that issued from the experiments carried out by Zukoski concerns the pressure at the separation point p_s .

$$\frac{p_s}{p_c} = \left(1 + 0.73 \frac{M_i}{2}\right) \quad (1.7)$$

1.2.4.3 Schmucker empirical criterion

Schmucker recommended an empirical criterion from the experimental data from the tests performed on liquid rocket propellant engines. The recommended correlation by Schmucker is;

$$\frac{p_i}{p_p} = (1.88M_i - 1)^{-0.64} \quad (1.8)$$

1.2.4.4 Schilling criterion

Based on experiments with conical and truncated ideal nozzles, Schilling derived in 1962 a simple expression accounting for the increase of separation pressure ratio $\frac{p_i}{p_p}$ with increasing Mach number,

$$\frac{p_i}{p_p} = k_1 \left(\frac{p_c}{p_p}\right)^{k_2} \quad (1.9)$$

with $k_1 = 0.582$ and $k_2 = -0.195$ for contoured nozzles, and $k_1 = 0.541$, and $k_2 = -0.136$ for conical nozzles.

1.2.4.5 Kalt and Bendall criterion

In 1965, based on Schilling's expression Kalt and Badal chose $k_1 = 2/3$ and $k_2 = -0.2$ for a better agreement with their experimental results.

1.3 Test campaigns on nozzle flow

In Europe, interest for nozzle flow behavior and performance optimization is still high. The European industrial partners Snecma and Volvo Aero together with the research institutions DLR, ONERA, LEA Poitiers and somewhat later also ESTEC focused their research efforts in the European Flow Separation Control Device (FSCD) group, which is organized by Centre National d'Etudes Spatiales CNES, focusing mainly on technological challenges of thrust

CHAPTER I: Technological study and bibliographical analysis

chambers [19,21]. An important part of the work consists in cold sub-scale tests, which are performed at four different test facilities at FOI (Sweden) [22], LEA Poitiers (France) [23], DLR Lampoldshausen (Germany) [24,25] and ONERA Meudon (France) [26, 27]. These cold gas tests allow investigations of critical nozzle flow phenomena in a relatively inexpensive and more versatile way than hot gas firing tests. A large amount of transducers and measurement techniques can also be used. Within the FSCD group, several attempts have been undertaken to improve the accuracy of separation prediction as well as the control of flow separation and side-loads in rocket nozzles with different contour designs.

Activities on nozzle flow with respect to flow separation and side-loads were initiated after high side-loads had been observed in a Vulcain engine. Since then, a series of test campaigns have been performed on either subscale or full-scale optimized nozzles. Sub-scale tests in a truncated ideal nozzle were carried out at LEA Poitiers, including dynamic wall pressure measurements [28]. At ONERA, a planar nozzle flow was investigated, where either a symmetrical or unsymmetrical shock could form [29]. In addition, a series of extensive experimental campaigns [30-35] have been conducted in order to characterize the influence of film cooling on flow separation phenomena. Wind tunnel tests with a sub-scaled Vulcain nozzle performed by Volvo Aero [36] showed the occurrence of RSS over a wide range of pressure ratios. It could be shown that huge side-loads were induced when the flow changed from FSS to RSS and vice versa [36]. By analyzing different nozzle design methods, DRL [37-44] carried out a cold flow test series to study the boundary layer separation and the related flow field in nozzles. DLR [38] showed that a weak shock exists inside thrust-optimized nozzles where re-attached flows are well-known for, originating from the beginning of the divergent nozzle section. This internal shock causes a plume pattern very different from the expected Mach disk and was called “cap shock pattern”. At low pressure ratios with flow separation, the cap shock pattern can cause the separated flow to reattach to the wall and thus cause RSS, even in full-scale engines as the Vulcain and the SSME [38]. Experiments [37, 39] also showed that even in TIC nozzles significantly high-amplitude side-loads may occur in particular at low pressure regimes, confirming earlier findings [38] of symmetrical/unsymmetrical boundary-layer separations and subsequent side-loads generation in conical nozzles. Stark and Wagner [39, 41] summarized recent findings achieved on TIC nozzles, with emphasis on the separation criteria and understanding of side-loads generation in

CHAPTER I: Technological study and bibliographical analysis

which a simple criterion was presented which is valid for turbulent nozzle flows and, therefore, suitable for technical application to rocket engines.

Outside Europe, USA [45] and Japan [46] have also carried out extensive experimental evaluations of flow separation in side-loads characteristics on different high-area-ratio rocket engines.

The figures 1.18-19 show the different shock patterns in the plume of overexpanded rocket nozzles that have been observed.



Figure 1.18: Cap shock pattern (left) and Mach disk (right) in the plume of the Vulcain engine [4]

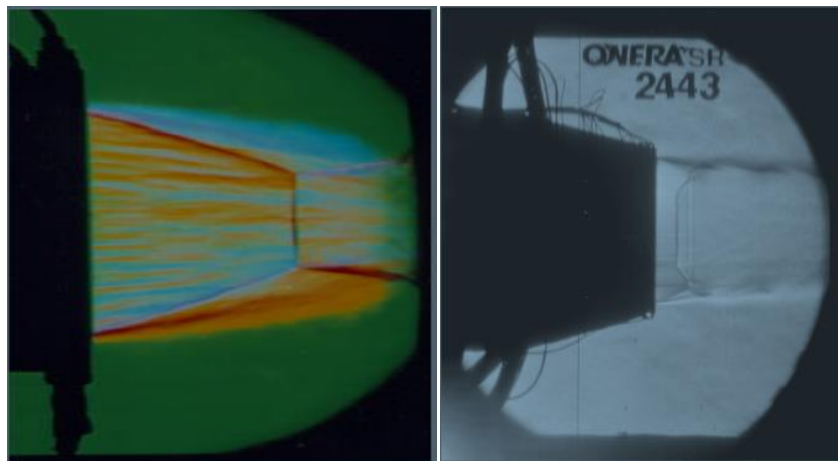


Figure 1.19: Exhaust plume patterns for nozzles, a) truncated ideal nozzle, with Mach disk, P6 TIC DLR [1], c) TOP ONERA [19]

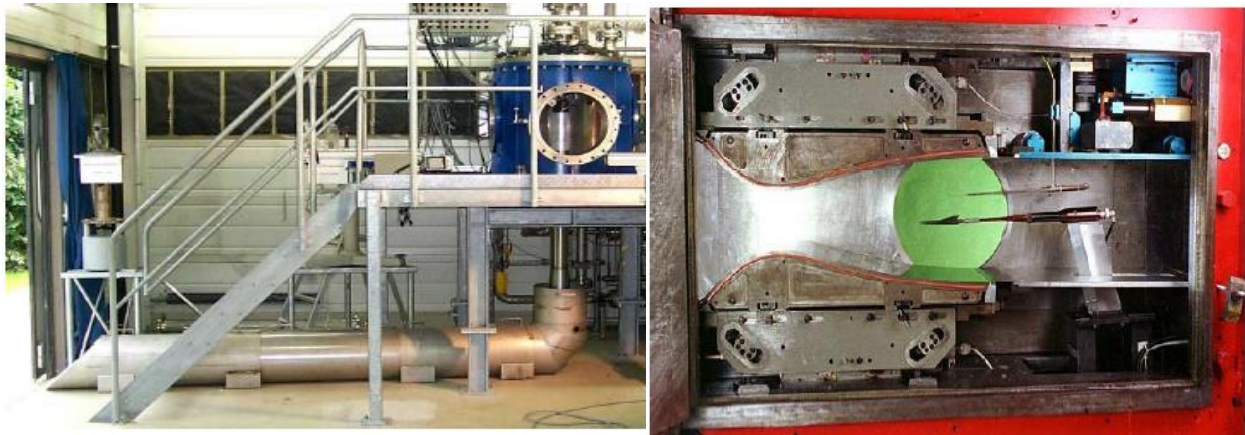


Figure 1.20: a) Cold gas subscale test facility P6.2 and b) ONERA R2Ch blowdown wind tunnel

1.4 Numerical investigations on nozzle flow

To corroborate experimental findings, extensive numerical studies as well as analytical considerations are being used to understand the physical phenomena connected to flow separation and side-loads in rocket nozzles.

From a numerical point of view, it is worth noticing that the modelling challenge is to predict the boundary layer in nozzles at a very high-Reynolds number to adequately simulate the interaction of shock-waves with large and small scale turbulence and associated phenomena.

Stark and Wagner [41] performed a series of CFD tests on a truncated ideal nozzle using the Tau code, developed by DLR to corroborate the tests conducted in cold flow test position P6.2, where they found that the shape of the Mach disk and the reflected shock are well resolved by the computations. Both in the experiments and in the computations the Mach disk is bended downstream. Bowed Mach disks at moderate NPRs could also be found in computations from Nasuti and al. [47] and Pilinski [48]. P. Reijasse, [49] carried out experimental and numerical investigations on the Cap-Shock structure in overexpanded thrust-optimized nozzles following the test campaign characterizing flow separation in overexpanded subscale nozzles performed in the R2Ch blowdown wind tunnel of the ONERA Chalais-Meudon center. In his calculations using Nasca research code, the outstanding results was the recirculating bubble seen on the nozzle centerline of the Mach disc which confirmed other computational and experimental

CHAPTER I: Technological study and bibliographical analysis

results performed in Europe [50-53]. In addition, P. Reijasse and Boccaletto [54] undertook steady and unsteady RANS computations to investigate the influence of the film cooling onto the shock in the subscale over-expanded nozzle. The objective was to conclude on the ability of this computation to re-build the features on the nozzle flow behavior during the transient of the wall film injection. In their findings, steady and unsteady computations can re-build the experimental features and have clearly revealed a dynamic phenomenon of the separation shock foot region during the rapid film injection. Many other steady computations of film cooling influence on the nozzle flow separation have been conducted by ONERA teams [50, 55, 56]. Stark and Hagemann [1] presented CFD simulations using the data from DLR's cold flow test facility P6.2 with the objective to compute the flow inside a strongly over-expanded truncated ideal contour nozzle with respect to the prediction of location and shape of the flow separation, the oblique shock and the Mach disc by using different turbulence models. The evaluation showed that up-to-date CFD simulations (at least for cold flow nozzles) tend to under-predict the separation location. A small advantage arose for $k\omega$ and Spalart-Allmaras turbulence models and they seem to be a better approach to calculate nozzle flows.

Many modelling efforts [57] have been carried out in the European FSCD frame to progress forward in the field of numerical simulations and modelling capabilities. Most of the numerically observed behaviors are consistent with experimental data, though accurate separation locations are still questionable and limited to the capabilities of state of the art turbulent models.

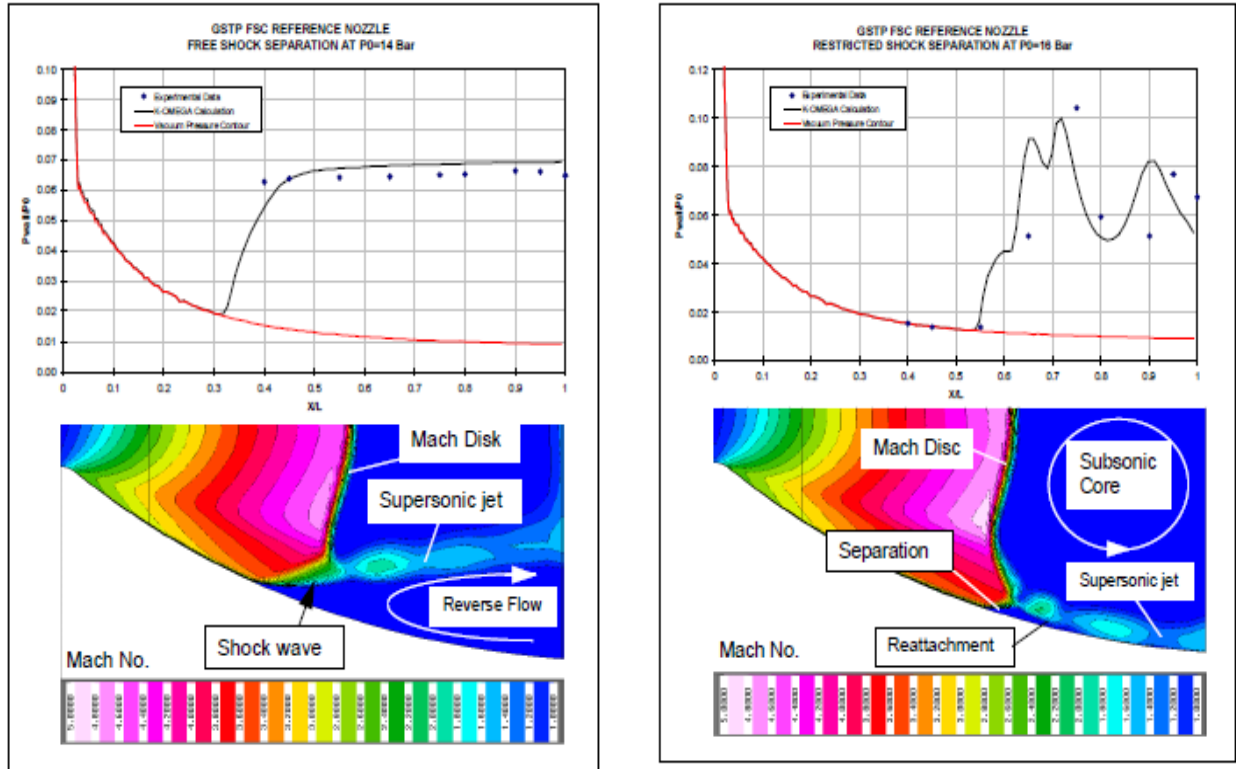


Figure 1.21: CFD calculated Mach number distribution in Volvo S1 nozzle [4]

1.5 Regenerative cooling on overexpanded nozzles

The primary objective of cooling is to prevent chambers and nozzle walls from failing, a condition where they no longer withstand the imposed loads or stresses. With rising heat rates, most wall materials ultimately fail and eventually melt. Cooling must therefore be implemented to reduce wall temperatures to acceptable levels.

Regenerative cooling is done with cooling jackets or a special cooling passage built around the thrust chamber where one liquid propellant (usually the fuel) circulates through to absorb the heat transfer from the hot reaction gases to the thrust chamber walls before it is fed to the injector. This cooling technique is used primarily in bipropellant chambers of medium to large thrust capacity. It has been very effective in applications with high chamber pressures and high heat transfer rates. Moreover, as some of the heat is transferred to the fuel there is slight increase in specific impulse of such engine owing to regain of certain amount of energy, which would be otherwise lost as heat to the walls. Due to its similarity to steam regenerators, the method is called regenerative cooling.

CHAPTER I: Technological study and bibliographical analysis

Jackets can consist of separate inner and outer walls (Fig.1.23) or of an assembly of contoured, adjacent tubes (Fig.1.22). Internal cooling passages, cooling jackets, or cooling coils permit the circulation of the coolant. These tubes are usually bent to the chamber and nozzle contours; they are formed hydraulically to give a variable cross section to permit the same number of tubes at the throat and exit diameters. The inner wall usually made of copper confines the gases, and the spaces between the walls serve as the coolant passage.

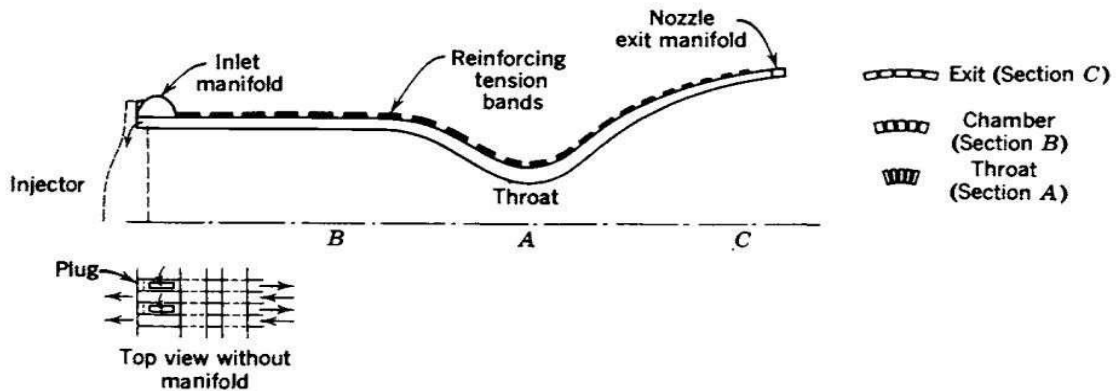


Figure 1.22: Cross-sections view of tubes [3]

Coolant enters through the inlet manifold i.e. fuel inlet into every other tube and proceeds axially to the nozzle exit manifold, where it then enters the alternate tubes and returns axially to go directly to the injector as shown in the figure below (Fig.1.23) .

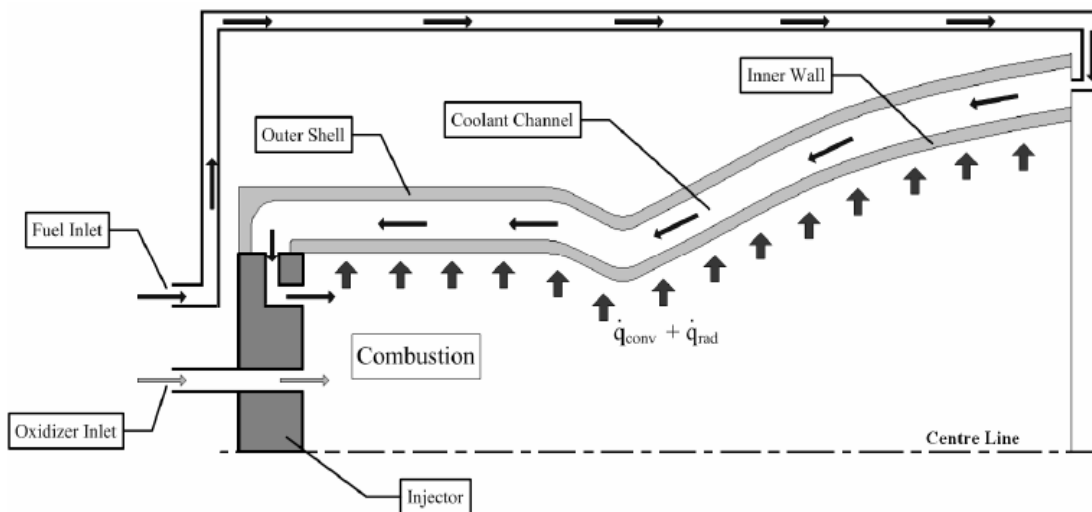


Figure 1.23: Cross-sectional view of a thrust chamber with regenerative cooling

CHAPTER I: Technological study and bibliographical analysis

The nozzle throat region usually has the highest heat flux and is therefore the most difficult to cool. For this reason the cooling passage is often designed so that the coolant velocity is highest at the critical regions by restricting the coolant passage cross-section (Fig.1.22). In some cases to increase the cooling efficiency, coolant can enter the coolant passages either from the nozzle exit and throat (Fig.1.24-a) or directly from the throat (Fig.1.24-b). This type of regenerative cooling is called dual regenerative cooling.

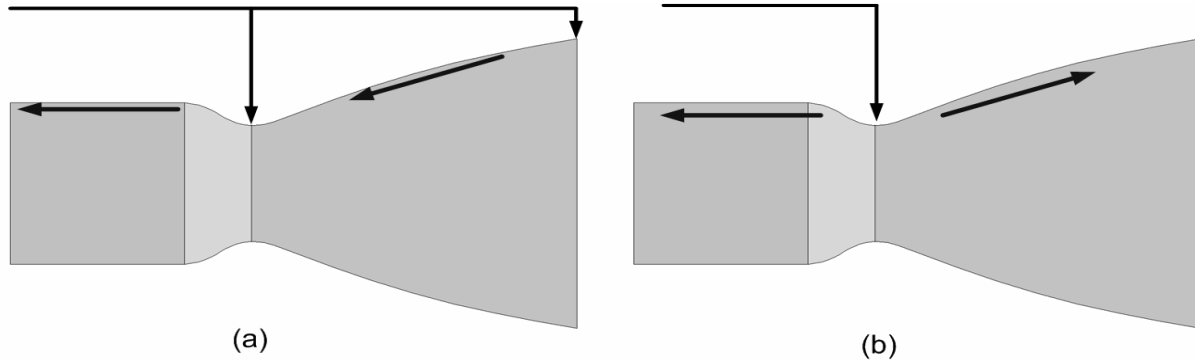


Figure 1.24: Schematic views for dual regenerative cooling

The heat transfer between the combusted gases and thrust chamber wall is by convection and radiation (Fig.1.23) while heat transfer between the coolant and thrust chamber wall is by forced convection. This heat transfer in a regeneratively cooled thrust chamber can be described as the heat flow between two moving fluids, through a multilayer partition as given in figure 1.25 and the total heat flux can be given as:

$$\dot{q}_{tot} = \dot{q}_g = \dot{q}_s = \dot{q}_c \quad (1.10)$$

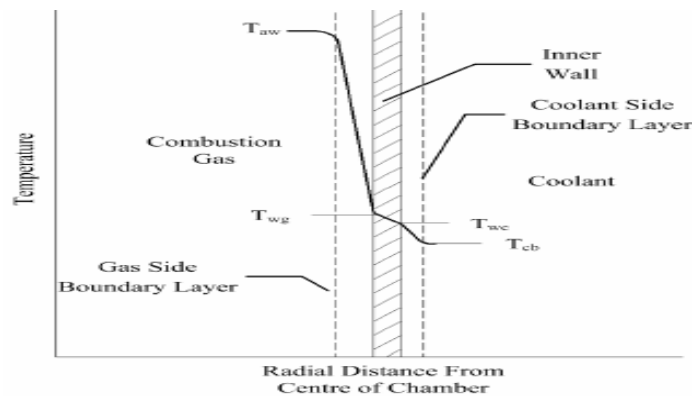


Figure 1.25: Heat transfer schematic for regenerative cooling

CHAPTER I: Technological study and bibliographical analysis

In order to provide sufficient cooling temperature of interior side of chamber wall, T_{wg} , which is directly exposed to hot combustion gases, (T_{aw}) must be lowered to some acceptable level. This is usually temperature at which material of chamber still has enough strength to withstand all accompanying stresses. Limitations of regenerative cooling encompass maximum allowable coolant temperature (called critical temperature), chamber wall thickness or fuel pressure drop in cooling channels.

Regenerative cooling is in most cases considered as a steady-state process, in which an acceptable temperature distribution occurs in the combustion chamber and nozzle wall. Given that condition holds up, regenerative cooling can work virtually for the infinite time and is only limited by available amount of propellants.

1.6 Performance losses due to shocks, separation and cooling

Because of the tremendous energy flow in rocket engines, these engines are characterized by small performance losses due to heat loss, friction, vaporization and mixing inefficiencies, etc. Other losses include losses due to shocks and separation. However, even small losses have a large impact on delivered payload or range of the system and are therefore important.

The consequences of shock wave/boundary layer interaction (SWBLI) are multiple and often critical for the vehicle performance. The shock submits the boundary layer to an adverse pressure gradient which may strongly distort its velocity profile thereby leading to non-uniformity of the flow. At the same time, in turbulent flows, turbulence production is enhanced which amplifies the viscous dissipation leading to aggravated performance losses.

Unstable separation is associated with high total pressure losses resulted from the occurrence of lambda shock and aftershocks, which results in loss of thrust performance. In addition, shock-induced separation most often results in high levels of unsteady lateral forces so-called side-loads which can damage the vehicle structure or, at least, severely limit its performance.

Cooling of thrust chamber walls is important, however there are some propulsion performance penalties that may accompany it. In regeneratively cooled liquid propellant rocket engines, the coolant pressure drop must be properly regulated because a higher pressure drop allows a higher coolant velocity in the cooling channel (and thus a better cooling), however, the pumping energy

CHAPTER I: Technological study and bibliographical analysis

required to overcome pressure losses in propellant and coolant liner result in a loss in impulse efficiency and requires a heavier feed system that increases the engine mass and thus also the total inert vehicle mass.

Conclusion

Flow separation is a natural phenomenon as well as an engineering problem of fundamental importance in numerous industrial applications. In most cases it is an undesirable phenomenon. The encounter of a shock wave with a boundary layer results in complex phenomena because of the rapid retardation of the boundary layer flow and the propagation of the shock in a multilayered structure. These interactions are responsible for acoustic, vibrate-acoustic, thermal, and mechanical-induced loads that act on the structure.

Since over-expanded flow results in total pressure losses, it is important to predict the thrust loss and thrust performance of the nozzle. Thrust performance could be improved by encouraging stable separation and controlling the location and extent of that separation. These objectives may be achieved by predicting the main state variables, while solving the governing equations of such flows. A task that is to be highlighted in the following chapter.

CHAPTER II: Modelling and governing equations

Introduction

Computational fluid dynamics or CFD is the analysis of systems involving fluid flow, heat transfer and associated phenomena such as chemical reactions by means of computer-based simulation. This branch of fluid mechanics uses numerical analysis and data structures to solve equations of flow (in a unique form) over a control volume.

Computational fluid dynamics constitutes a new “third approach” in the philosophical study and development of the whole discipline of fluid dynamics. The two other approaches are pure experiment and theory. It complements experimental and theoretical fluid dynamics by providing a cost-effective means of simulating real flows. The governing equations of computational fluid dynamics are based on the conservation law of physical properties i.e. mass, energy, and momentum

2.1 Governing equations of fluid flow

To understand the physics of the fluid in motion related to any engineering problem, it is important to develop an accurate relationship among the variations of the fluid flow properties such pressure, temperature, velocity, density etc. at discrete points in space and time. The fluid governing equations proves a theoretical solution to how these flow properties are related to each other by either integral, differential or algebraic equations.

A simplification and idealization of the full two or three-dimensional equations of real flow behaviors is done by assuming the flow to be one-dimensional.

The following three fundamental laws known as the conservation laws are used to establish the governing equations of the fluid flow.

2.1.1 Conservation of mass

By definition the mass of a closed system remains constant over time, as the system’s mass cannot change, so the quantity can neither be added nor be removed.

$$\frac{d(\text{mass})}{dt} = 0 \tag{2.1}$$

CHAPTER II: Modelling and governing equations

The integral form of the momentum equation [13]

$$\left(\frac{dm}{dt}\right)_{sys} = \frac{\partial}{\partial t} \left(\iiint \rho d\tilde{V} \right) + \iint \rho(V \cdot \tilde{n}) dA \quad (2.2)$$

where ρ is the fluid density and \tilde{V} the control volume and A the area. The fluid velocity is $V = ui + vj + wk$ where u , v , and w are the velocity components in i , j and k directions.

It is known by equation (2.1) that this must be zero; thus the transformed equation

$$\frac{\partial}{\partial t} \left(\iiint \rho d\tilde{V} \right) + \iint \rho(V \cdot \tilde{n}) dA = 0 \quad (2.2)$$

This equation is called the *continuity equation*; it is an integral formulation of the conservation of mass principle as applied to a fluid flow. Equation (2.2) is quite general, it applies to all flows, compressible, incompressible, viscous or inviscid.

For steady flow, any partial derivative with respect to time is zero and the equation becomes

$$\iint \rho(V \cdot \tilde{n}) dA = 0 \quad (2.3)$$

For a steady, one-dimensional flow, the continuity equation for a control volume is:

$$\sum \rho u A = 0 \quad (2.4)$$

If there is only one section where fluid enters and one section where fluid leaves the control volume, this becomes

$$(\rho u A)_{out} - (\rho u A)_{in} = 0, \text{ or } (\rho u A)_{out} = (\rho u A)_{in} \quad (2.5)$$

This is usually written as

$$\dot{m} = \rho u A = \text{constant} \quad (2.6)$$

2.1.2 Conservation of momentum (Newton's second law)

The time rate of change of momentum of a body equals the net force exerted on it.

CHAPTER II: Modelling and governing equations

Newton's second law tells us that its linear momentum will be changed in direct proportion to the applied forces. This is expressed by the following equation[14]:

$$\sum F = \frac{d(mV)}{dt} \quad (2.7)$$

Based on the Newton's second law the following equation is given in integral form for momentum [13]:

$$\frac{d(mV)}{dt} = \iiint \frac{\partial(\rho V)}{\partial t} d\tilde{v} + \iint \rho V(V \cdot \hat{n}) dA \quad (2.8. a)$$

From equation (2.7), the integral form becomes

$$\sum F = \iiint \frac{\partial(\rho V)}{\partial t} d\tilde{v} + \iint \rho V(V \cdot \hat{n}) dA \quad (2.8. b)$$

$$\iiint \frac{\partial(\rho V)}{\partial t} d\tilde{v} + \iint \rho V(V \cdot \hat{n}) dA = \iiint \rho f d\tilde{v} - \iint p dA \quad (2.9)$$

f represents the body force per unit mass of the fluid.

The equation (2.9) is called the momentum equation. It is a general formulation Newton's second law applied on inviscid fluid flows. The equation above (2.9) does not include the effects of friction. If friction were to be included, it would appear as additional surface forces, which are the shear and normal viscous stresses integrated over the control volumes.

$$\iiint \frac{\partial(\rho V)}{\partial t} d\tilde{v} + \iint \rho V(V \cdot \hat{n}) dA = \iiint \rho f d\tilde{v} - \iint p dA + F_{viscous} \quad (2.10)$$

Assuming one-dimensional steady flow and absence of body force, the first and third term in equation 2.9 become zero. The equation becomes

$$\iint (\rho V \cdot dA) u = - \iint p dA \quad (2.11)$$

If there is only one section where fluid enters and one section where fluid leaves the control volume, we know (from continuity) that

$$\rho_1(-u_1 A) + \rho_2(u_2 A) = -(p_1 A + p_2 A) \quad (2.12. a)$$

CHAPTER II: Modelling and governing equations

or

$$p_1 + \rho_1 u_1 = p_2 + \rho_2 u_2 \quad (2.12. b)$$

Equation 2.12 is the momentum equation for a steady one dimensional flow.

2.1.3 Conservation of energy (First law of thermodynamics)

The first law of thermodynamics is a statement of conservation of energy. For a system composed of a given quantity of mass that undergoes a thermodynamic process without transfer of matter, the first law is often formulated as

$$Q + W = \Delta E \quad (2.13)$$

where,

Q = the net heat transferred into the system

W = the net work done by the system

ΔE = the change in total energy of the system

This can also be written on a rate basis to yield an expression that is valid at any instant of time:

$$\frac{dQ}{dt} = \frac{dW}{dt} + \frac{dE}{dt} \quad (2.14)$$

Based on the above law the following equation is given in integral form [13]

$$\iiint \rho \dot{q} d\tilde{V} - \iint p V dA + \iiint \rho f d\tilde{V} = \iiint \frac{\partial}{\partial t} \left[\rho \left(e + \frac{v^2}{2} \right) \right] d\tilde{V} + \iint \rho \left(e + \frac{v^2}{2} \right) V \cdot dA \quad (2.15)$$

where e is internal energy (per unit mass), and \dot{q} is the rate of heat added. The term is $\left(e + \frac{v^2}{2} \right)$ the sum of internal and kinetic energies per unit mass.

The equation (2.15) is called the energy equation. It is the integral formulation of the first law of thermodynamics applied on inviscid fluid flows. In this equation there is no thermal conduction or diffusion, no shaft work and there is no work done by viscous stresses.

CHAPTER II: Modelling and governing equations

The first term (2.15) on the left physically represents the total rate of heat added to the gas inside the control volume. For the sake of simplicity, this integral volume is noted \dot{Q} . The third and fourth term are zero because of zero body force and steady flow respectively. Hence equation (2.15) becomes

$$\dot{Q} - \oint pV \, dA = \oint \rho \left(e + \frac{V^2}{2} \right) V \cdot dA \quad (2.16)$$

Evaluating integrals on the surface of the control volume, the following equation is obtained [13]

$$\dot{Q} - (-p_1 u_1 A + p_2 u_2 A) = -\rho_1 \left(e + \frac{u_1^2}{2} \right) u_1 A + -\rho_2 \left(e + \frac{u_2^2}{2} \right) u_2 A \quad (2.17)$$

Simplifying equation (2.17) and such that $h = e + pv$

$$h_1 + \frac{u_1^2}{2} + q = h_2 + \frac{u_2^2}{2} \quad (2.18)$$

Equation (2.18) is the energy equation for a steady one dimensional flow.

2.2 Equations of conservation in compressible flows

The equations for a one-dimensional flow in a nozzle can be solved by carrying out calculations by section .i.e. the gas velocity, pressure, temperature, and density (v,p,T, ρ) are all uniform across any section normal to the nozzle axis, and are thus only a function of the section position.

2.2.1 Speed of sound

The so-called speed of sound is the rate of propagation of a pressure pulse of infinitesimal strength through a still fluid.

The differential form of the continuity equation and the equation of momentum in a steady one-dimensional flow can be written as;

$$\frac{d\rho}{\rho} + \frac{dV}{V} + \frac{dA}{A} = 0 \quad (2.19)$$

and

$$dp + \rho V dV = 0 \quad (2.20)$$

CHAPTER II: Modelling and governing equations

Analyzing a pulse of finite strength and applying equations (2.19 and 2.20) across a sound wave, the sonic velocity is given by the following expression [58]:

$$a^2 = \left(\frac{\partial p}{\partial \rho} \right)_s \quad (2.21)$$

we have,

$$\frac{p}{\rho^\gamma} = \text{constant} \quad (2.22)$$

Thus,
$$a^2 = \left(\frac{\partial p}{\partial \rho} \right)_s = \gamma \rho^{\gamma-1} \frac{p}{\rho^\gamma} = \gamma \frac{p}{\rho} \quad (2.23)$$

And the perfect gas equation of state gives,

$$p = \rho r T \quad (2.24)$$

Therefore, equation (2.23) becomes,

$$a = \sqrt{\gamma r T} \quad (2.25)$$

Equation (2.25) is called the sonic velocity relation

2.2.2 Mach number

The *Mach number* is defined as

$$M = \frac{u}{a} \quad (2.26)$$

where,

$u \equiv$ the velocity of the medium

$a \equiv$ sonic velocity through the medium

2.2.3 Stagnation expressions

CHAPTER II: Modelling and governing equations

These expressions are derived from the conservation of energy.

The differential form of the energy equation (2.16) is,

$$dh + VdV = 0 \Rightarrow c_p dT + VdV = 0 \quad (2.27)$$

Without heat addition, the energy equation (2.18) becomes

$$h_1 + \frac{u_1^2}{2} = h_2 + \frac{u_2^2}{2} = \text{constant} \quad (2.28)$$

The constant in Eq. (2.28) is equal to the maximum enthalpy that the fluid would achieve if brought to rest adiabatically. We call this value h_o , the *stagnation enthalpy* of the flow. Thus we rewrite Eq. (2.28) in the form

$$h + \frac{u^2}{2} = h_o = \text{constant} \quad (2.29)$$

Knowing from equation (2.26) that

$$u^2 = M^2 \times a^2$$

and [from equation (2.25)]

$$a^2 = \gamma r T$$

we have

$$h_o = h + \frac{M^2 \times \gamma r T}{2} \quad (2.30)$$

Using the Meyer relation and the isentropic ratio of specific heats equations, the specific heat at constant pressure can be written in terms of γ and r .

Meyer's relation

$$r = c_p - c_v \quad (2.31)$$

Ratio of specific heats

CHAPTER II: Modelling and governing equations

$$\gamma = \frac{c_p}{c_v} \quad (2.32)$$

The specific heat at constant pressure

$$c_p [\text{J}/(\text{kg} \cdot \text{K})] = \frac{\gamma r}{\gamma - 1} \quad (2.33)$$

Combining (2.33) and (2.30) gives

$$h_o = h + M^2 \frac{\gamma - 1}{2} c_p T \quad (2.34)$$

But for a perfect gas

$$h = c_p T \quad (2.35)$$

Thus

$$h_o = h \left(1 + \frac{\gamma - 1}{2} M^2 \right) \quad (2.36)$$

Using $h = c_p T$ and $h_o = c_p T_o$, this can be written as

$$T_o = T \left(1 + \frac{\gamma - 1}{2} M^2 \right) \quad (2.37)$$

Now, the stagnation process is isentropic. Using equation (2.24) and (2.22) between point 1 and 2 yields,

$$\frac{p_2}{p_1} = \left(\frac{T_2}{T_1} \right)^{\frac{\gamma}{\gamma - 1}} \quad (2.38)$$

Let point 1 refer to the static conditions, and point 2, the stagnation conditions. Then, combining (2.38) and (2.37) produces

$$\frac{p_o}{p} = \left(\frac{T_o}{T} \right)^{\frac{\gamma}{\gamma - 1}} = \left(1 + \frac{\gamma - 1}{2} M^2 \right)^{\frac{\gamma}{\gamma - 1}} \quad (2.39)$$

or

CHAPTER II: Modelling and governing equations

$$p_o = p \left(1 + \frac{\gamma - 1}{2} M^2\right)^{\frac{\gamma}{\gamma - 1}} \quad (2.40)$$

From equation (2.24) the total density becomes

$$\frac{\rho_o}{\rho} = \left(1 + \frac{\gamma - 1}{2} M^2\right)^{\frac{1}{\gamma - 1}} \quad (2.41)$$

2.2.4 Area ratio

The perfect-gas and isentropic flow relations can be used to convert the continuity relation (2.6) into an algebraic expression involving only area and Mach number, as follows. Equate the mass flow at any section to the mass flow under sonic conditions (*).

$$\rho^* u^* A^* = \rho u A \quad (2.6)$$

$$\frac{A}{A^*} = \frac{\rho_o u^*}{\rho u} = \frac{p_o T u^*}{p T_o u} \quad (2.42)$$

$$\frac{A}{A^*} = \frac{1}{M} \left[\frac{1 + \frac{\gamma - 1}{2} M^2}{\frac{\gamma + 1}{2}} \right]^{\frac{\gamma + 1}{2(\gamma - 1)}} \quad (2.43)$$

2.2.5 Velocity

The flow velocity can be determined using the energy equation (2.2)

$$u = \sqrt{2(h_o - h)} \quad (2.44)$$

For a perfect gas,

$$u = \sqrt{2C_p(T_o - T)} \quad (2.45. a)$$

or

$$u = \sqrt{2c_p T_o \left(1 - \frac{T}{T_o}\right)} \quad (2.45. b)$$

CHAPTER II: Modelling and governing equations

Using equations (2.38) and (2.33), the expression for the velocity becomes,

$$u = \sqrt{\frac{2\gamma}{\gamma-1} rT_0 \left[1 - \left(\frac{p}{p_0} \right)^{\frac{\gamma-1}{\gamma}} \right]} \quad (2.46)$$

2.2.6 Sonic conditions

At the sonic condition (*) a unique gas pressure ratio exists, which is only a function of the ratio of specific heats γ . This pressure ratio is found by setting $M = 1$.

Therefore equation 2.40 becomes

$$\frac{p_0}{p^*} = \left(\frac{\gamma+1}{2} \right)^{\frac{\gamma}{\gamma-1}} \quad (2.47)$$

and

$$\frac{T_0}{T^*} = \frac{\gamma+1}{2} \quad (2.48)$$

The mass flow rate per unit area is

$$\rho^* u^* A^* \quad (2.49)$$

knowing $u^* = a = \sqrt{\gamma r T^*}$; $\rho^* = \frac{p^*}{r T^*}$

equation 2.49 becomes

$$\dot{m} = \frac{p^*}{r T^*} T^* \sqrt{\gamma r T^*} \quad (2.50)$$

Introducing the stagnation values using equations (2.48) and (2.47) into equation (2.50) yields,

$$\dot{m} = \left(\frac{2}{\gamma+1} \right)^{\frac{\gamma+1}{2(\gamma-1)}} \sqrt{\frac{\gamma}{r T_0} A^* p_0} \quad (2.51)$$

2.2.7 Mach number and area ratio in function of pressure ratio

CHAPTER II: Modelling and governing equations

The Mach number in function of the pressure ratio is:

$$M = \sqrt{\frac{2}{\gamma - 1} \left[\left(\frac{p_0}{p} \right)^{\frac{\gamma-1}{\gamma}} - 1 \right]} \quad (2.52)$$

The expression of the area ratio can also be expressed in terms of the pressure ratio as follows;

$$\frac{A}{A^*} = \sqrt{\left(\frac{\gamma - 1}{2} \right)} \times \left(\frac{2}{\gamma + 1} \right)^{\frac{\gamma+1}{2(\gamma-1)}} \times \frac{1}{\left(\frac{p}{p_0} \right)^{1/\gamma} \sqrt{1 - \left(\frac{p}{p_0} \right)^{\frac{\gamma-1}{\gamma}}}} \quad (2.53)$$

2.3 Thrust coefficient

Principles from gas dynamics and thermodynamics describe processes inside a rocket nozzle and its chamber. These mathematical relations obtained from these principles can be used for evaluating and comparing the performance between different rocket systems since with them one can predict operating parameters for any system that uses the thermodynamic gas expansion in a supersonic nozzle

Steady thrust is given as [3]

$$F = \dot{m}u_e + (p_e - p_a)A_e \quad (2.54)$$

This equation can be modified by substituting \dot{m} and u_e with equation (2.51) and (2.46) respectively.

$$F = p_c A_t \sqrt{\frac{2\gamma^2}{\gamma - 1} \left(\frac{2}{\gamma + 1} \right)^{\frac{\gamma+1}{\gamma-1}} \left[1 - \left(\frac{p_e}{p_c} \right)^{\frac{\gamma-1}{\gamma}} \right]} + (p_e - p_a)A_e \quad (2.55)$$

p_c : Chamber pressure corresponding to the stagnation pressure

A_t : Throat sectional area corresponding to the area at sonic conditions (*)

A_e : Exit sectional area

CHAPTER II: Modelling and governing equations

Equation (2.55) is called the ideal thrust equation. It applies to an ideal rocket propulsion system with γ being constant throughout the expansion process.

A thrust coefficient C_F may now be defined as the thrust divided by the chamber pressure and the throat area.

$$C_F = \frac{F}{p_c A_t} \quad (2.56)$$

Using equation (2.55), the ideal thrust coefficient becomes

$$C_F = \sqrt{\frac{2\gamma^2}{\gamma-1} \left(\frac{2}{\gamma+1}\right)^{\frac{\gamma+1}{\gamma-1}} \left[1 - \left(\frac{p_e}{p_c}\right)^{\frac{\gamma-1}{\gamma}}\right]} + \frac{p_e - p_a}{p_c} \frac{A_e}{A_t} \quad (2.57)$$

2.4 Turbulence modelling (Spalart-Allmaras model)

The Spalart-Allmaras model [59] is a one-equation model that solves a modeled transport equation for the kinematic eddy (turbulent) viscosity variable $\tilde{\nu}$. It was developed based on empiricism, dimensional analysis and Galilean invariance. The mixing defines the transport of the turbulent viscosity.

The (dynamic) turbulent viscosity is related to $\tilde{\nu}$ by [60]

$$\mu_t = \rho \tilde{\nu} f_{v1} \quad (2.55)$$

Equation (2.55) contains the wall-damping function $f_{v1} = f_{v1}(v/\tilde{\nu})$, which tends to unity for high Reynolds numbers, so the kinematic eddy viscosity parameter $\tilde{\nu}$ is just equal to the kinematic eddy viscosity μ_t in this case. At the wall the damping function f_{v1} tends to zero.

The Spalart-Allmaras model was designed specifically for aerospace applications involving wall-bounded flows and has been shown to give good results for boundary layers subjected to adverse pressure gradients. Furthermore, it is capable of smooth transition from laminar to turbulent flow at user specified locations. The Spalart-Allmaras model has several favorable numerical features. It is “local” which means that the equation at one point does not depend on the solution at other points. Therefore, it can be readily implemented on structured multi-block or on unstructured grids. It is also robust, converges fast to steady-state and requires only moderate grid resolution in the near-wall region.

The transported variable in the Spalart-Allmaras model is identical to the turbulent kinematic viscosity except in the near-wall (viscosity-affected) region. The transport equation for the modified turbulent viscosity is:

CHAPTER II: Modelling and governing equations

$$\frac{D\rho\tilde{v}}{Dt} = c_{b1}\rho\tilde{S}\tilde{v} + \frac{1}{\rho} + [\nabla \cdot ((\mu + \rho\tilde{v})\nabla\tilde{v}) + c_{b2}\rho(\nabla\tilde{v})^2] - c_{\omega1}\rho f_{\omega} \left(\frac{\tilde{v}}{d}\right)^2 \quad (2.58)$$

where μ is the molecular viscosity of the fluid, d is the distance to the nearest wall, $v_t = f_{v1}\tilde{v}$ is the turbulent viscosity, f_{v1} is damping function which assure that $\tilde{v} = ky u_t$ (u_t is friction velocity) in the various areas of the boundary layer (linear, plug and logarithmic curve)

$$f_{v1} = \frac{x^3}{x^3 + c_{v1}^3} \quad (2.59)$$

with, $x = \frac{\tilde{v}}{v}$

in addition:

$$\tilde{S} = \sqrt{2\Omega_{ij}\Omega_{ij}} + \frac{\tilde{v}}{k^2 d^2} f_{v2} \text{ With } f_{v2} = 1 - \frac{x}{1 + x f_{v1}} \text{ and } \Omega_{ij} = \frac{1}{2} \left(\frac{\partial u_i}{\partial x_j} - \frac{\partial u_j}{\partial x_i} \right) \quad (2.60)$$

$$f_{\omega}(g) = g \left(\frac{1 + c_{\omega3}^6}{g^6 + c_{\omega3}^6} \right)^{1/6} \text{ With } g = r + c_{\omega2}(r^6 - r) \text{ and, } r = \frac{\tilde{v}}{\tilde{S} k^2 d^2} \quad (2.61)$$

Model constants are as follows [60]:

$$c_{\omega1} = \frac{c_{b1}}{k} + \frac{(1 + c_{b1})}{\sigma}, c_{b1} = 0,1355, c_{b2} = 0,622, \sigma = 2/3 \text{ and } k = 0,41 \quad (2.62)$$

$$c_{\omega2} = 0,3, c_{\omega3} = 2 \quad c_{v1} = 7.1$$

In the transport equation of \tilde{v} , the term of destruction depends on the distance to the wall. That makes it possible to ensure that sufficient quantity of viscosity is injected according to the position in the boundary layer. The action of this term is all the more important as the distance to the wall is weak. In the external zone of the boundary layer on the other hand, the decrease of the term of destruction is accelerated by the function of correction f_{ω} [61].

2.5 Finite volume formulation [62]

The resolution of the governing equations in time and space can done either by an exact or averaged (in a Favre form) solution. In this case, Ansys-Fluent® is used to solve the whole system of governing equations for the flow variables.

Discretization i.e. integration is the integration of the governing equation (or equations) over a control volume is done by finite volume method.

• **Momentum equation according to OX**

$$\frac{\partial}{\partial x}(\rho u \cdot u) + \frac{\partial}{\partial y}(\rho v \cdot u) = -\frac{\partial P}{\partial x} + \frac{\partial}{\partial x}\left(\mu \frac{\partial u}{\partial x}\right) + \frac{\partial}{\partial y}\left(\mu \frac{\partial u}{\partial y}\right) \quad 2.63$$

Consider the staggered grid (Fig.2.1) for “u”, with a control volume ΔV_u .

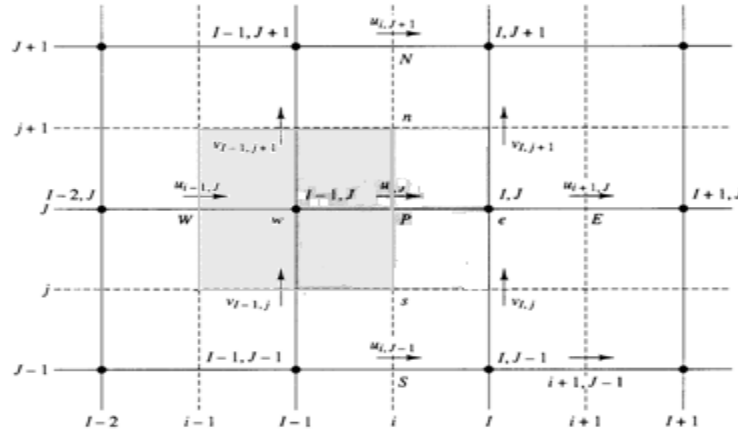


Figure 2.1: Grid

The point “P” is the pivot point where we want to calculate the component “u” of the flight path vector localized on a node of index (i, J). This will be the case for all the nearby nodes intended for the calculation of the component “u”. On the other hand, the second component for velocity “v” is calculated on nodes located in places of the type (I, j). Noting that the lines “i” and columns “j” are upstream of the lines “I” and “J”, we intend to make a “regressive shift (backward staggering)” in the equations.

The integral form of equation (63):

$$\int_{\Delta A_u} \frac{\partial}{\partial x}(\rho u \cdot u) dA + \int_{\Delta A_u} \frac{\partial}{\partial y}(\rho v \cdot u) dA = \int_{\Delta A_u} -\frac{\partial P}{\partial x} dA + \int_{\Delta A_u} \frac{\partial}{\partial x}\left(\mu \frac{\partial u}{\partial x}\right) dA + \int_{\Delta A_u} \frac{\partial}{\partial y}\left(\mu \frac{\partial u}{\partial y}\right) dA \quad (2.64)$$

$\Delta A_u, \Delta V_u$ represent respectively the surface of the one of the four faces (e, w, n, s) of the volume of the cell “u” and the control volume of the same cell.

The discrete form of the integral expression is written:

CHAPTER II: Modelling and governing equations

$$(F_e A_e u_e - F_w A_w u_w) + (F_n A_n u_n - F_s A_s u_s) = \mu_e A_e \frac{u_E - u_P}{\delta x_{EP}} - \mu_w A_w \frac{u_P - u_W}{\delta x_{WP}} + \mu_n A_n \frac{u_N - u_P}{\delta y_{nP}} +$$

$$- \mu_s A_s \frac{u_P - u_S}{\delta y_{SP}} - \frac{P_e - P_w}{\delta x_{ew}} \Delta V_u \quad 2.46 \quad (2.65)$$

It is can be seen that in the shifted cell (staggered cell), the nodes of the type (e, w, n, s) are in positions of the type (I, J), these positions are the ones that are used to evaluate the scalar quantities (pressure, temperature, laminar viscosity, density).

$F = \rho u$ (or ρv) corresponds to the mass flows through the faces of edge of the cell “u”.

Pressures P_e, P_w are scalars and they are evaluated directly in their positions $P_e = P_{I,J}$ $P_w = P_{I-1,J}$ The values of the component of the velocity “u”, namely u_E, u_W, u_N, u_S are evaluated in their positions since they belong to the nodes of the shifted grid ($E = (i + 1, J), W = (i - 1, J), N = (i, J + 1), S = (i, J - 1)$). The distances used in the discretization can be expressed according to the indices (i, j, I, J) like:

$$\delta x_{EP} = x_{i+1} - x_i, \delta x_{WP} = x_i - x_{i-1}, \delta y_{NP} = y_{J+1} - y_J, \delta y_{SP} = y_J - y_{J-1} \quad (2.66)$$

Terms of velocity “u” on the nodes (e, w, n, s) that appear in the convective terms require a special treatment. By adopting an upwind scheme which implies that the value within the node is equal to that of the node located upstream according to direction of the flow. From this fact we thus have two cases according to .i.e. whether flows of mass are positive or negative. In the first case

$$(F_e > 0, F_w > 0, F_n > 0, F_s > 0)$$

we can write:

$$u_e = u_P, u_w = u_W, u_n = u_P, u_s = u_S$$

whereas in the second case (flow negative), it is possible to write

$$u_e = u_E, u_w = u_P, u_n = u_N, u_s = u_P.$$

It is important to establish a relation which is independent of the sign of mass flows in the cells. The discrete equation 2.65 in index terms is written:

CHAPTER II: Modelling and governing equations

$$a_p u_{i,j} = a_e u_{i+1,j} + a_w u_{i-1,j} + a_n u_{i,j+1} + a_s u_{i,j-1} - A_{i,j} (P_{i,j} - P_{i-1,j}) + b_{i,j} \quad (2.67)$$

Where:

$$a_p = a_{i,j} = a_e + a_w + a_n + a_s + F_e - F_w + F_n - F_s \quad (2.68)$$

and,

$$A_{i,j} = \frac{\Delta V_u}{\delta x_{ew}} = \frac{\Delta V_u}{\delta x_u} = \frac{\Delta V_u}{x_I - x_{I-1}} \quad (2.69)$$

$$b_{i,j} = \bar{S}_{Mx} \cdot \Delta V_u, \quad \Delta V_u = \delta x_u \delta y_u$$

Terms $A_{i,j}$ represents the surface of the “east” face is noted “e” or western “w” of the cell associated with control volume “u” and $b_{i,j}$.

Coefficients “a” contain mass flows of the edge faces and the diffusion terms, and are expressed in the case of an upwind scheme like:

$$a_e = A_e [D_e + \text{Max}(F_e, 0)], \quad a_w = A_w [D_w + \text{Max}(-F_w, 0)], \quad a_n = A_n [D_n + \text{Max}(F_n, 0)], \quad (2.70)$$

$$a_s = A_s [D_s + \text{Max}(-F_s, 0)]$$

and,
$$D_e = \frac{\mu_e}{\delta x_{EP}}, \quad D_w = \frac{\mu_w}{\delta x_{WP}}, \quad D_n = \frac{\mu_n}{\delta y_{NP}}, \quad D_s = \frac{\mu_s}{\delta y_{SP}} \quad (2.71)$$

The distances between the points (E, W, N, P) are given in relation (2.65).

The laminar viscosity of the mixture is a scalar which is evaluated (and known) with the nodes of not shifted cell of type “I, J”, these values in “n and n” must be calculated by an average of all the adjacent nodes:

$$\mu_e = \mu_{I,J}, \quad \mu_w = \mu_{I-1,J}$$

$$\mu_n = \mu_{i,j+1} = \frac{\mu_{I-1,J-1} + \mu_{I,J-1} + \mu_{I,J+1} + \mu_{I-1,J+1}}{4} \quad (2.72)$$

$$\mu_s = \mu_{i,j} = \frac{\mu_{I-1,J-1} + \mu_{I,J-1} + \mu_{I,J} + \mu_{I-1,J}}{4}$$

CHAPTER II: Modelling and governing equations

Mass flows on the edge faces contain the product of a scalar (density) by a component of a vector; they are in this case discretized according to an average on the adjacent nodes, as follows:

$$F_e = (\rho u)_{I,J} = \frac{(\rho u)_{i+1,J} + (\rho u)_{i,J}}{2} = \frac{1}{2} [\rho_{i+1,J} \cdot u_{i+1,J} + \rho_{i,J} \cdot u_{i,J}] \quad (2.73)$$

However the density being a scalar, can be evaluated only on nodes of the “not shifted” cell of type (I, J), so we take the average of these nodes, like:

$$\rho_{i+1,J} = \frac{\rho_{I+1,J} + \rho_{I,J}}{2} \quad (2.74)$$

In the same way,

$$\begin{aligned} F_e &= (\rho u)_{I,J} = \frac{(\rho u)_{i+1,J} + (\rho u)_{i,J}}{2} = \frac{1}{2} \left[\frac{\rho_{I+1,J} + \rho_{I,J}}{2} \cdot u_{i+1,J} + \frac{\rho_{I,J} + \rho_{I-1,J}}{2} \cdot u_{i,J} \right] \\ F_w &= (\rho u)_{I-1,J} = \frac{1}{2} \left[\frac{\rho_{I,J} + \rho_{I-1,J}}{2} \cdot u_{i,J} + \frac{\rho_{I-1,J} + \rho_{I-2,J}}{2} \cdot u_{i-1,J} \right] \\ F_n &= (\rho v)_{i,j+1} = \frac{1}{2} \left[\frac{\rho_{I,J} + \rho_{I,J+1}}{2} \cdot v_{I,j+1} + \frac{\rho_{I-1,J} + \rho_{I-1,J+1}}{2} \cdot v_{I-1,j+1} \right] \\ F_s &= (\rho v)_{i,j} = \frac{1}{2} \left[\frac{\rho_{I,J} + \rho_{I,J-1}}{2} \cdot v_{I,j} + \frac{\rho_{I-1,J} + \rho_{I-1,J-1}}{2} \cdot v_{I-1,j} \right] \end{aligned} \quad (2.75)$$

- **Momentum equation according to OY**

The final form of the equation realized according to OY is written like:

$$\frac{\partial}{\partial x} (\rho u \cdot v) + \frac{\partial}{\partial y} (\rho v \cdot v) = -\frac{\partial P}{\partial y} + \frac{\partial}{\partial x} \left(\mu \frac{\partial v}{\partial x} \right) + \frac{\partial}{\partial y} \left(\mu \frac{\partial v}{\partial y} \right) \quad (2.76)$$

In this case, we will use another control volume relating to “v” (figure 2.2), where the components “v” velocity will be evaluated on nodes of the type (I,J).

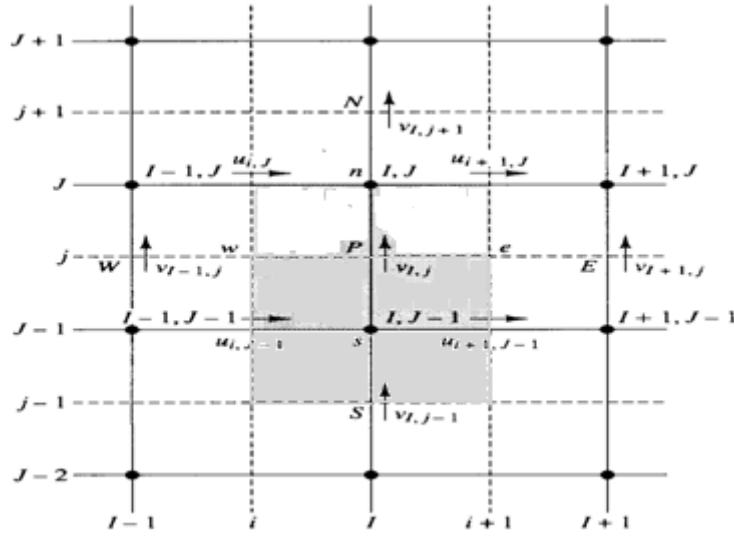


Figure 2.2: v Staggered grid

In same manner as in the case of the equation according to OX, we lead to a discrete form of the equation of momentum according to OY:

$$a_p v_{I,j} = a_e v_{I+1,j} + a_w v_{I-1,j} + a_n v_{I,j+1} + a_s v_{I,j-1} - A_{I,j} (P_{I,j} - P_{I,j-1}) + b_{I,j} \quad (2.77)$$

where,

$$a_p = a_{I,j} = a_e + a_w + a_n + a_s + F_e - F_w + F_n - F_s \quad (2.78)$$

and,

$$A_{I,j} = \frac{\Delta V_v}{\delta y_{ns}} = \frac{\Delta V_u}{\delta y_v} = \frac{\Delta V_u}{y_j - y_{j-1}} \quad (2.79)$$

$$b_{I,j} = \bar{S}_{My} \cdot \Delta V_v, \quad \Delta V_v = \delta x_v \delta y_v$$

Terms $A_{I,j}$ represents the “northern” surface face noted “n” or “s” for “southern” surface face noted “s” of the cell associated with control volume “v” and $b_{I,j}$.

The coefficients of the equation 2.77 and in the case of an Upwind-scheme are expressed by a general form independent of the direction of flow:

CHAPTER II: Modelling and governing equations

$$\begin{aligned} a_e &= A_e [D_e + \text{Max}(-F_e, 0)], \quad a_w = A_w [D_w + \text{Max}(F_w, 0)], \quad a_n = A_n [D_n + \text{Max}(-F_n, 0)], \\ a_s &= A_s [D_s + \text{Max}(F_s, 0)] \end{aligned} \quad (2.80)$$

and,

$$a_p = a_{I,j} = a_e + a_w + a_n + a_s + F_e - F_w + F_n - F_s,$$

with:

$$\begin{aligned} D_e &= \frac{\mu_e}{\delta x_{EP}}, \quad D_w = \frac{\mu_w}{\delta x_{WP}}, \quad D_n = \frac{\mu_n}{\delta y_{NP}}, \quad D_s = \frac{\mu_s}{\delta y_{SP}} \\ \delta x_{EP} &= x_{I+1} - x_I, \quad \delta x_{WP} = x_I - x_{I-1}, \quad \delta y_{NP} = y_{j+1} - y_j, \quad \delta y_{SP} = y_j - y_{j-1} \end{aligned} \quad (2.81)$$

The scalar terms located on the nodes “n, s” are evaluated directly, whereas the others (located in “e, w”) are interpolated starting from the adjacent nodes:

$$\begin{aligned} \mu_n &= \mu_{I,J}, \quad \mu_s = \mu_{I,J-1} \\ \mu_e &= \mu_{i+1,j} = \frac{\mu_{I,J-1} + \mu_{I+1,J-1} + \mu_{I+1,J} + \mu_{I,J}}{4} \\ \mu_w &= \mu_{i,j} = \frac{\mu_{I,J-1} + \mu_{I,J} + \mu_{I-1,J} + \mu_{I-1,J-1}}{4} \end{aligned} \quad (2.82)$$

In the same manner as in the equation according to (OX), the terms of flow of mass are discretized as (knowing that in this case the averages are caught according to adjacent nodes' in direction OY):

$$\begin{aligned} F_e &= (\rho u)_{i+1,j} = \frac{(\rho u)_{i+1,J} + (\rho u)_{i+1,J-1}}{2} = \frac{1}{2} \left[\frac{\rho_{I+1,J} + \rho_{I,J}}{2} \cdot u_{i+1,J-1} + \frac{\rho_{I,J-1} + \rho_{I+1,J-1}}{2} \cdot u_{i+1,J} \right] \\ F_w &= (\rho u)_{i,j} = \frac{1}{2} \left[\frac{\rho_{I,J} + \rho_{I-1,J}}{2} \cdot u_{i,J} + \frac{\rho_{I-1,J-1} + \rho_{I,J-1}}{2} \cdot u_{i,J-1} \right] \\ F_n &= (\rho v)_{I,J} = \frac{1}{2} \left[\frac{\rho_{I,J} + \rho_{I,J-1}}{2} \cdot v_{I,j} + \frac{\rho_{I,J+1} + \rho_{I,J}}{2} \cdot v_{I,j+1} \right] \\ F_s &= (\rho v)_{I,J-1} = \frac{1}{2} \left[\frac{\rho_{I,J-1} + \rho_{I,J-2}}{2} \cdot v_{I,j-1} + \frac{\rho_{I,J} + \rho_{I,J-1}}{2} \cdot v_{I,j} \right] \end{aligned}$$

2.6 Discretization schemes for convective terms (Roe) [59]:

2.6.1 Governing equations in vector form

CHAPTER II: Modelling and governing equations

The system of governing equations for a single-component fluid, written to describe the mean flow properties, is cast in integral Cartesian form for an arbitrary control volume V with differential surface area dA as follows [59]:

$$\frac{\partial}{\partial t} \int_V W dV + \oint [F-G] \cdot dA = \int_V H dV \quad (2.83)$$

Where the vectors W , F , and G are defined as:

$$W = \begin{Bmatrix} \rho \\ \rho u \\ \rho v \\ \rho w \\ \rho E \end{Bmatrix}, F = \begin{Bmatrix} \rho v \\ \rho v u + p \hat{i} \\ \rho v v + p \hat{j} \\ \rho v w + p \hat{k} \\ \rho v E + p v \end{Bmatrix}, G = \begin{Bmatrix} 0 \\ \tau_{xi} \\ \tau_{yi} \\ \tau_{zi} \\ \tau_{ij} v_j + q \end{Bmatrix} \quad (2.84)$$

And the vector H contains source terms such as body forces and energy sources.

ρ : Density of the fluid

v : Velocity of the fluid

p : Pressure of the fluid

E : Total energy per unit mass

τ : Viscous stress tensor

q : Heat flux

E is related to total enthalpy by $H = p/\rho$ where, $H = h + |v^2|/2$

Derivation of the preconditioning matrix begins by transforming the dependent variable in (2.83) from conserved quantities to primitive variables using the chain-rule as follows:

$$\frac{\partial W}{\partial Q} \frac{\partial}{\partial t} \int_V Q dV + \oint [F-G] \cdot dA = \int_V H dV \quad (2.85)$$

where Q is the vector $\{p, u, w, T\}^T$ and the Jacobian $\frac{\partial W}{\partial Q}$ is given by:

CHAPTER II: Modelling and governing equations

$$\frac{\partial W}{\partial Q} = \begin{bmatrix} \rho_p & 0 & 0 & 0 & \rho_T \\ \rho_p u & \rho & 0 & 0 & \rho_T u \\ \rho_p v & 0 & \rho & 0 & \rho_T v \\ \rho_p w & 0 & 0 & \rho & \rho_T w \\ \rho_p H - \delta & \rho u & \rho v & \rho w & \rho_T H + \rho C_p \end{bmatrix} \quad (2.86)$$

where,

$$\rho_p = \left. \frac{\partial \rho}{\partial p} \right|_T, \rho_T = \left. \frac{\partial \rho}{\partial T} \right|_p$$

And $\delta = 1$ for an ideal gas, and $\delta = 0$ for an incompressible fluid.

We precondition the system by replacing the Jacobian matrix $\frac{\partial W}{\partial Q}$ (2.86) with the preconditioning matrix Γ so that the preconditioned system in conservation form becomes:

$$\Gamma \frac{\partial}{\partial t} \int_V Q dV + \oint [F-G] \cdot dA = \int_V H dV \quad (2.87)$$

where,

$$\Gamma = \begin{bmatrix} \theta & 0 & 0 & 0 & \rho_T \\ \theta u & \rho & 0 & 0 & \rho_T u \\ \theta v & 0 & \rho & 0 & \rho_T v \\ \theta w & 0 & 0 & \rho & \rho_T w \\ \theta H - \delta & \rho u & \rho v & \rho w & \rho_T H + \rho C_p \end{bmatrix} \quad (2.88)$$

The parameter θ is given by

$$\theta = \left(\frac{1}{U_r^2} - \frac{\rho_T}{\rho C_p} \right) \quad (2.89)$$

CHAPTER II: Modelling and governing equations

The reference velocity appearing in (2.89) is chosen locally such that the eigenvalues of the system remain well conditioned with respect to the convective and diffusive time scales [63].

2.6.2 Roe Flux-Difference Splitting Scheme:

The inviscid flux vector F appearing in (2.87) is evaluated by a standard upwind, flux difference splitting. This approach acknowledges that the flux F vector contains characteristic information propagating through the domain with speed and direction according to the eigenvalues of the system. By splitting F into parts, where each part contains information traveling in a particular direction (that is, characteristic information), and upwind differencing the split fluxes in a manner consistent with their corresponding eigenvalues, we obtain the following expression for the discrete flux at each face [59]:

$$F = \frac{1}{2}(F_R + F_L) - \frac{1}{2}\Gamma|\hat{A}|\delta Q \quad (2.90)$$

Here δQ is the spatial difference $Q_R - Q_L$. The flux $F_R = F(Q_R)$ and $F_L = F(Q_L)$ are computed using the (reconstructed) solution vectors Q_R and Q_L on the “right” and “left” side of the face. The matrix $|\hat{A}|$ is defined by:

$$|\hat{A}| = M|\Lambda|M^{-1} \quad (2.91)$$

Where Λ is the diagonal matrix of eigenvalues and M is the modal matrix that diagonalizes $\Gamma^{-1}A$, where A is the inviscid flux Jacobian $\frac{\partial F}{\partial Q}$.

For the non-preconditioned system (and an ideal gas) (2.90) reduces to Roe’s flux-difference splitting [64], when Roe-averaged values are used to evaluate $\Gamma|\hat{A}|$. At present, arithmetic averaging of states Q_R and Q_L is used.

CHAPTER II: Modelling and governing equations

Conclusion

A first assumption is to qualify the compressible flow within the nozzle as 1D in a stationary regime. Indeed, this is a way to neglect the different losses (by divergence, by turbulence, by convection...) and achieve the ideal performances of the nozzle, by using the relations derived in the first part of this chapter. The second part was devoted to the FV formulation of the 'realistic' governing equations, where turbulence, divergence and shock separation were considered. Solving the set of continuity, momentum, energy and turbulence equations is expected to be undertaken by mean of the Ansys-Fluent software. Details on grid generation, BC, solution control and numerical results regarding compressible flow within an experimental overexpanded nozzle, will be performed in the next chapter.

CHAPTER III: Results and discussions

Introduction

This chapter covers the main objective of this present work. It presents the computational results obtained by means of the Ansys-Fluent[®] (19.2 Release) computational fluid dynamics (CFD) software [2]. This chapter is divided into five (5) parts. The first part covers the geometric description of the DRL-TIC nozzle model. In the second part, thermodynamic relations are applied to predict the operating parameters of the model for the given conditions. Thirdly, numerical methodology is outlined. This includes definition of the geometry, grid generation and boundary conditions. The fourth part is dedicated to the discussion of the numerical results. In addition, the numerical results are compared with experimental data of Stark and Al [1] for model validation. This study is completed with a parametric analysis for the different CFD simulation scenarios.

3.1 Baseline model description

The nozzle model studied in this computational work is the truncated ideal contour (TIC) subscale nozzle used by the German Aerospace Center (DRL) in the cold flow test campaigns of the European FSCD group, in the view of validating turbulence models and characterizing boundary layer separation and the related flow field in nozzles. It was the subject of study in the computational work carried out by Stark and Hagemann [1] with the objective to compute the flow inside a strongly overexpanded truncated ideal contour nozzle with respect to the prediction of location and shape of the flow separation, the oblique shock and the Mach disc [1].



Figure 3.1: Acrylic glass TIC nozzle with transducer ports [1]

The test specimen used in these cold flow test campaigns was made of acrylic glass, with a throat diameter of 20mm, an overall divergent length of 90mm, a wall thickness of 11.5mm, and a design Mach number of 5.15. Figure 3.2 shows the geometric model for the DRL-TIC nozzle.

Table 3.1: Geometric properties of the DRL-TIC nozzle [1]

Convergent length (mm)	$L_{cv} = 25.8$
Divergent length (mm)	$L_{div} = 90.0$
Chamber diameter (mm)	$\phi_c = 40.0$
Throat diameter (mm)	$\phi_t = 20.0$
Exit diameter (mm)	$\phi_e = 74.88$

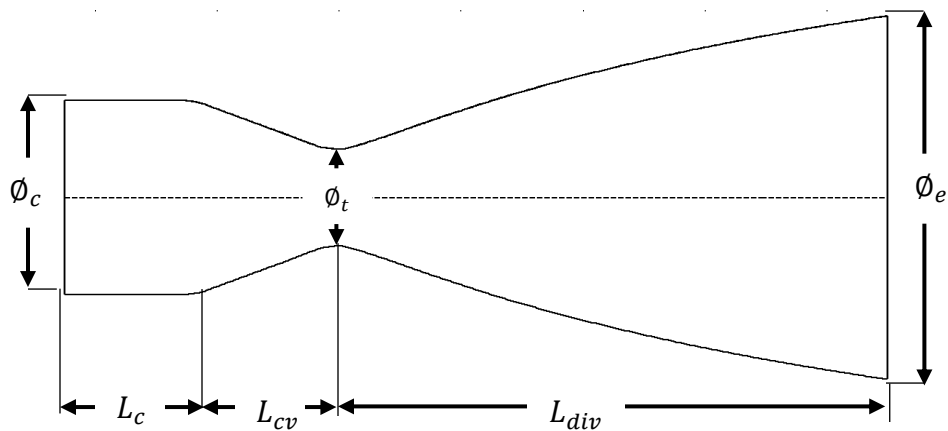


Figure 3.2: Geometric model for the DRL-TIC nozzle

3.2 Experimental operating conditions

The data used in this work is obtained from the experiments conducted at DLR's cold flow test facility P6.2 in Lampoldshausen, Germany [1]. As fluid, dry gaseous nitrogen N_2 is used, stored in high pressure tanks at 25.25 bar and 283K. The nitrogen flow then accelerates in a convergent-divergent nozzle to supersonic velocity and exits the nozzle to an ambient pressure and temperature of 1 Bar and 270 K respectively.

A sketch of the experimental setup is shown below.

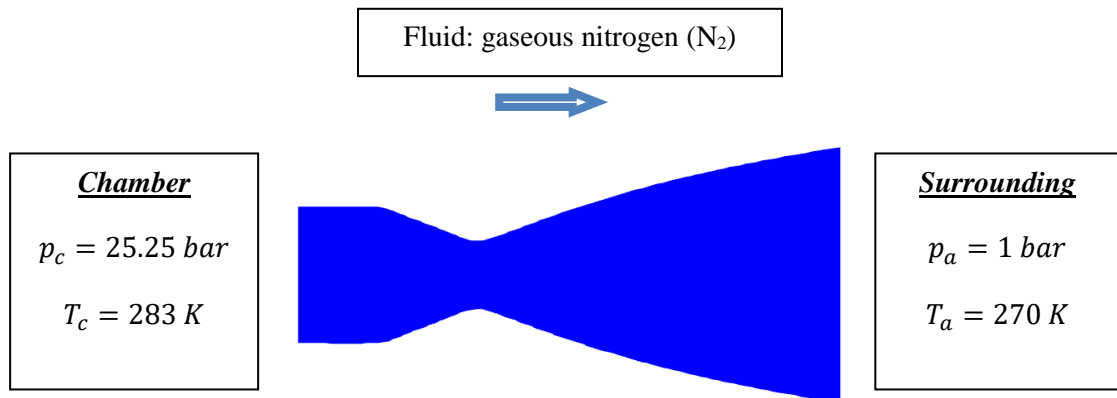


Figure 3.3: Experimental operating conditions

3.3 Prediction of nozzle flow conditions

Prediction of operating parameters for any system that uses thermodynamic gas expansion in the nozzle can be done using mathematical relations obtained from gas dynamics principles covered in chapter 2. The equations for an assumed quasi-one-dimensional nozzle flow, represent an idealization and simplification of the full two- or three-dimensional equations of real aerothermochemical behavior.

In the thermodynamic calculations two (02) important factors are going to be used .i.e. the ratio of specific heats γ and the specific gas constant r . The ratio of specific heats is important for its

CHAPTER III: Results and discussions

application in thermodynamical reversible processes and the specific gas constant is required in which a gas dynamic network is included. The speed of sound also depends on these factors.

The relation of the gas constant is given as [13]:

$$r = \frac{R}{M} \left[\frac{J}{kg.K} \right] \quad (3.1)$$

where M is the molar mass of the gas [mole/kg] and R [J/(kg.mol.K)] is the universal gas constant.

The ratio of specific heats is calculated as:

$$\gamma = \frac{c_p}{c_v} \quad (3.2)$$

where c_p and c_v are specific heats [J/(kg.K)] at constant pressure and volume which can be obtained from thermodynamics tables.

For a calorifically perfect gas, the specific heats are constant. In real gas behavior, the specific heats c_p and c_v vary somewhat with temperature, however their ratio does not exhibit much change except over large temperature ranges. Thus the assumption of constant γ generally leads to acceptable engineering accuracy.

In the following calculations, N₂ is assumed to be a perfect gas with a gas constant $r = 296.8 \text{ J/kg}$ and ratio of specific heat $\gamma = 1.4005$.

3.3.1 Nozzle Inlet

Mach number

At the inlet, the Mach number is subsonic which can be computed from the area ratio using different methods, for example, Initial guess, Newton-Raphson, A Higher-Order Method etc. The contraction ratio can be given as [3]:

$$\frac{A}{A_t} = \frac{1}{M} \left[\frac{1 + \left(\frac{\gamma - 1}{2} \right) M^2}{\frac{\gamma + 1}{2}} \right]^{\frac{\gamma + 1}{2(\gamma - 1)}} \quad (3.3)$$

CHAPTER III: Results and discussions

Where A_t stands for the throat sectional area, and:

$$M_{i+1} = \frac{A_t}{A_i} \left[\frac{1 + \left(\frac{\gamma - 1}{2}\right) M_i^2}{\frac{\gamma + 1}{2}} \right]^{\frac{\gamma + 1}{2(\gamma - 1)}} \quad (3.4)$$

The chamber contraction ratio is calculated as:

$$\epsilon_c = \frac{A_c}{A_t} = \frac{\pi r_c^2}{\pi r_t^2} = \left(\frac{r_c}{r_t}\right)^2 = \left(\frac{20}{10}\right)^2 = 4.0 \quad (3.5)$$

To compute the Mach number using the area ratio equation (3.3), the fixed point method is used. In this method the equation is solved using an iterative process which requires a starting solution. The computational sequences are as follows:

M (1) =0,5	M(1) =1	M(1) =2
M(2)=0.16748046875	M(2)= 0.25	M(2)= 0.84375
M(3)= 0.147124481384679	M(3)= 0.150169372558594	M(3)= 0.215690616458973
M(4)= 0.14656303137364	M(4)= 0.146642306259479	M(4)= 0.148752024197441
M(5)= 0.14654859420769	M(5)= 0.146550629283628	M(5)= 0.146605199488069
M(6)= 0.1465482237098	M(6)= 0.14654827593327	M(6)= 0.146549676571515
M(7)= 0.146548214202281	M(7)= 0.14654821554241	M(7)= 0.146548251484984
M(8)= 0.146548213958305	M(8)= 0.146548213992694	M(8)= 0.146548214915032
M(9)= 0.146548213952044	M(9)= 0.146548213952926	M(9)= 0.146548213976595
M(10)= 0.146548213951883	M(10)=0.146548213951906	M(10)= 0.146548213952513
M(11)=0.146548213951879	M(11)= 0.14654821395188	M(11)= 0.146548213951895
M(12)=0.146548213951879	M(12)=0.146548213951879	M(12)= 0.146548213951879
M(13)=0.146548213951879	M(13)=0.146548213951879	M(13)= 0.146548213951879
M(14)=0.146548213951879	M(14)=0.146548213951879	M(14)= 0.146548213951879

$$M_{sub} = 0.147$$

CHAPTER III: Results and discussions

Static Temperature

$$\frac{T_0}{T} = \left(1 + \frac{\gamma - 1}{2} M_i^2\right) \quad (3.6)$$

$$\frac{T_0}{T_{in}} = \left(1 + \frac{\gamma - 1}{2} M_{sub}^2\right) \rightarrow T_{in} = T_0 \left(1 + \frac{\gamma - 1}{2} M_{sub}^2\right)^{-1}$$

where $T_0 = T_c = 283 \text{ K}$

$$T_{in} = 281.79 \text{ K}$$

Static Pressure

$$\frac{p_0}{p} = \left(1 + \frac{\gamma - 1}{2} M_i^2\right)^{\frac{\gamma}{\gamma - 1}} \quad (3.7)$$

$$\frac{p_0}{p_{in}} = \left(1 + \frac{\gamma - 1}{2} M_{sub}^2\right)^{\frac{\gamma}{\gamma - 1}} \rightarrow p_{in} = p_0 \left(1 + \frac{\gamma - 1}{2} M_{sub}^2\right)^{-\frac{\gamma}{\gamma - 1}}$$

where $p_0 = p_c = 25.25 \text{ bar}$

$$p_{in} = 24.874 \text{ bar}$$

Density

$$\rho = \frac{p}{r \times T} \quad (3.8)$$

$$\rho_{in} = \frac{p_{in}}{r \times T_{in}}$$

$$\rho_{in} = 30.115 \text{ kg/m}^3$$

Velocity

$$M = \frac{u}{a} \rightarrow u = M \times a \quad (3.9)$$

$$a = \sqrt{\gamma r T} \quad (3.10)$$

$$u = M \sqrt{\gamma r T}$$

CHAPTER III: Results and discussions

$$u_{in} = M_{sub} \sqrt{\gamma r T_{in}}$$

$$u_{in} = 50.163 \text{ ms}^{-1}$$

Mass flow rate

$$\dot{m} = \rho u A \quad (3.11)$$

$$\dot{m} = \rho_{in} u_{in} A_c$$

$$\dot{m}_{in} = 1.898 \text{ kg/s}$$

3.3.2 Nozzle throat

Mach number

$$M_t = 1$$

Static Temperature

$$\frac{T_0}{T_t} = \left(1 + \frac{\gamma - 1}{2} M_t^2\right) \rightarrow T_t = T_0 \left(1 + \frac{\gamma - 1}{2} M_t^2\right)^{-1}$$

$$T_t = 235.83 \text{ K}$$

Static Pressure

$$\frac{p_0}{p_t} = \left(1 + \frac{\gamma - 1}{2} M_t^2\right)^{\frac{\gamma}{\gamma - 1}} \rightarrow p_t = p_0 \left(1 + \frac{\gamma - 1}{2} M_t^2\right)^{-\frac{\gamma}{\gamma - 1}}$$

$$p_t = 13.339 \text{ bar}$$

Density

$$\rho_t = \frac{p_t}{r \times T_t}$$

$$\rho_t = 19.31 \text{ kg/m}^3$$

Velocity

$$u = M_t \sqrt{\gamma r T_t}$$

$$u_t = \sqrt{\gamma r T_t} = a$$

$$u_t = 313.039 \text{ ms}^{-1}$$

CHAPTER III: Results and discussions

Mass flow rate

$$\dot{m} = \rho_t u_t A_t$$

$$\dot{m}_t = 1.898 \text{ kg/s}$$

3.3.3 Nozzle exit

Mach number

$$M_{i+1} = \sqrt{\left(\left(\left(\left(\left(\left(\frac{A_i}{A_t} \times M_i \right)^{\frac{2(\gamma-1)}{\gamma+1}} \right) \left(\frac{\gamma+1}{2} \right) \right) - 1 \right) \left(\frac{2}{\gamma-1} \right) \right) \right)} \quad (3.12)$$

$$\epsilon_e = \frac{A_e}{A_t} = \frac{\pi r_e^2}{\pi r_t^2} = \left(\frac{r_e}{r_t} \right)^2 = \left(\frac{37.44}{10} \right)^2 = 14.017536 = 14.02$$

$$\mathbf{M_{sup} = 4.305}$$

Static Temperature

$$\frac{T_0}{T_e} = \left(1 + \frac{\gamma-1}{2} M_{sup}^2 \right) \rightarrow T_e = T_0 \left(1 + \frac{\gamma-1}{2} M_{sup}^2 \right)^{-1}$$

$$T_e = 60.124 \text{ K}$$

Static Pressure

$$\frac{p_0}{p_e} = \left(1 + \frac{\gamma-1}{2} M_{sup}^2 \right)^{\frac{\gamma}{\gamma-1}} \rightarrow p_e = p_0 \left(1 + \frac{\gamma-1}{2} M_{sup}^2 \right)^{-\frac{\gamma}{\gamma-1}}$$

$$p_e = 0.112 \text{ bar}$$

Density

$$\rho_e = \frac{p_e}{r \times T_e}$$

$$\rho_e = 0.633 \text{ kg/m}^3$$

Velocity

CHAPTER III: Results and discussions

$$u_e = M_{sup} \sqrt{\gamma r T_e}$$
$$u_e = 680.704 \text{ ms}^{-1}$$

Mass flow rate

$$\dot{m}_e = \rho_e u_e A_e$$
$$\dot{m}_e = 1.898 \text{ kg/s}$$

From the thermodynamic calculations, the design exit pressure is found to be less than that of the surrounding. This in tells that the nozzle is operating in an overexpansion regime.

The conservation of mass can be seen from the fact that the mass flow rate at the prescribed cross-sectional areas constant. This is a proper indication that this thermodynamic formulation is suitable and has been well applied.

3.4 Flow regime across the nozzle

In determining whether the flow is laminar or turbulent, a dimensionless grouping of parameters called the Reynolds number is used [58].

$$Re = \frac{\rho u \phi}{\mu} \quad (3.13)$$

where; ρ is the fluid density, u is the fluid velocity, ϕ is the diameter and μ the viscosity of the fluid.

The viscosity is assumed constant and equals $\mu = 1.663 \times 10^{-5} \text{ kgm}^{-1}\text{s}^{-1}$ at standard conditions.

The Reynolds number is evaluated at each cross-sectional area of the nozzle, as:

Nozzle inlet

$$\rho_{in} = 30.115 \text{ kg/m}^3, u_{in} = 50.163 \text{ ms}^{-1}, \phi_c = 0.04 \text{ m}$$
$$Re_{in} = \frac{\rho_{in} u_{in} \phi_c}{\mu}$$
$$Re_{in} = 3.634 \times 10^6$$

CHAPTER III: Results and discussions

Nozzle throat

$$\rho_t = 19.31 \text{ kg/m}^3, u_t = 313.309 \text{ ms}^{-1}, \phi_t = 0.02 \text{ m}$$

$$Re_t = \frac{\rho_t u_t \phi_t}{\mu}$$

$$Re_t = 7.27 \times 10^6$$

Nozzle exit section

$$\rho_e = 0.633 \text{ kg/m}^3, u_e = 680.704 \text{ ms}^{-1}, \phi_e = 0.07488 \text{ m}$$

$$Re_e = \frac{\rho_e u_e \phi_e}{\mu}$$

$$Re_e = 1.941 \times 10^6$$

The Reynolds values computed across the prescribed sectional-areas of the nozzle .i.e. inlet, throat and exit are over 10^6 which indicates that the flow is fully turbulent and no transition occurs in its pattern.

3.5 Nozzle theoretical performances

Inasmuch as the studied experimental case is an overexpanded nozzle, experiments on nozzle flow may also be performed on either a sea-level adapted nozzle ($p_e = p_a = 1 \text{ bar}$) or a vacuum adapted nozzle ($p_e = p_a = 0 \text{ bar}$). These nozzles produce different thrust force which can be determined using thermodynamic relations:

i. Adaptation conditions : $p_e = p_a$

a. $p_e = p_a = 0 \text{ bar}$ (Vacuum)

$$C_F = \gamma \sqrt{\frac{2}{\gamma-1} \left(\left(\frac{2}{\gamma+1} \right)^{\frac{\gamma+1}{\gamma-1}} \right) \left[1 - \left(\frac{p_e}{p_c} \right)^{\frac{\gamma-1}{\gamma}} \right]} + \left(\frac{p_e}{p_c} - \frac{p_a}{p_c} \right) \epsilon_e = 1.812 \quad (3.14)$$

b. $p_e = p_a = 1 \text{ bar}$ (Sea level)

$$C_F = \gamma \sqrt{\frac{2}{\gamma-1} \left(\left(\frac{2}{\gamma+1} \right)^{\frac{\gamma+1}{\gamma-1}} \right) \left[1 - \left(\frac{p_e}{p_c} \right)^{\frac{\gamma-1}{\gamma}} \right]} + \left(\frac{p_e}{p_c} - \frac{p_a}{p_c} \right) \epsilon_e = 1.406$$

CHAPTER III: Results and discussions

ii. Overexpansion conditions; $NPR = \frac{p_c}{p_a} = \frac{25.25}{1} = 25.25$

$$p_e = 0.112 \text{ bar}$$

$$C_F = \gamma \sqrt{\frac{2}{\gamma-1} \left(\left(\frac{2}{\gamma+1} \right)^{\frac{\gamma+1}{\gamma-1}} \right) \left[1 - \left(\frac{p_e}{p_c} \right)^{\frac{\gamma-1}{\gamma}} \right] + \left(\frac{p_e}{p_c} - \frac{p_a}{p_c} \right)} \epsilon_e = 1.115$$

Thrust efficiency represented by the thrust coefficient is proportional to exhaust velocity. From a thermodynamics point of view, the exhaust velocity is a function of $\left(\frac{p_e}{p_c} \right)^{\frac{\gamma-1}{\gamma}}$ (3.14) and for vacuum, p_e is almost equal to zero making the term above equal to zero hence the exhaust velocity is maximum.

For sea level conditions, the term $\left(\frac{p_e}{p_c} \right)^{\frac{\gamma-1}{\gamma}}$ does not reduce to zero hence the exhaust is less compared to that in the vacuum with a deviation of -22.41%.

Overexpanded flows are characterized with loss in thrust efficiency. As already described in chapter 1, the second term in the equation (1.1) for the thrust is negative resulting in a decrease in thrust coefficient. The relative deviation compared with vacuum and sea level conditions are -38.41% and -20.7 % respectively indicating a high loss in thrust performance.

3.6 Numerical calculations

Navier -Stokes equations, energy and turbulence equations were averaged in a Favre form, using Ansys-Fluent[®]. Density based solver with implicit time integration is used to obtain steady state solutions. The inviscid fluxes are discretized using ROE flux difference splitting scheme. The solution is second order accurate in space. Spalart-Allmaras turbulence model is used to account for the turbulence effects. For the scaled residuals, 10^{-6} was adopted for the energy, momentum and μ_t equations while 10^{-3} was adopted for the continuity equation. A net mass flow rate of 10^{-4} was adopted as the convergence criteria.

3.6.1 Computational domain and boundary conditions

CHAPTER III: Results and discussions

The solution domain consists of 2 sub-domains; the converging-diverging nozzle (Fig.3.4.a) and a large extension ($12.5\phi_{in} \times 10\phi_{in}$ caisson) as shown in figure 3.4.b. The purpose of the extension is to avoid disturbing the flow at the exit section, such that a Dirichlet condition for the ambient pressure, p_a could be imposed at the far-field of the nozzle.

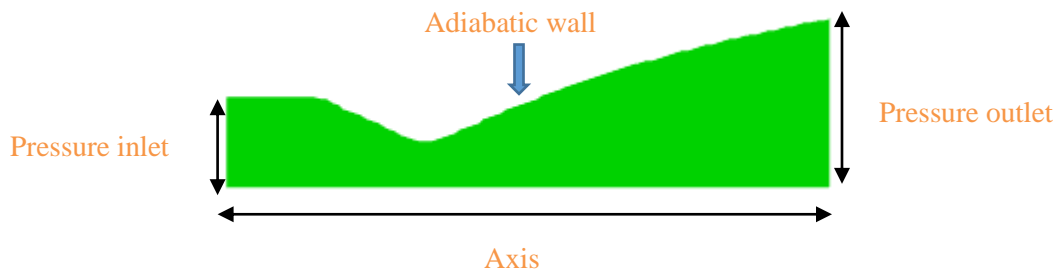


Figure 3.4.a: Nozzle domain with boundary conditions

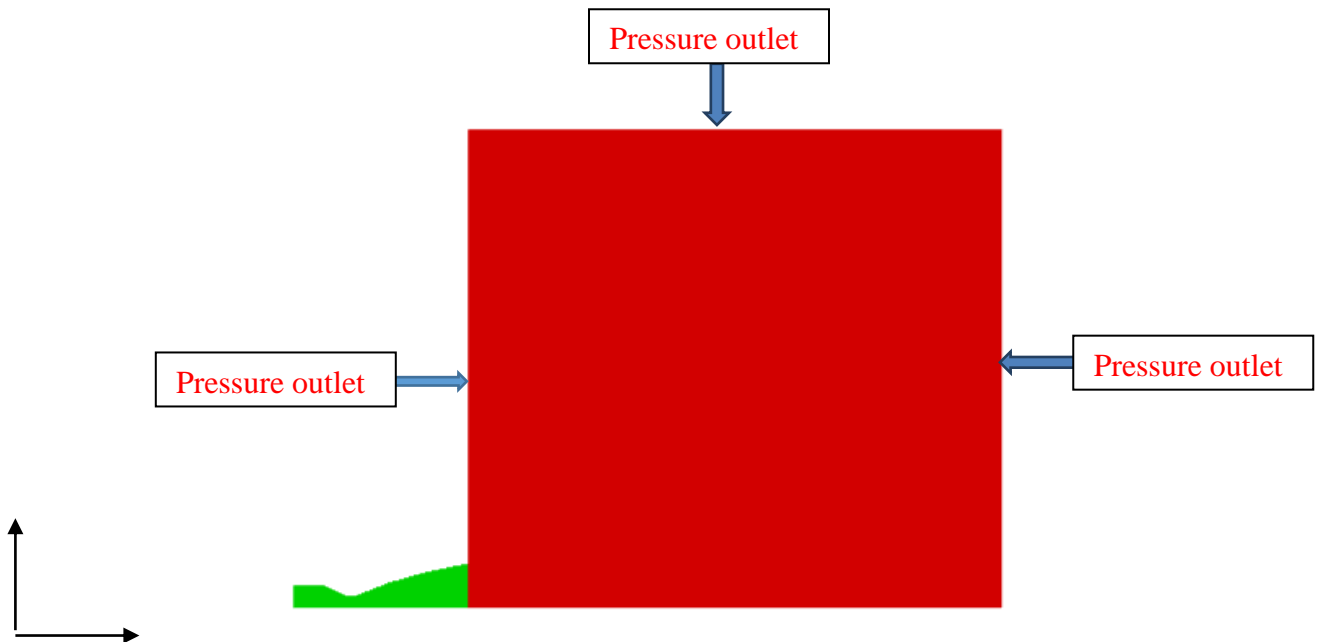


Figure 3.4.b: Computational domain and boundary conditions

CHAPTER III: Results and discussions

The flow at the nozzle inlet is subsonic, and using the values obtained from the 1D thermodynamic calculations, we have $p_a=25.25$ bar, $T_c = 283$ K and $p_{in} = 24.874$ bar as inlet boundary conditions. In the case of the extension (caisson), ambient conditions have been imposed with a constant static pressure p_a . The nozzle wall is taken as a stationary wall with no slip. For the lower boundary, the imposed condition is an axis because the model under consideration is an axisymmetric nozzle. The adopted boundary conditions are provided in the table below.

Table 3.2: Physical boundary conditions

Geometric entity	Physical BCs	Mathematical BCs
Chamber inlet	Imposed static pressure Imposed stagnation temperature	$P_c = 25.25$ bar; $P_{in} = 24.874$ bar $T_c = 283$ K
Chamber and divergent axis	Zero flux on velocity magnitude	$\partial u_x / \partial r = 0$ $\partial u_r / \partial r = 0$
Chamber wall	Zero velocity + adiabatic	$u_x = u_r = 0$ $\partial T / \partial n _{wall} = 0$
Divergent wall	Zero velocity + adiabatic	$u_x = u_r = 0$ $\partial T / \partial n _{wall} = 0$
Caisson boundaries	Imposed static pressure	$\Delta p = p - p_\infty = 0$

3.6.2 Grid generation

Grid generation is the sub-division of the computational domain into a number of smaller, non-overlapping sub-domains: a *grid* (or *mesh*) of *cells* (or *control volumes*). The solution to a flow problem (velocity, pressure, temperature etc.) is defined at *nodes* inside each cell.

Grid generation is of great importance as the accuracy of the computational results depends on it. Over 50% of the time spent on this project was devoted to the definition of the domain geometry and grid generation. The accuracy of a CFD solution is governed by the number of cells in the grid. In general, the larger the number of cells, the better the solution accuracy. Both the

CHAPTER III: Results and discussions

accuracy of a solution and its cost in terms of necessary computer hardware and calculation time are dependent on the fineness of the grid.

For the present numerical problem, after several attempts so as to obtain a good mesh quality, a structured 100x100 mesh generated in GAMBIT 2.4.6 was adopted. For turbulent layer boundary resolutions, the near wall region is refined with a ratio of 1.6.

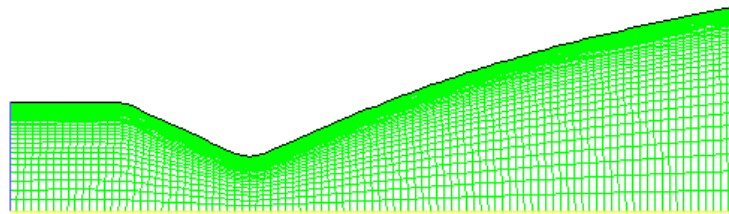


Figure 3.5: 100x100 structured mesh for the nozzle.

For the caisson an unstructured mesh with 13 368 grid elements was used. Refinement in the case of the caisson is done in the vicinity of the nozzle exit where the shocks are located and it is coarsened in the far-field zone as shown in figure 3.6. The total number of grid elements for the computational domain is 23 368.

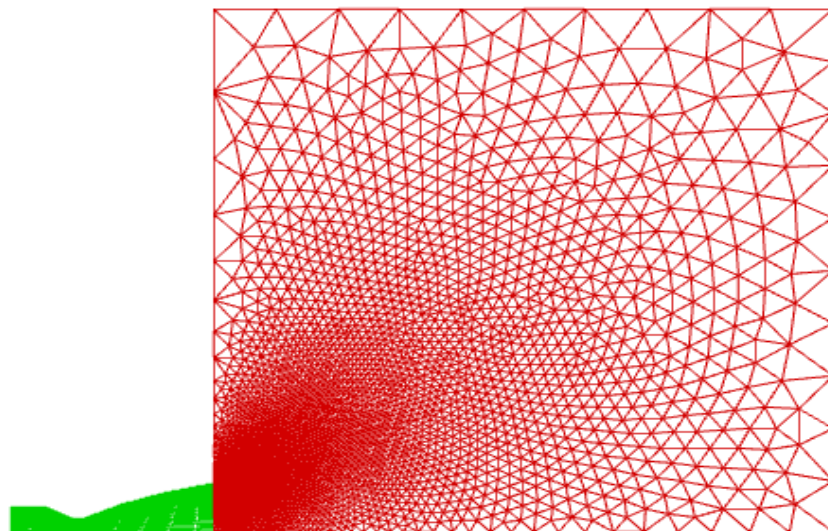


Figure 3.6: Computational domain mesh

CHAPTER III: Results and discussions

In order to recover concisely the boundary layer separation, an improvement of the near-wall region is mandatory (Fig.3.5). The implementation of wall boundary conditions in turbulent flows starts with the evaluation of [60]

$$y^+ = \frac{\Delta y}{\vartheta} \sqrt{\frac{\tau_w}{\rho}} \quad (3.15)$$

where Δy is the distance of the near-wall node to the solid surface, τ_w is the wall shear stress, ϑ is the kinematic viscosity and ρ is the fluid density.

For an accurate resolution of turbulent boundary layer, fine grids with near-wall grid points should verify $y^+ \leq 1$ [59].

The plots have been drawn according to a reduced axial coordinate (X/L_{div}) where the values $X/L_{div}=-0.5$ and $X/L_{div}=+1.0$ correspond to the nozzle inlet and exit respectively.

From the curve in figure 3.7, it can be seen that the global y^+ is less than 1, which simply means that the mesh provides an accurate resolution of the boundary layer thereby nicely detecting the separation of the boundary layer and provide a good location for the separation shock.

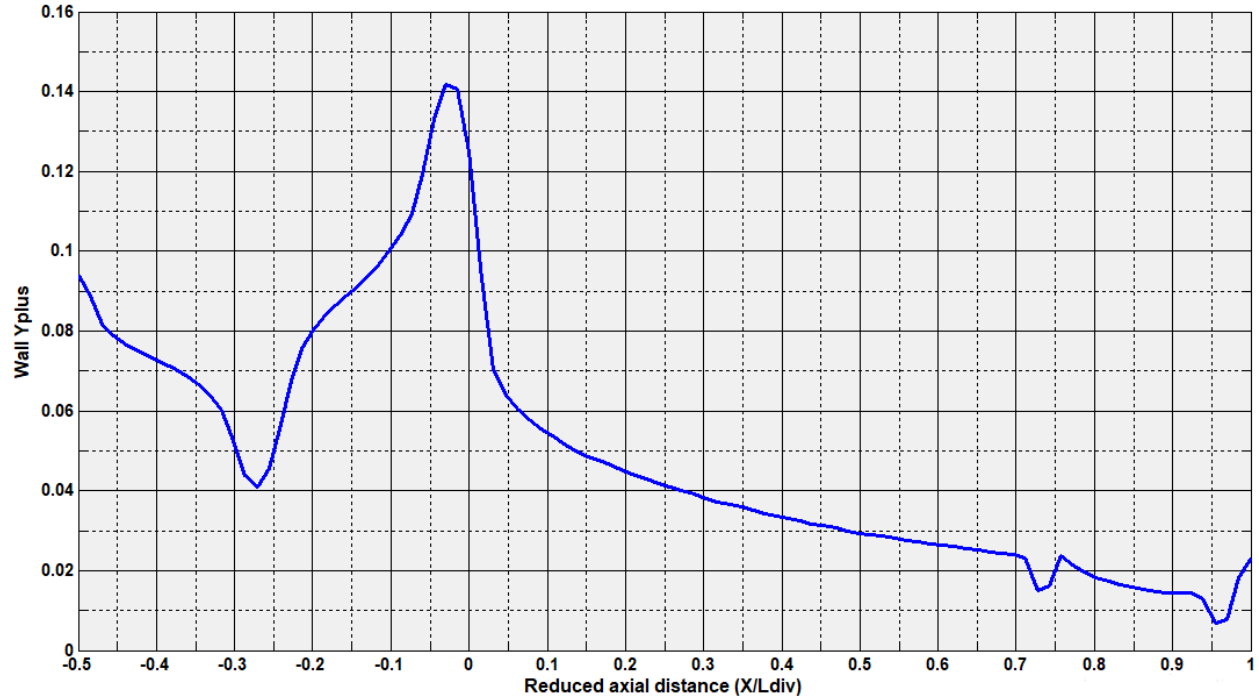


Figure 3.7: Distribution of wall Y+

3.6.3 Computational analysis of the compressible flow

This part presents the results obtained from the CFD simulations ran on the axisymmetric model using Ansys-Fluent® commercial software as the solver. The turbulence is handled by Spalart-Allmaras model, which is a one-equation model for turbulent viscosity μ_t .

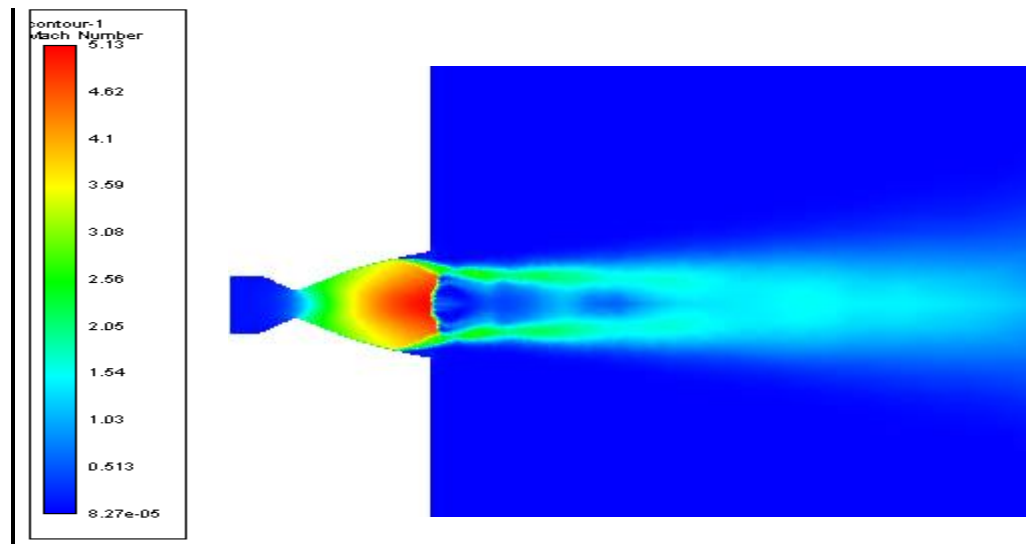


Figure 3.8.a: Distribution of Mach number

CHAPTER III: Results and discussions

As already predicted using basic gas dynamics equations at NPR=25.25, the nozzle runs in overexpansion regime as shown in the figure above. The maximum Mach number attained at the nozzle exit section is 5.13 (Fig.3.8.a). This values reveals a relative deviation of +16.08% compared with the thermodynamics analysis. It is also clearly shown that the Mach disc (oblique to normal shock) is positioned slightly downstream the exit section (Fig.3.8.a), a behavior that seems captured in the figure below (Fig.3.8.b)

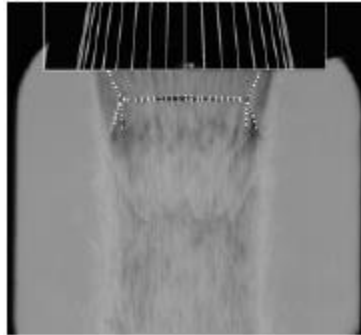


Figure 3.8.b: Sketch of the Mach disc Schlieren image [1]

The curve in the figure below (Fig.3.9) shows that the Mach number increases along the nozzle. Just before the nozzle exit, the nozzle reaches its maximum Mach number of 5.13. Across the disc (oblique to normal shock) in the close downstream ($X/L_{div}=1.016$) of the nozzle exit, the Mach number drops to 2.65 and then the flow eventually becomes subsonic with a Mach number of 0.14. The relative decay of the Mach number across the disc is close to -97% which indicates a huge shock intensity.

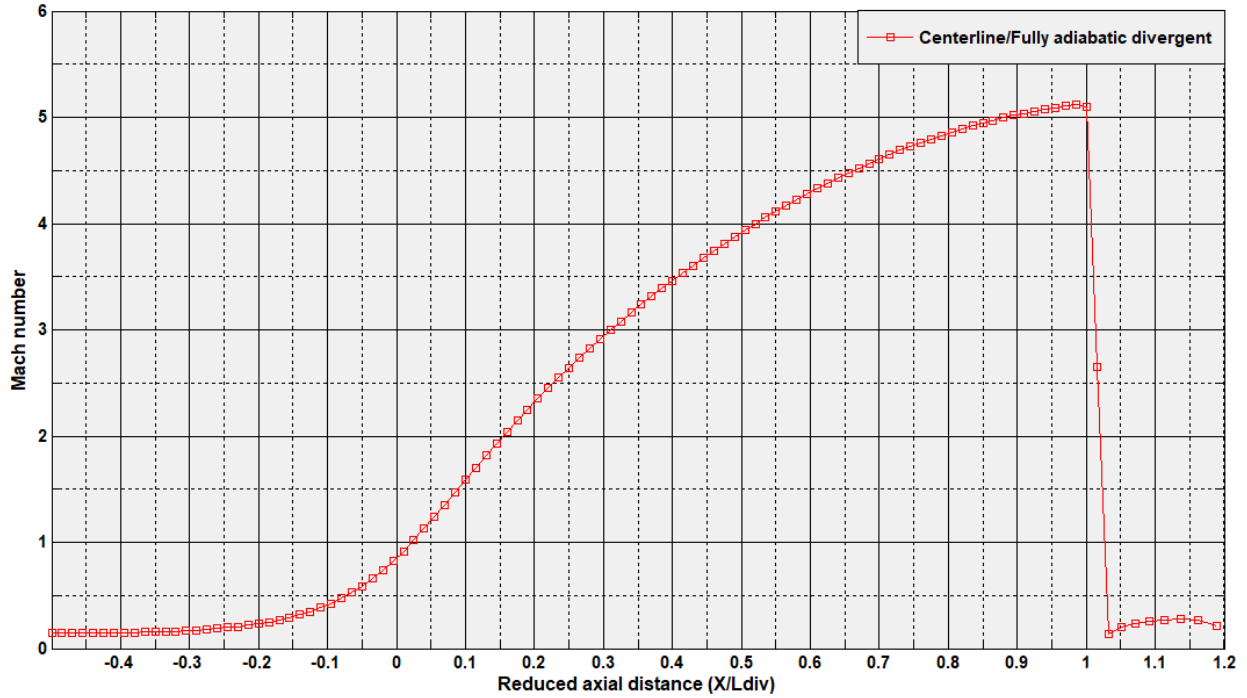


Figure 3.9: Shock and evolution of Mach number

The figure below (Fig.3.10) shows that the Mach number is well resolved by the computations. The given design Mach number for the subscale DIC-TIC nozzle was 5.15 [1]. From the computations, the Mach number just before the nozzle exit is 5.13 with a relative offset of -0.39 % from the experiments' value.

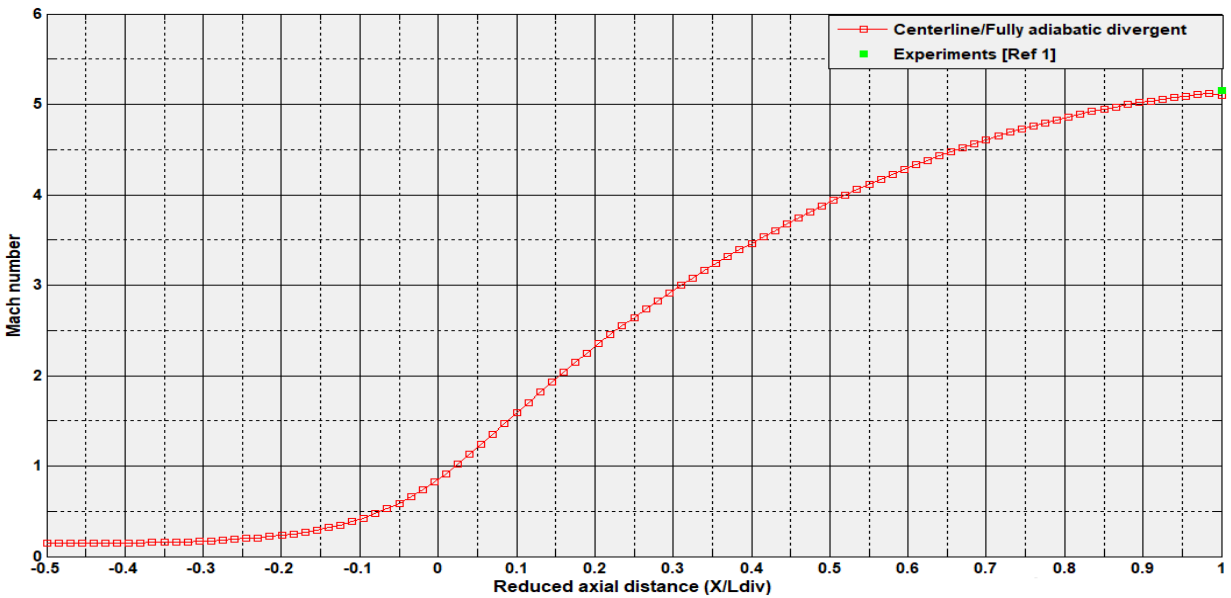


Figure 3.10: Axial Mach number

CHAPTER III: Results and discussions

The curve in figure 3.11 shows continual drop of static pressure along the nozzle. A rapid rise in pressure is observed in the vicinity of the nozzle exit, which is due to a standing shock that is normal to the flow at the exit to match the exit pressure to that of the surrounding. This reveals a recompression normal shock at $X/L_{div}=1.016$.

The figure also shows an inlet ($X/L_{div}=-0.5$) static pressure $P/P_c= 0.9850$ which is quite close to the thermodynamic value $P/P_c= 24.874/25.25=0.9851$.

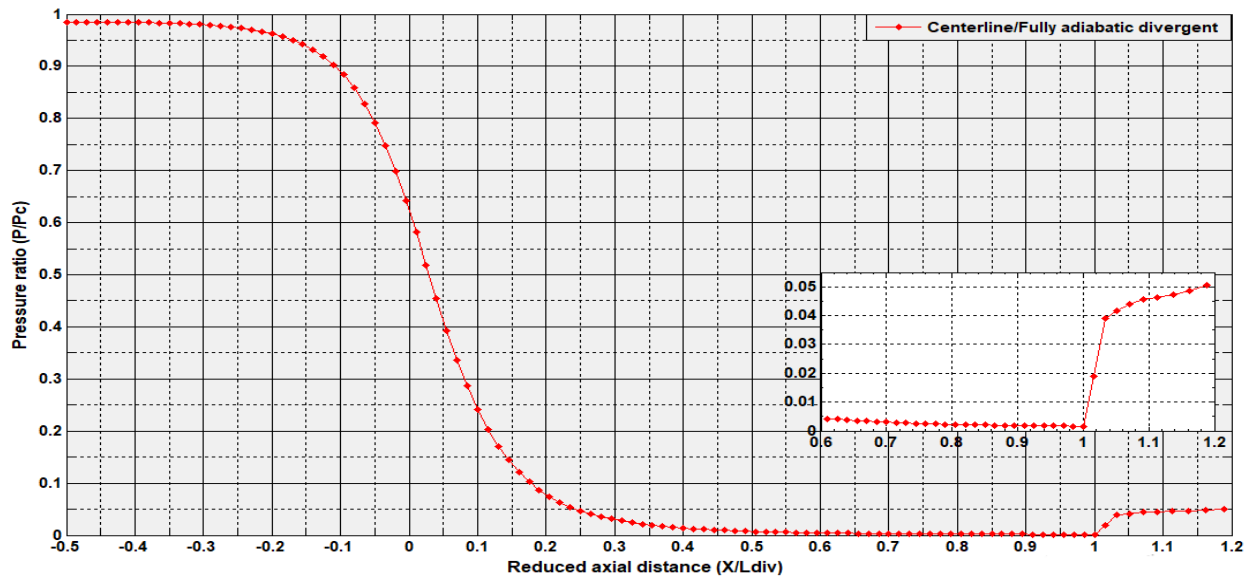


Figure 3.11: Evolution of static pressure on the nozzle centerline

From the figure below (Fig.3.12), it can be seen that there is a difference in the exit pressure between the experimental value and that from the computations. The exit pressure for the experiments is an estimation computed from the given design Mach number using gas dynamics relations. For this reason, an additional curve has been added i.e. thermodynamics, to show that 1D thermodynamics calculations are simplified and do not take into consideration other factors that affect compressible flows, hence, do not give the exact value but are useful for prediction of operating conditions. In this case, an over-prediction of the exit pressure is noted for thermodynamic calculations. That said, looking at the difference (+39.32%), it can be said that given the actual experimental exit pressure, the computations can be easily validated.

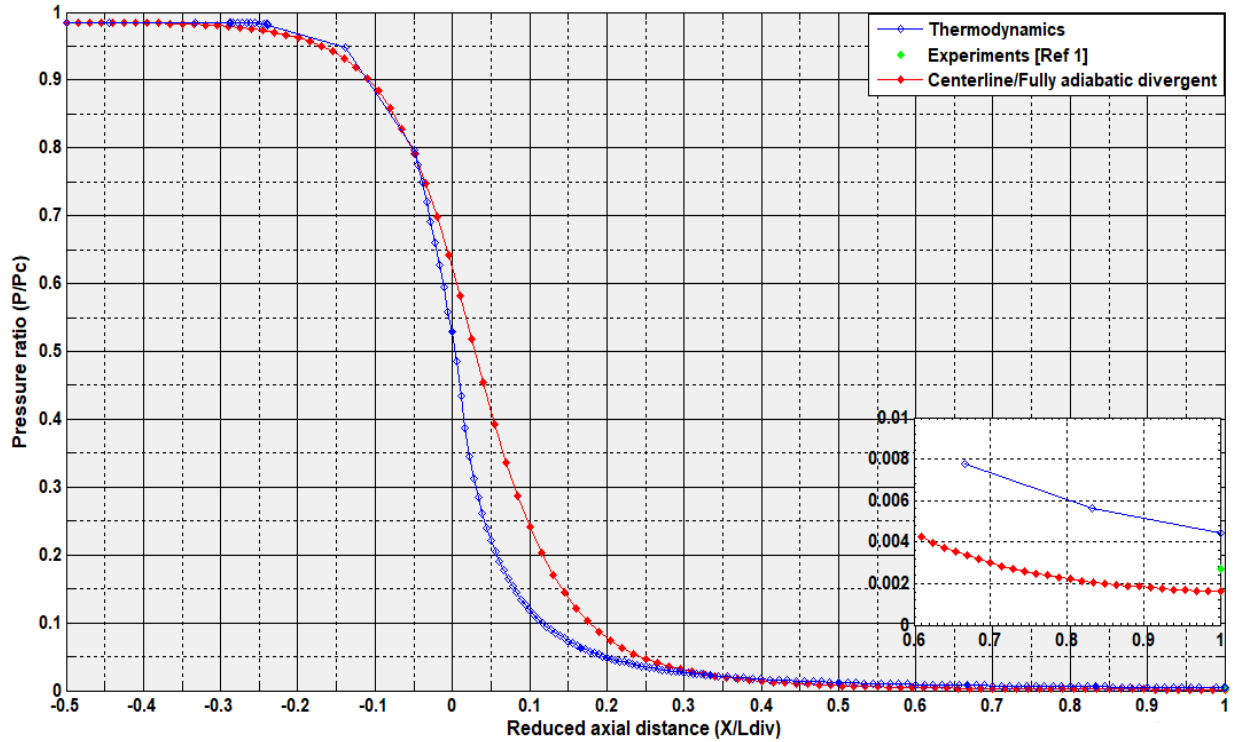


Figure 3.12: Axial static pressure

Since flow separation occurs when the nozzle theoretical wall exit pressure goes down to approximately 80% to 40% of the ambient pressure and this computational work is devoted to flow separation, it is therefore of great importance to validate the model using wall pressures from the experiments [1].

Comparing the numerical results with those from the experiments, it is evident that the wall pressures are well resolved by the computations (Fig.3.13).

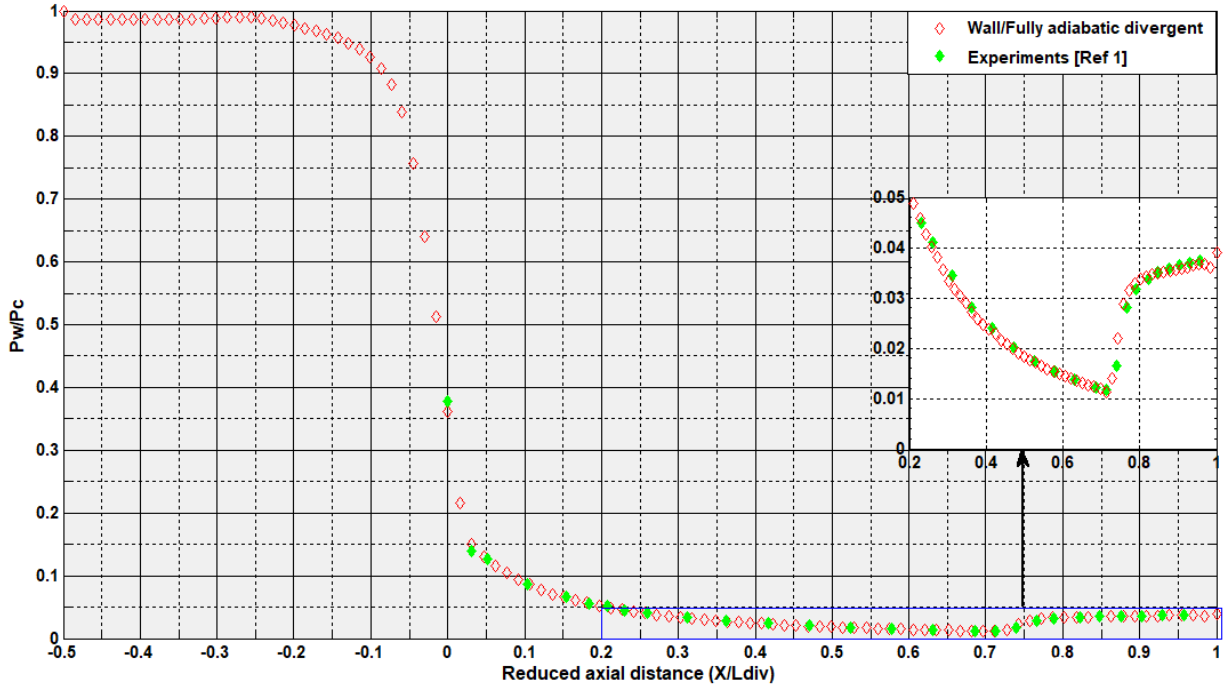


Figure 3.13: Computed and experimental wall pressures

Separation location

To show where in the divergent region the separation is located, iso-surfaces called stations have been created from the centerline to the nozzle wall at six (06) different points, each $X/L_{div}=1.5$ apart. For example, station $6/6=1$ means the radial line at the exit, i.e. the nozzle exit ($X/L_{div}=6/6=1$).

The evolution of the Mach number (Fig.3.14) on stations $2/6$ and $4/6$ appears stable while stations $6/5$ and $6/6$ present fluctuations at the near wall region which is as a result of the shock that is oblique in nature. Upon this, it can be concluded that the separation shock is somewhere between station $4/6$ and $5/6$, which in turn can be termed as station S.

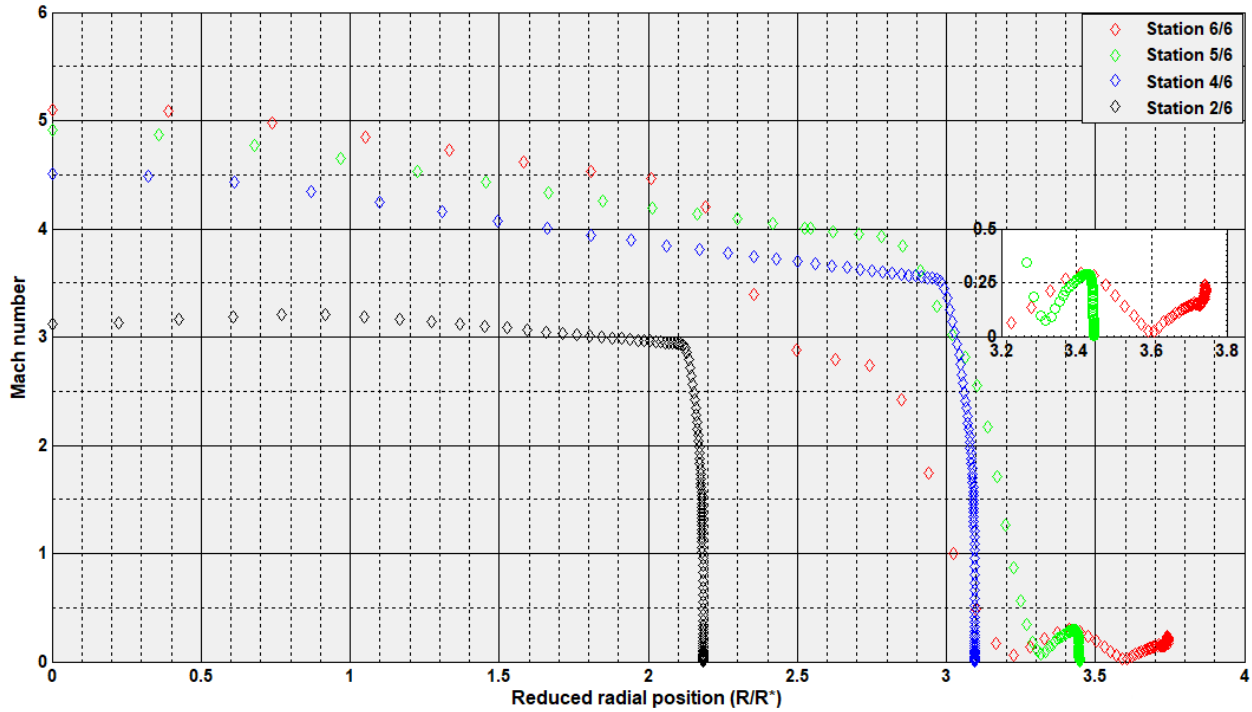


Figure 3.14: Radial evolution of Mach number

The figure 3.15.a shows the contour of axial velocity. The values of the axial velocity in the vicinity of the wall after the separation present negative values. This is an indication of the existence of a reverse flow. The velocity vectors (Fig.3.15.b) show the recirculation region. In the recirculation zone, the velocity vectors are in the opposite direction of the incident flow thus the negative axial velocity values. However, at the end of this zone, the velocity vectors change their direction again towards the incident flow direction (Fig.3.15.b)

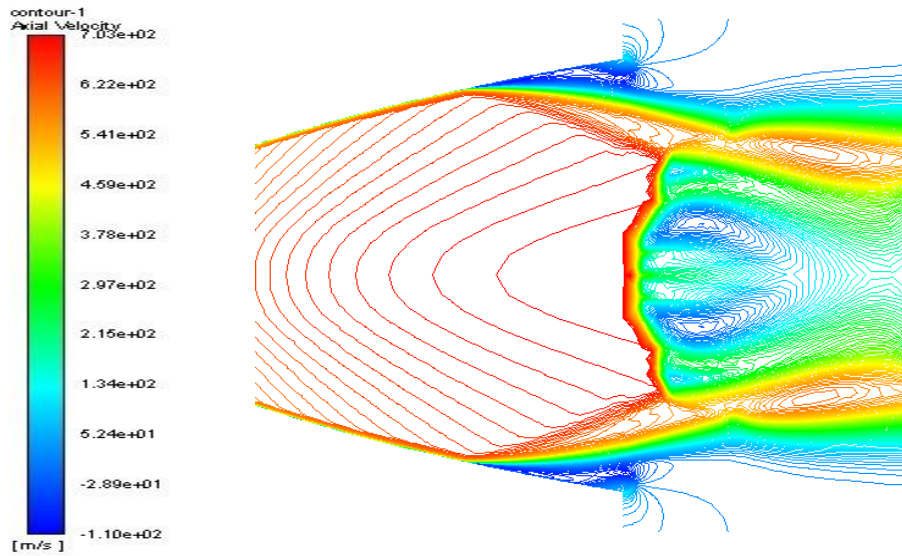


Figure 3.15.a: Axial velocity contours

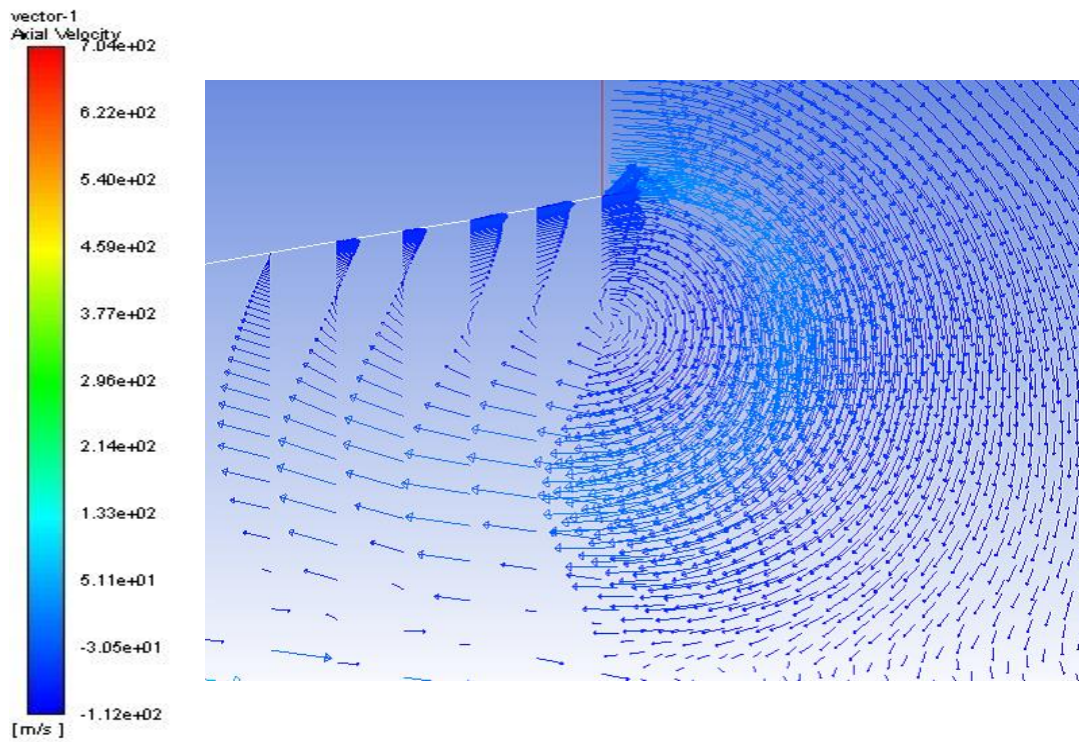


Figure 3.15.b: Recirculation zone

The evolution of shear stress on the wall gives the exact location of the separation shock. At the separation point of two-dimensional boundary layers, the wall shear stress becomes zero.

CHAPTER III: Results and discussions

$$\tau_w = \mu \cdot (\partial u / \partial y)_w = 0$$

The curve in figure 3.16 shows the evolution of the axial wall shear stress. Comparing with the experimental data, it can be seen that the flow separation location has been over-predicted by the computations.

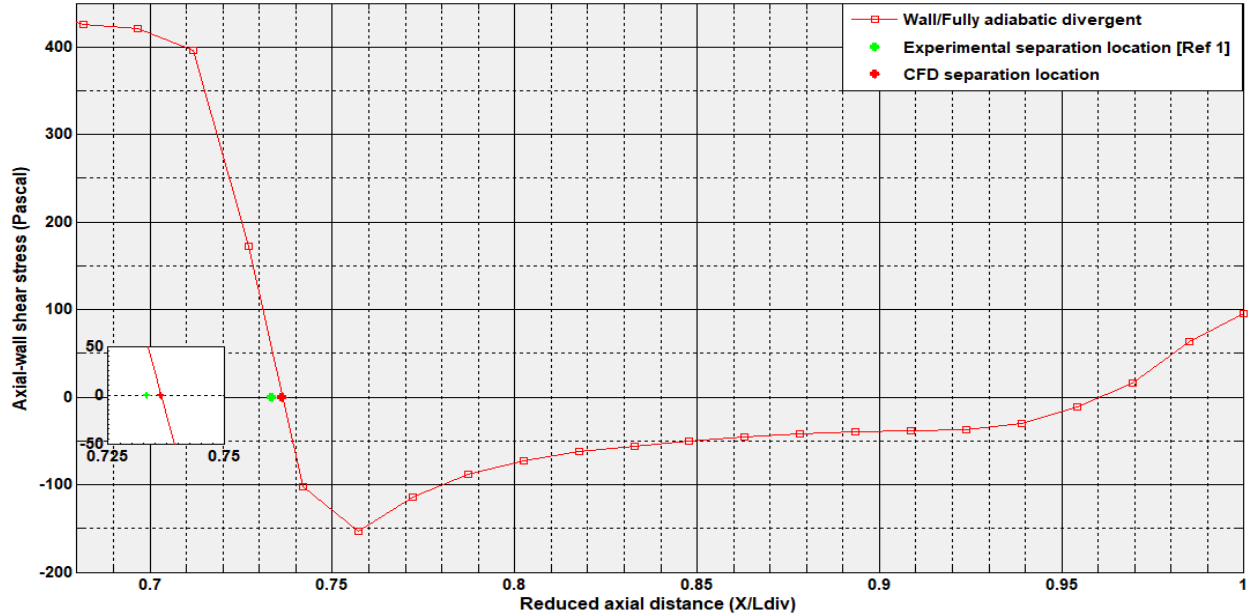


Figure 3.16: Evolution of axial wall shear stress

The computed locations differ from the experimental one over a certain range [1]. According to the experiments, the given separation location is $X_{sep}/L_{div}=0.733333$ and the computed location for the separation is $X_{sep}/L_{div}=0.736356$, giving an offset of 0.41%. The minor difference shows a good agreement with the experimental data. The table below (table 3.3) depicts the numerical values for the evolution of the normal shear stress on the divergent wall.

Table 3.3: Wall pressure and shear stress values

X/L _{div}	0.0000	0.1668	0.3333	0.5000	0.6667	0.736356	0.8333	1.0000
P _w /P _c	0.361175	0.060841	0.0302562	0.018244	0.0126545	0.0188963	0.0345813	0.0389879
Shear stress(Pa)	4016.06	1360.11	840.484	581.476	437.504	0	-55.6683	95.2213

CHAPTER III: Results and discussions

From the values, it is observed that as the wall pressure decreases, the shear stress values also decrease. This drop in wall pressure results in an adverse pressure gradient which tends to reduce the velocity near the wall. This continuous retardation brings the shear stress at $X/L_{div}=0.736356$ on the wall to zero. This point corresponds to a pressure of ratio $P_w/P_c=0.0188963$. From this points, the shear stress becomes negative and then a region of recirculating flow develops (Fig.3.15.b). The shear stress values change back to positive values (Fig.3.16) due to the inflow and upstream acceleration of gas from the ambience into the recirculation region.

Thrust coefficient

The figure below (Fig.3.17) shows the different values for the thrust coefficient which were obtained from the computations and thermodynamic calculations. Represented in blue are estimated values for the thrust coefficient calculated using the ideal thrust coefficient equation (3.14) in the thermodynamic calculations. The CFD computed thrust coefficient (in black) is termed 1D-CFD simply because it is not an averaged value computed over the exit section but from the centerline at the nozzle exit.

Thrust efficiency represented by the thrust coefficient is proportional to the exhaust velocity. A vacuum offers no flow resistance, hence, the maximum flow rate and the highest exhaust velocity through the exhaust nozzle are attained in the vacuum of space. At sea level conditions, the adaptation conditions tend to give the highest thrust efficiency because of the absence of pressure loss due to shocks or separation as compared to overexpansion conditions which require a shock at the nozzle exit to match the exit pressure to the ambient conditions. Comparing the overexpansion condition with the sea adaptation condition, a drop in thrust efficiency of 20.7 % is observed. The estimated value of the experiments' thrust coefficient and that of the computations present an offset of -3.37%.

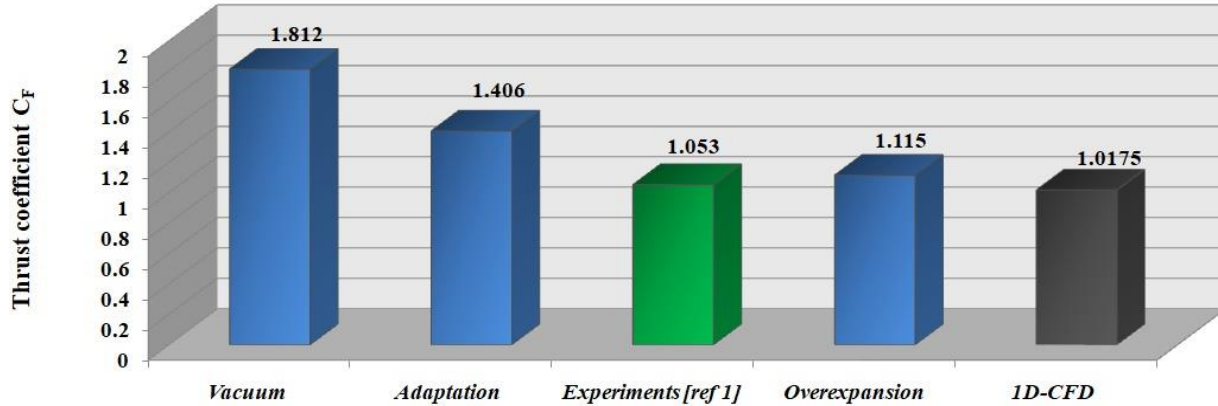


Figure 3.17: 1D thrust coefficients for different conditions

3.7 Parametric Analysis

The given nozzle divergent length 90mm [1] was split into three (3) equal parts of 30mm each starting from the nozzle throat. Div. 1 corresponds to the first part of the divergent section of the nozzle from the throat, Div. 2 the second part and Div. 3 the last part of the nozzle to the exit.

The fully adiabatic wall case will be used as the baseline case to provide a reference datum to check the influence of wall temperature on flow dynamics in overexpanded nozzles. Due to the high temperatures in the nozzle cooling is implemented to reduce wall temperatures to acceptable levels making an adiabatic case not possible to achieve. However, regenerative cooling mimics in essence the adiabatic wall since some of the heat that would have been lost as a heat to the walls is transferred to the fuel and then injected back from the chamber.

Maintaining the same geometric properties of the baseline model, we analyze the influence of wall temperature on the flow, especially its influence on flow separation, recirculation zone size and nozzle performance C_F .

The table 3.4 shows the different wall configurations (modification of wall boundary conditions) of the divergent section of the nozzle wall and cases (imposed wall temperatures T_w) used in this section.

CHAPTER III: Results and discussions

Table 3.4: Wall thermal configurations

Configuration	Case	Div. 1	Div. 2	Div. 3
Baseline	Baseline	Adiabatic	Adiabatic	Adiabatic
Configuration A	Case 1	273 K	273 K	273 K
	Case 2	283 K	283 K	283 K
	Case 3	298 K	298 K	298 K
Configuration B	Case 1	Adiabatic	Adiabatic	273 K
	Case 2	Adiabatic	Adiabatic	283 K
	Case 3	Adiabatic	Adiabatic	298 K
Configuration C	Case 1	273 K	Adiabatic	Adiabatic
	Case 2	283 K	Adiabatic	Adiabatic
	Case 3	298 K	Adiabatic	Adiabatic

Configuration A

In this first scenario, a comparative analysis where a fully isothermal divergent wall with different imposed wall temperatures T_w is discussed (table 3.5). The objective is to check the effect of wall temperature T_w on flow separation and the thrust efficiency.

Table 3.5: Wall thermal configuration A

Configuration	Case	Div. 1	Div. 2	Div. 3
Configuration A	Case 1	273 K	273 K	273 K
	Case 2	283 K	283 K	283 K
	Case 3	298 K	298 K	298 K

The curve in figure 3.18 shows that the distribution of the Mach number computed across the centerline is not affected by thermal conditions on the divergent wall.

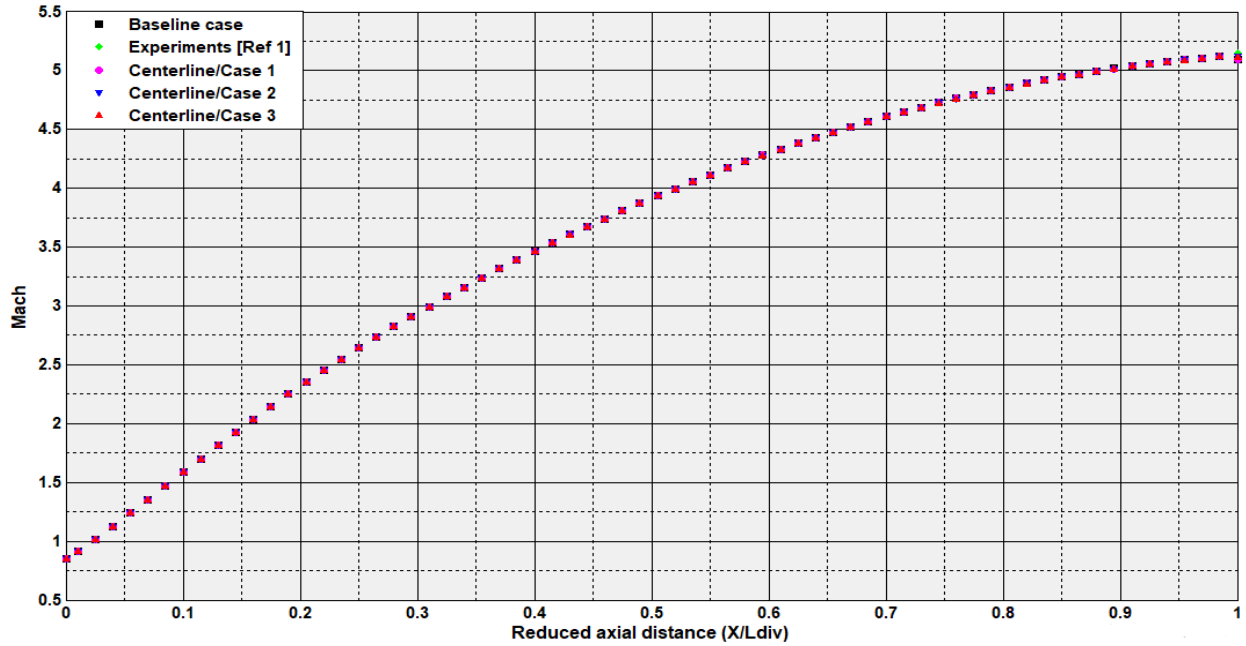


Figure 3.18: Axial Mach number (Config.A)

However, axial Mach number values computed from the near wall region is affected by thermal conditions at the divergent wall. As temperature increases, the near wall region experiences a decrease in axial Mach number (Fig.3.19).

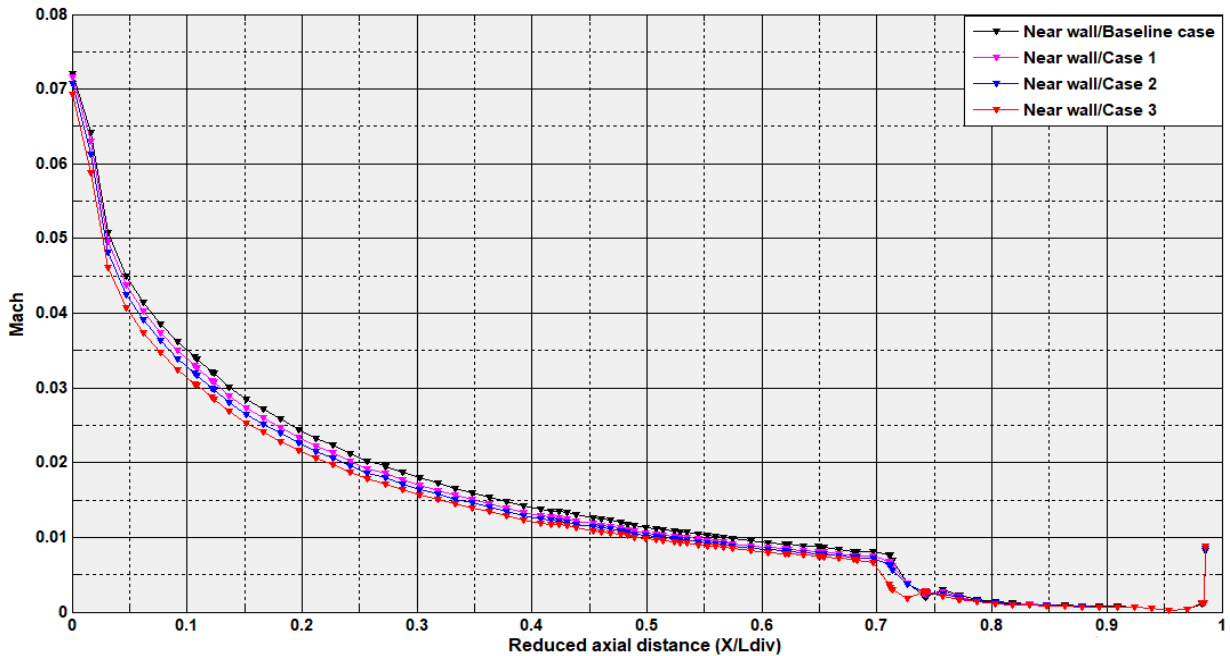


Figure 3.19: Mach number computed from the near wall (Config.A)

CHAPTER III: Results and discussions

The evolution of the wall pressure in figure 3.20 from the throat to $X/L_{div}=0.7$ appears not to be affected by thermal conditions at the divergent wall. However, a rapid rise in wall pressure at different locations is easily observed for each case. This indicates different points for the origin of interaction which results in different locations of separation.

The computed wall pressure results also show that Case 3 which has the highest wall temperature is the first to present a rise in wall pressure (Fig.3.20). As the temperature decreases, the origin of the interaction shifts further in the downstream direction.

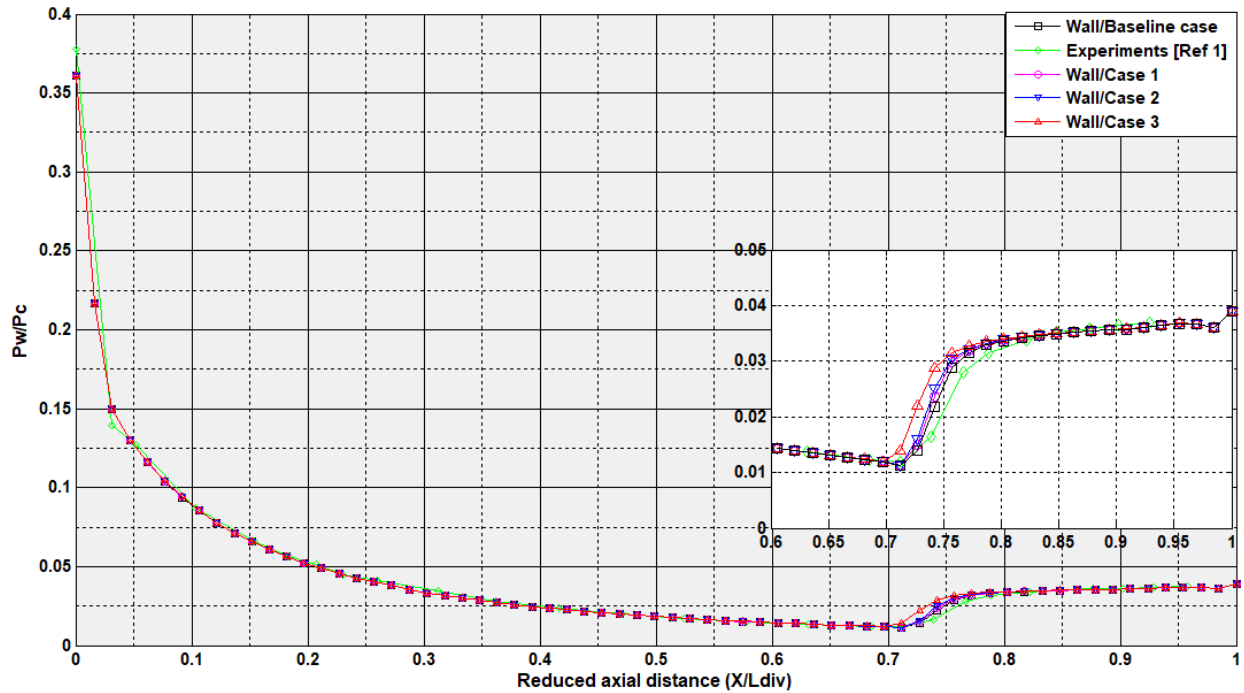


Figure 3.20: Wall pressures (Config.A)

For the imposed wall temperatures, it can be observed from figure 3.21 that the flow separation shifts in the upstream direction of the nozzle with an increase in temperature.

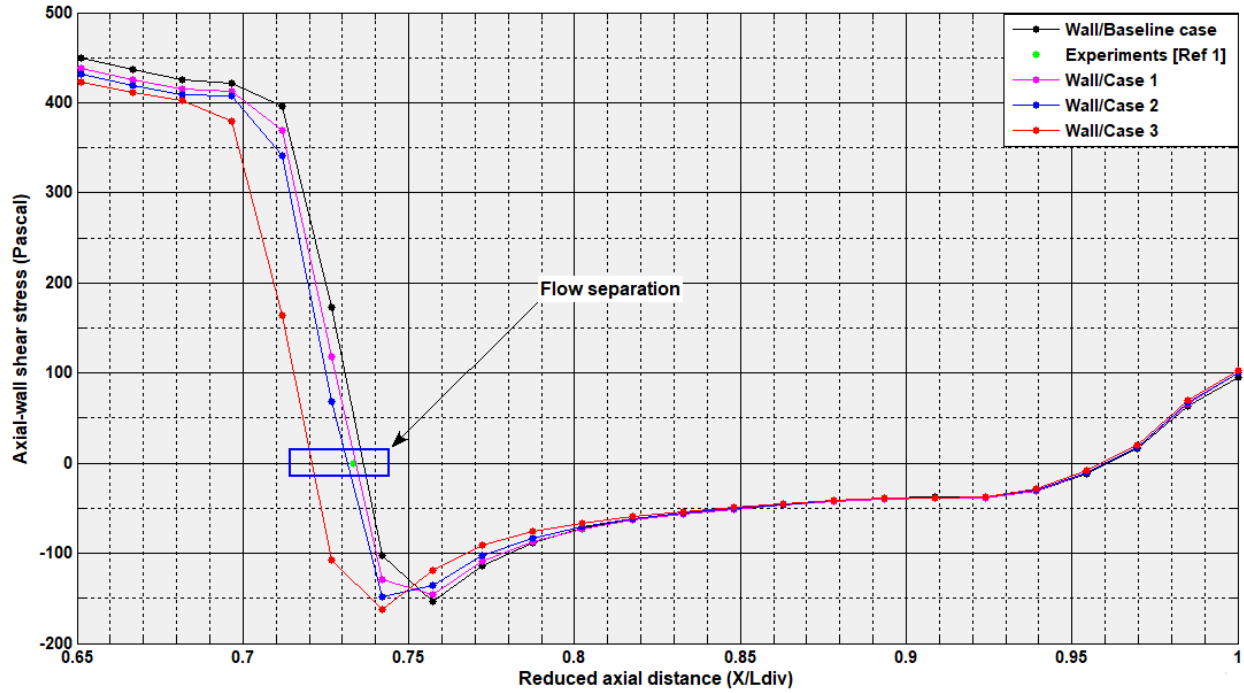


Figure 3.21: Evolution of axial wall shear stress (Config.A)

Table 3.6: Separation location

Case	Separation location(X/Ldiv)	Offset (%)
Baseline	0.73636	Reference
Case 1	0.73409	-0.31
Case 2	0.73166	-0.64
Case 3	0.72093	-2.09

Table 3.6 shows the exact computed separation locations for the cases. Compared to baseline case, Case 1 gives an offset of -0.31% and an offset of -2.09% for Case 3. This shows that as the temperature increases, the separation point moves in the upstream direction from the initial position.

For configuration A, The separation location for the isothermal divergent wall condition are all upstream the initial location i.e. baseline case separation location. This is shown in figure 3.21 and from the negative offset values in table 3.6.

CHAPTER III: Results and discussions

The recirculation zone computed in terms of axial size is also observed to differ with respect to the imposed wall temperature on the divergent wall.

For the recirculation zone size, the results in the histograms indicate an increase in size of the recirculation zone as the wall temperature increases (Fig.3.22). A relative increase of +4.87% is observed for Case 3 while Case 1 presents +1.33% when compared to the baseline.

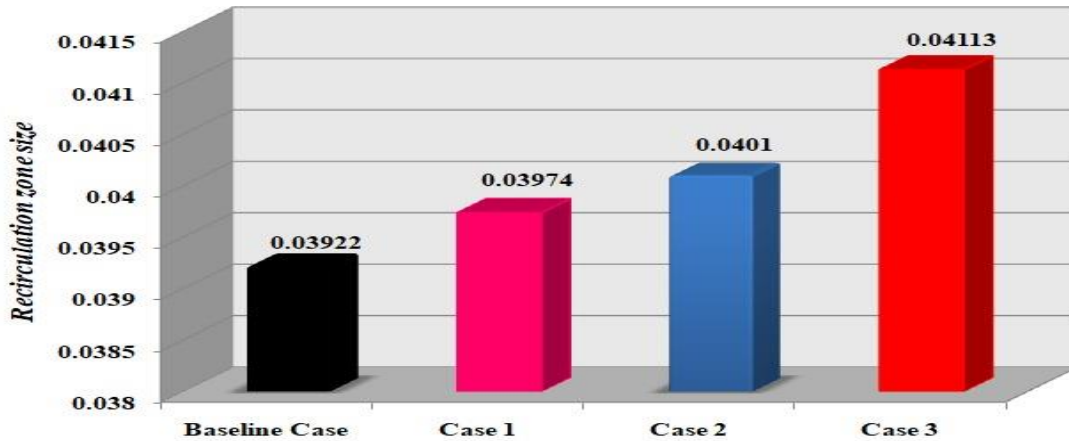


Figure 3.22: Recirculation zone size (Config. A)

The computation of the thrust coefficients shows that the shift of the separation location further upstream results in loss of performance. Case 3 which has the furthest location upstream the nozzle shows the least thrust efficiency with a 1.73% drop in thrust force compared to the baseline. Case 1 shows a better advantage compared to the other two (02) thermal cases as it presents a higher thrust efficiency (Fig.3.23). A relative difference of +1.35% is observed when compared with Case 3.

The thrust coefficients for the isothermal divergent wall conditions are all less than the baseline case .i.e. the fully adiabatic divergent wall, this correlates with the findings in the separation location where all the cases are upstream of the baseline case location.

As the separation moves further in the upstream direction, loss in thrust efficiency is observed.

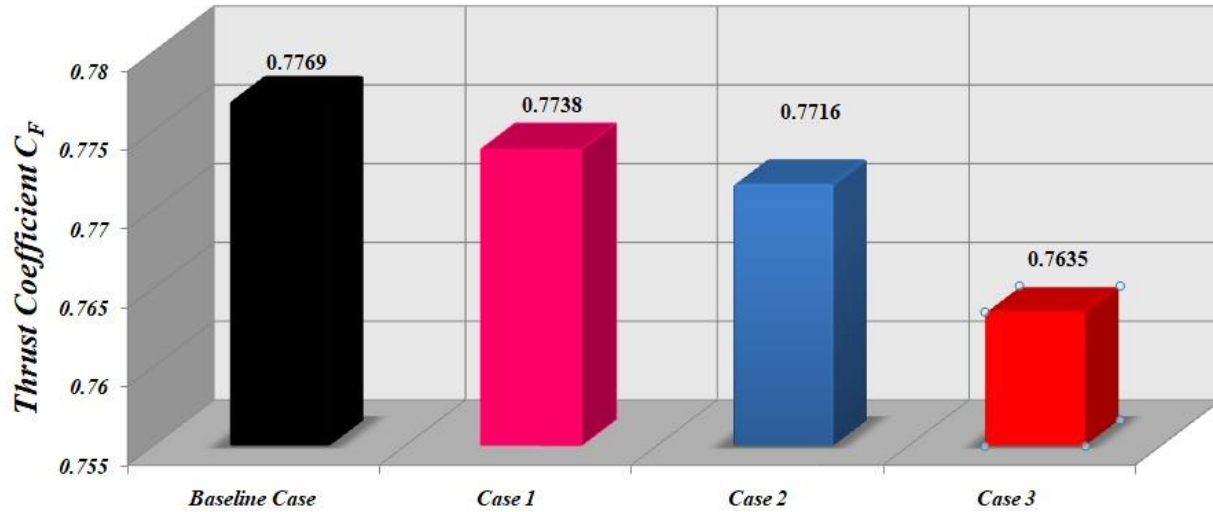


Figure 3.23: Thrust coefficient (Config.A)

Configuration B

After observing the effect of wall temperature on flow separation, recirculation zone size and thrust efficiency, the next 2 configurations .i.e. Configurations B and C are studied to check the best cooling position of the divergent wall that could lead to improved thrust efficiency when cooled.

In configuration B, maintaining the same wall temperatures, the last portion of the divergent section of the nozzle wall is treated as isothermal with a fixed wall temperature T_w while the rest of the nozzle wall is taken as adiabatic (table 3.7)

Table 3.7: Wall thermal configuration B

Configuration	Case	Div. 1	Div. 2	Div. 3
Configuration B	Case 1	Adiabatic	Adiabatic	273 K
	Case 2	Adiabatic	Adiabatic	283 K
	Case 3	Adiabatic	Adiabatic	298 K

Figure 3.24 shows that for configuration B, the distribution of the Mach number computed across the centerline is not affected by the imposed thermal conditions as in configuration A.

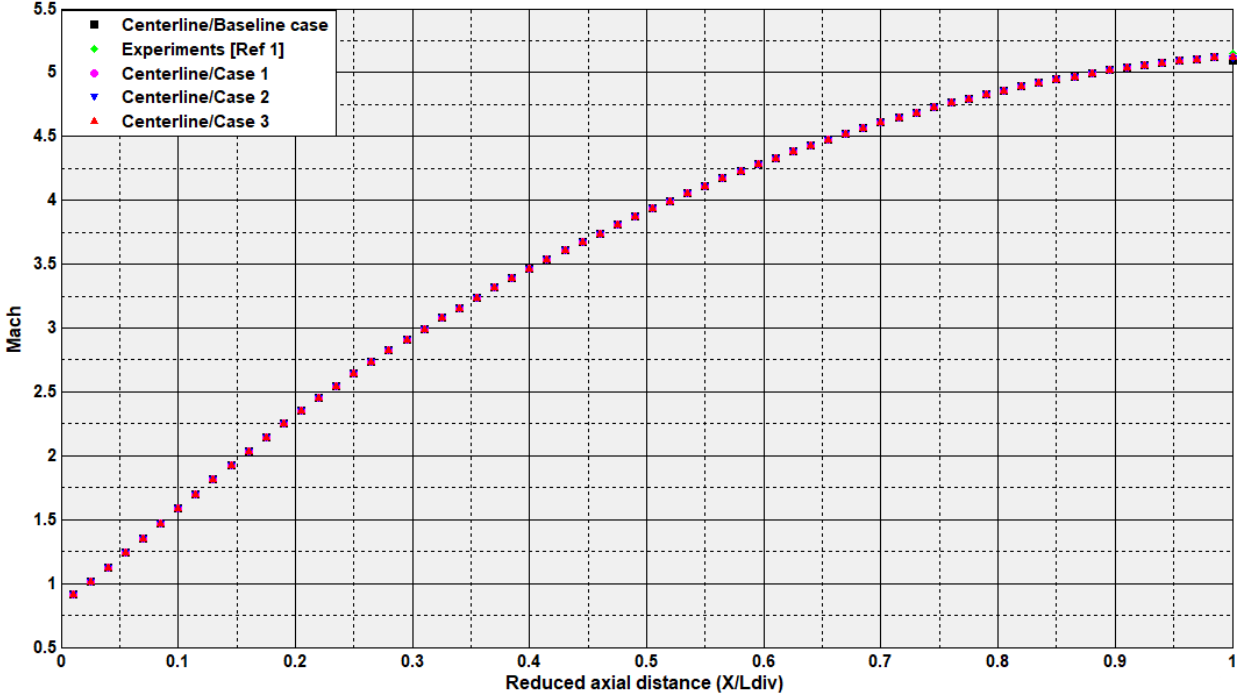


Figure 3.24: Axial Mach number (Config.B)

In Figure 3.25 the distribution of wall pressure shows that the point associated with a rise in wall pressure is the same for all thermal cases. The effect of the adverse pressure gradient is felt at the around same point in the nozzle divergent. This is due to the small difference in wall temperature.

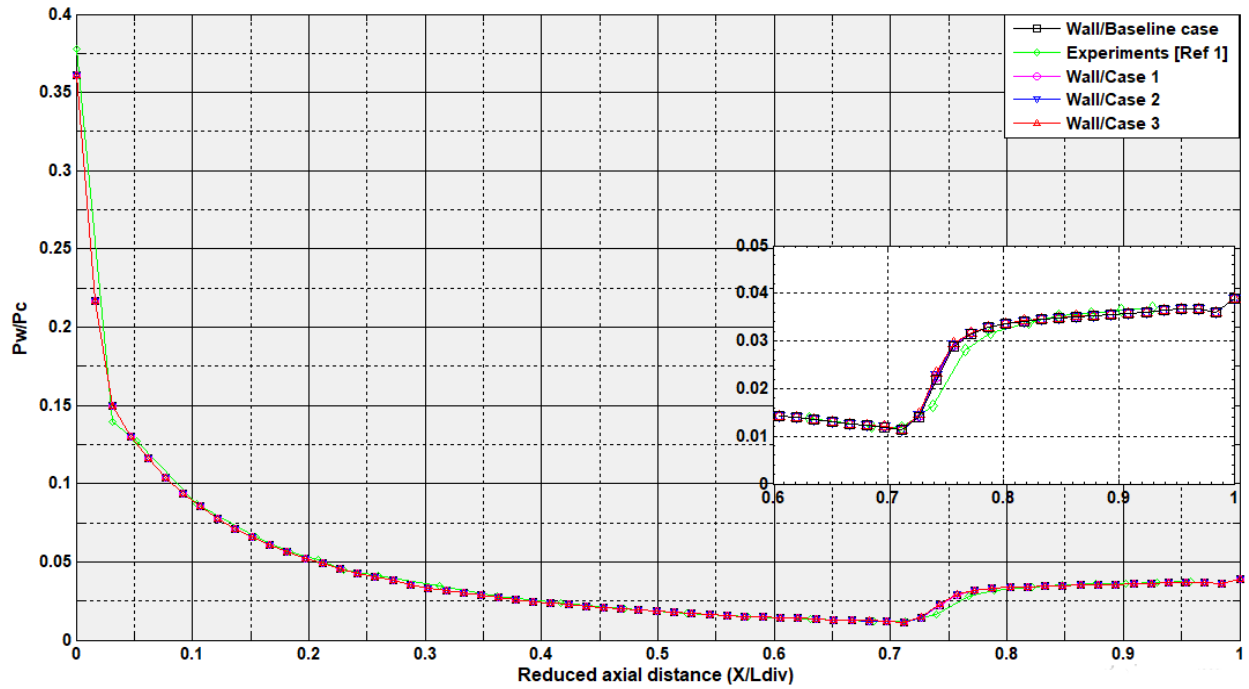


Figure 3.25: Wall pressures (Config.B)

In this configuration (Config.B), the evolution of the shear stress indicates that all the locations are upstream of the baseline case location and downstream of the experimental location (Fig.3.26).

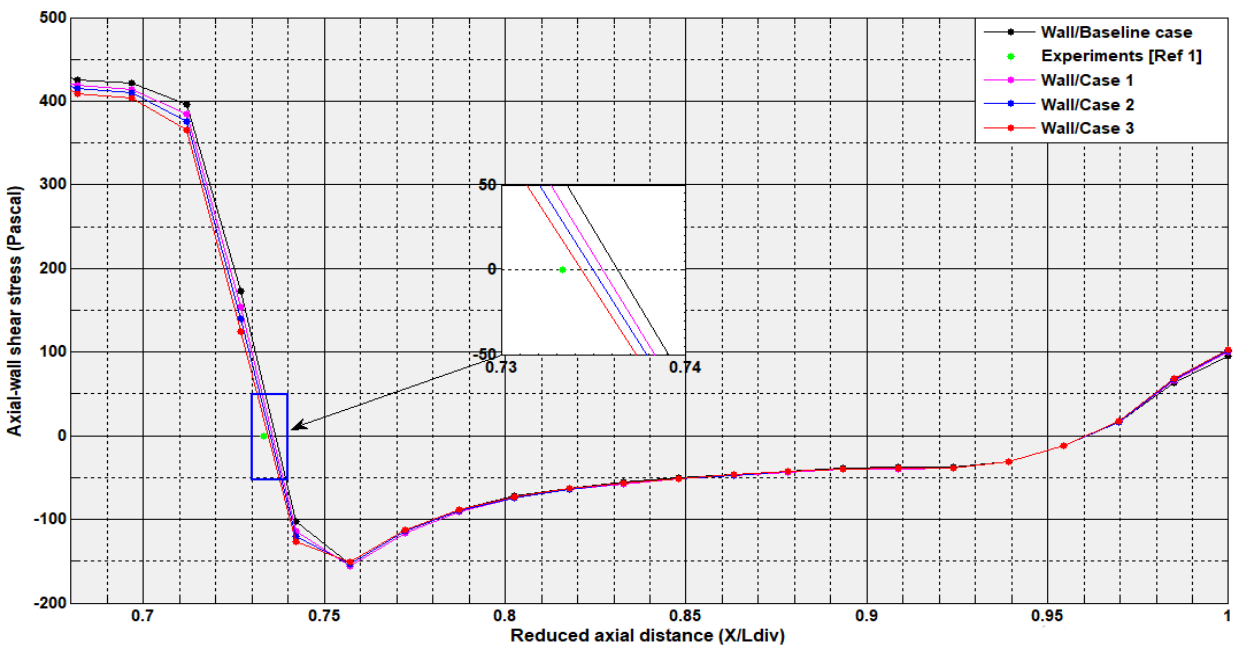


Figure 3.26: Evolution of axial wall shear stress (Config.B)

CHAPTER III: Results and discussions

Table 3.8: Separation location

Case	Separation location (X/Ldiv)	Offset (%)
Baseline	0.73636	Reference
Case 1	0.73553	-0.11
Case 2	0.73501	-0.18
Case 3	0.73439	-0.27

From the offsets shown in table 3.8, the values indicate how close the separation locations are to the baseline case, the case with the lowest temperature being the closest.

Thrust coefficient decrease with an increase in temperature as shown from the histogram (Fig.3.27). All thermal cases present a thrust coefficient less than the baseline case (Fig.3.27). A relative difference of -0.1% between Case 1 and the baseline case is observed while Case 3 gives a difference of -0.27%. This difference is as a result of the closeness of the separation point to the baseline case shown by the offset (table 3.8).

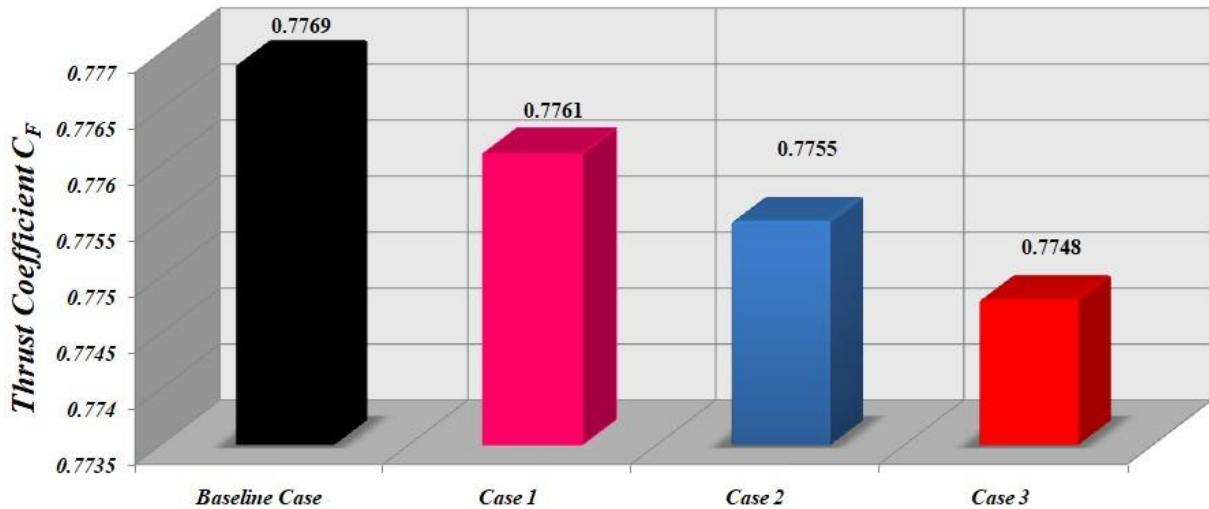


Figure 3.27: Thrust coefficient (Config.B)

CHAPTER III: Results and discussions

Configuration C

In this configuration, the first portion of the divergent section of the nozzle wall starting from the throat is treated as isothermal with a fixed wall temperature T_w while the rest of the nozzle wall is taken as adiabatic (table 3.9).

Table 3.9: Wall thermal configuration C

Configuration	Case	Div. 1	Div. 2	Div. 3
Configuration C	Case 1	273 K	Adiabatic	Adiabatic
	Case 2	283 K	Adiabatic	Adiabatic
	Case 3	298 K	Adiabatic	Adiabatic

As in the other 2 configurations, the distribution of the Mach number computed across the centerline for all thermal conditions does not change with respect to the imposed wall temperature (Fig.3.28).

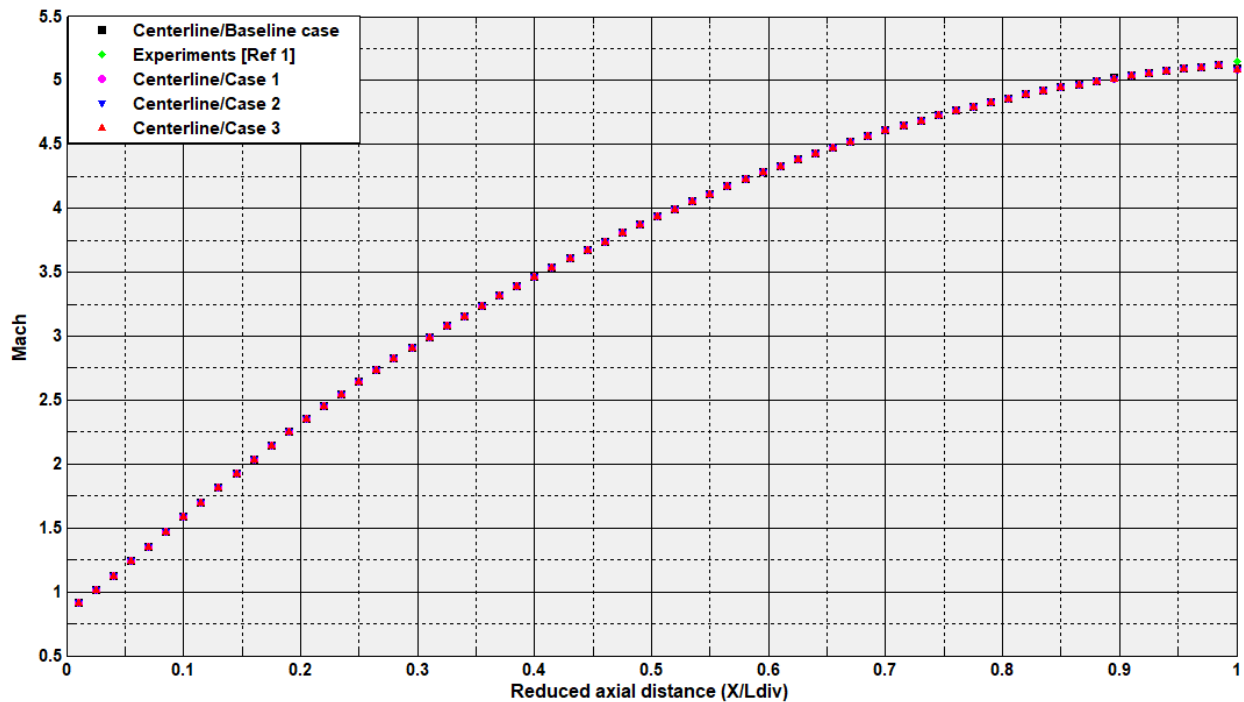


Figure 3.28: Axial Mach number (Config.C)

CHAPTER III: Results and discussions

The origin of the interaction in the boundary layer for all thermal cases is the same as the baseline case excepting that of the experiments which is first along the axis (Fig.3.29). This implies that effect of the adverse pressure gradient is ‘felt’ around the same point in the nozzle divergent wall.

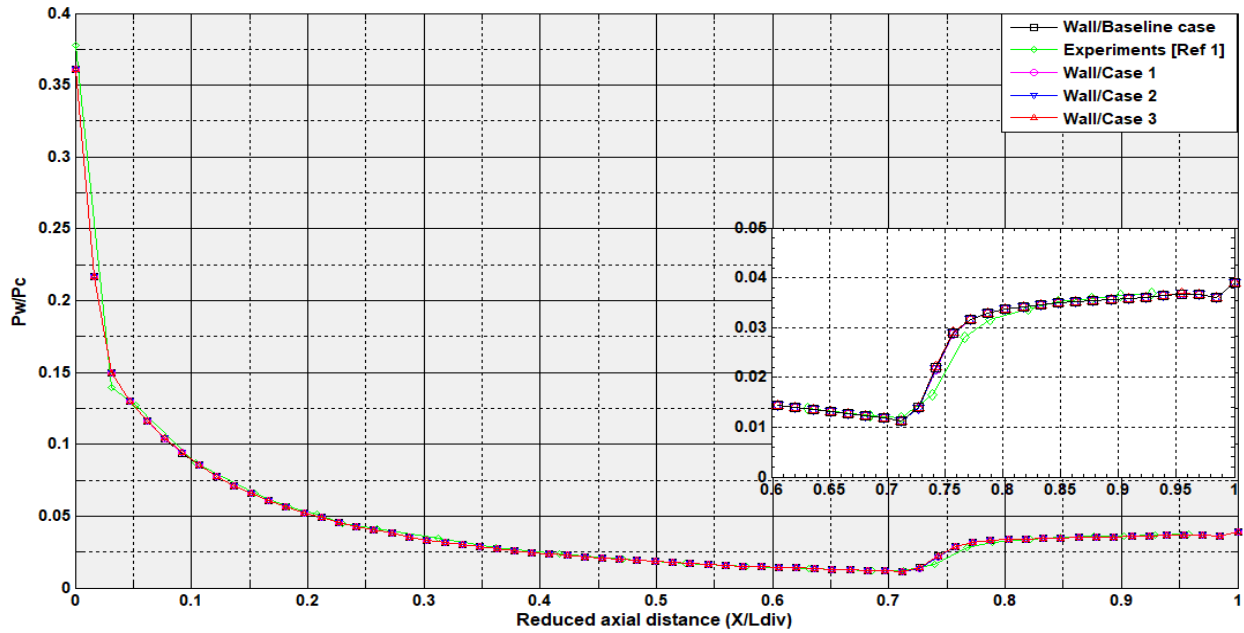


Figure 3.29: Wall pressures (Config.C)

From figures 3.30 and 3.31, Cases 1 and 2 present separation locations downstream of the baseline yet not sparse which is due to the closeness of the origin of interaction. Unlike Case 1 and 2, the separation location for Case 3 is situated upstream owing to the high wall temperature which reduces the resistance of the flow to boundary layer separation.

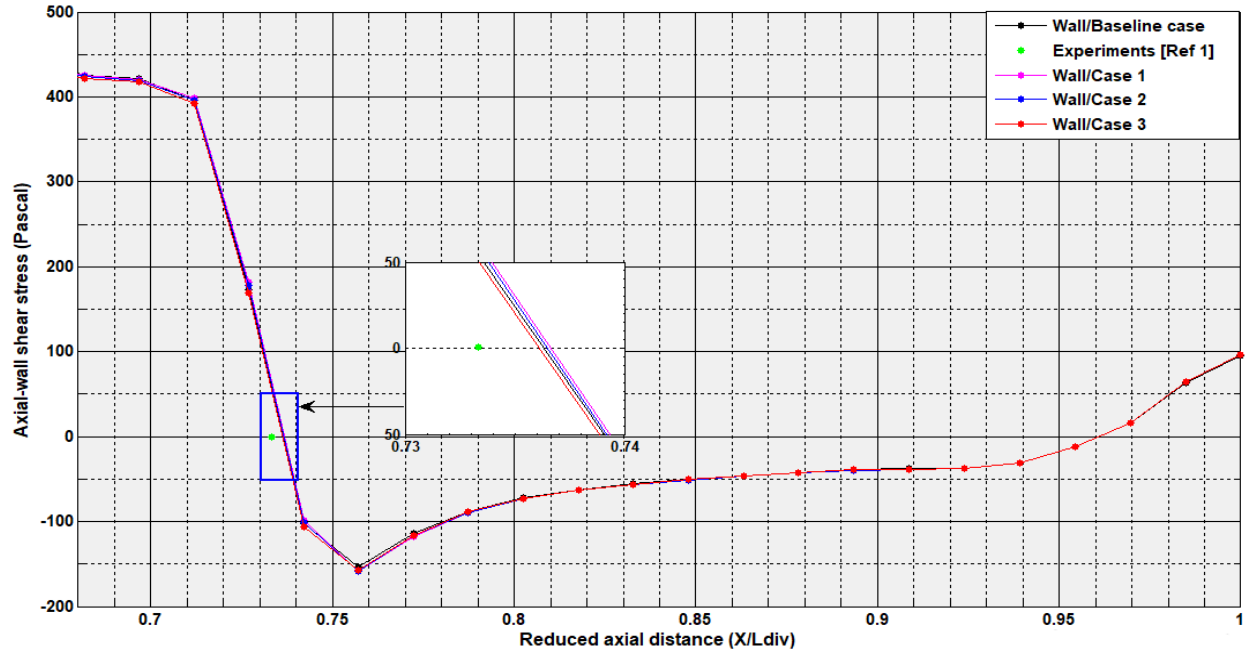


Figure 3.30: Evolution of axial wall shear stress (Config.C)

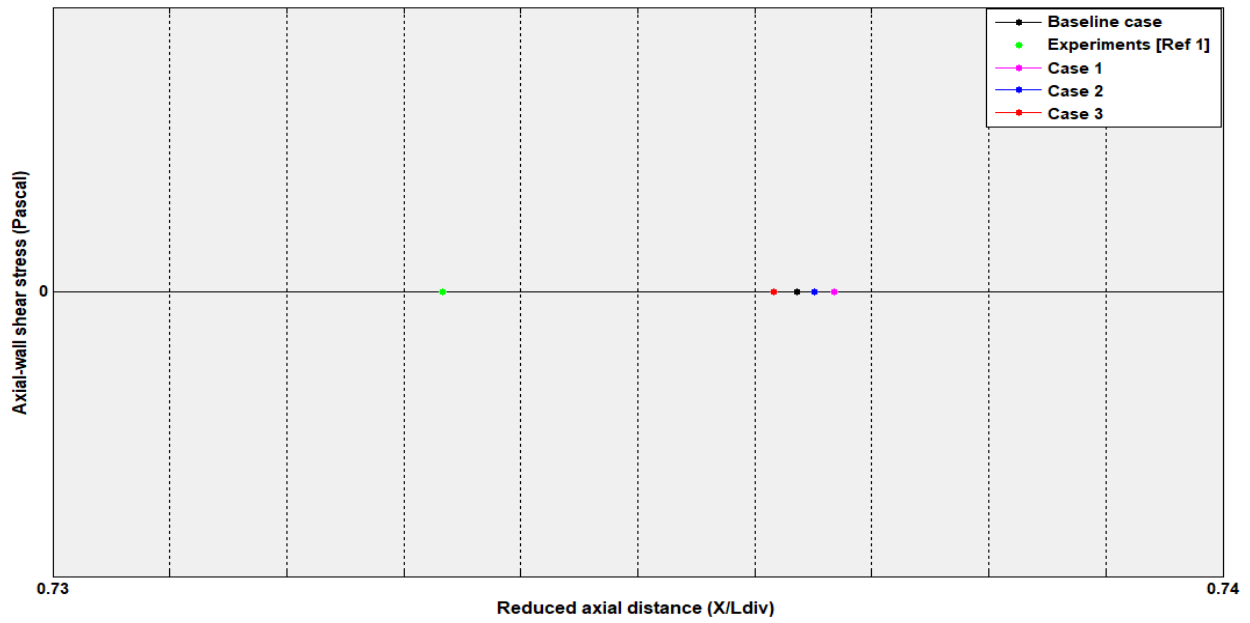


Figure 3.31: Separation location (Config.C)

CHAPTER III: Results and discussions

Table 3.10: Separation location

Case	Separation location (X/Ldiv)	Offset (%)
Baseline	0.73636	Reference
Case 1	0.736682	0.0443
Case 2	0.736512	0.0212
Case 3	0.736157	-0.0270

Despite the closeness of the location observed in figure 3.30, table 3.10 shows the relative difference in distance. Case 1 and Case 2 present positive offset values implying a downstream shift of the separation from the initial point.

The shift of the separation location in the downstream direction resulted in a decrease in size of the recirculation zone for Cases 1 and 2. A relative decrease in size of 0.15% is observed for Case 1 while the size of the recirculation zone for Case 3 increases by 0.31% (Fig.3.32).

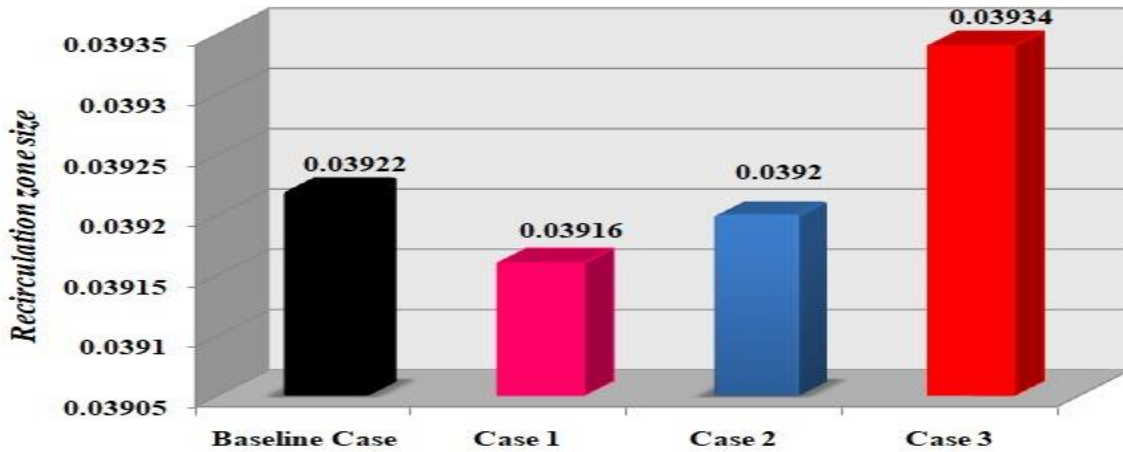


Figure 3.32: Recirculation zone size (Config.C)

Case 1 which presented a location furthest downstream of the nozzle (table 3.10) has the highest thrust coefficient for this configuration (Fig.3.33) with a relative increase in thrust efficiency of 0.039%. The computations also show a relative difference in thrust of -0.10% for Case 3 when compared with Case 1 and a 0.064% loss in thrust compared to the baseline case.

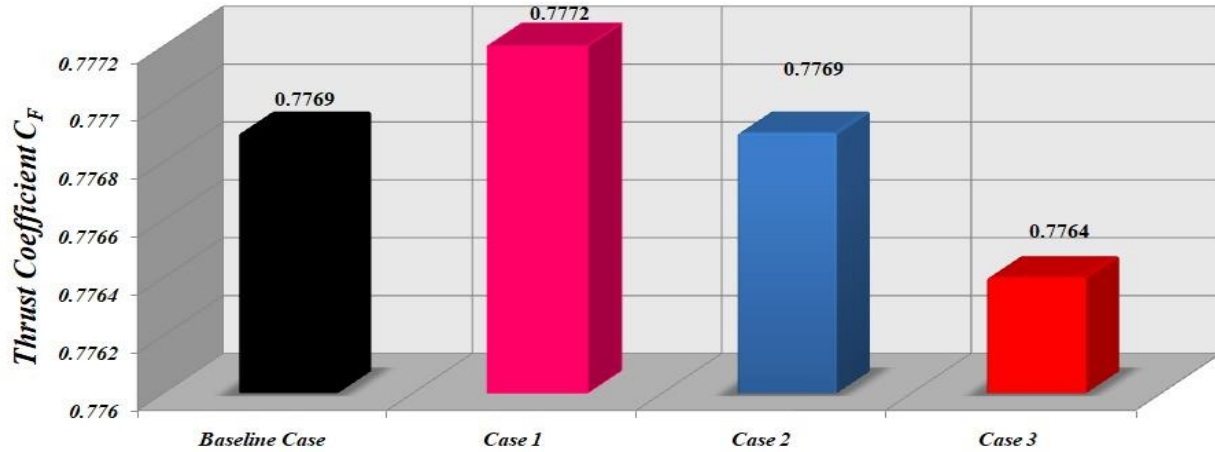


Figure 3.33: Thrust coefficient (Config.C)

Conclusion

The 1D thermodynamic calculations showed that at given conditions, the nozzle runs in overexpansion regime. An offset of -16.41% was found for the exit Mach number calculated from thermodynamic relations when compared to the exit design Mach number from the experiments. Also, the 1D thermodynamic calculations tend to overpredict the exit pressure ratio as compared to the experiments and the 1D CFD results.

The numerical results were obtained for a fully adiabatic case. Model validation was done by comparing the computed wall pressure and the separation location with the experimental data. The computed results presented an offset of +0.41% and the wall pressures showed a good agreement with the experimental wall pressures. In addition, the recirculation zone and the Mach disc pattern was in accordance with the observations by Meister [65] and Al.

In the parametric analysis, it has been shown that the wall temperature that the wall temperature has an effect on the separation location and consequently the thrust coefficient C_F . As the wall temperature increases, the separation location moves from the initial position in the upstream direction resulting in a loss of thrust.

Comparing the results for the considered configurations, Configuration C has shown to give the furthest separation location downstream in the nozzle's divergent region. As a result, Configuration C presented the highest thrust efficiency.

Conclusion and perspectives

Flow separation continues to be an engineering problem of fundamental importance in numerous industrial applications. In this study, the phenomenon of flow separation and its associated undesirable effect on thrust efficiency in overexpanded nozzles has been analyzed. In addition, the influence of wall cooling on the free shock-induced separation has been investigated through the analysis of wall temperature properties.

The validation of the model was performed by a numerical study of the location of separation, wall pressure and Mach number. The calculations agreed well with the experimental data and the exit jet shape also showed good agreement with shapes from literature for different experiments.

In the case of wall cooling, three (03) wall thermal configurations with different imposed wall temperatures T_w were analyzed. The first configuration i.e. an isothermal divergent wall was used to analyze the effect of wall temperature on the free shock-induced separation while the other two (02) were used to study the best wall cooling configuration to be employed to achieve the best thrust efficiency possible.

By analyzing wall temperature properties, it has been observed that the wall temperature is directly linked to the separation location. Lowering the wall temperature enhances the resistance of the flow to the separation of the boundary layer. It has been shown that the separation location moves further downstream with decrease in wall temperature resulting in a decrease in the size of the recirculation zone. Compared to all thermal cases, Case 1 i.e. case with the lowest wall temperature presented the highest thrust coefficient.

In the wall cooling position analysis, configuration C i.e. cooling from the nozzle throat presented the highest thrust efficiency with an increase in thrust coefficient of 0.039% compared to the baseline configuration and a relative difference of +0.14% when compared to configuration B. The separation location for Case 1 (in Config.C) was the furthest location downstream in the nozzle's divergent region with an offset of 0.044%.

Conclusion and perspectives

The numerical results also showed that Mach number computed across the centerline is not affected by the thermal conditions on the divergent wall. The effect of the wall temperature is observed in the near wall region of the divergent section of the nozzle.

This thesis provides an analysis of the influence of wall cooling on flow dynamics with respect to flow separation and thrust efficiency. As a future work, the parameters affecting cooling of the nozzle wall can be optimized for given conditions. Heat transfer at the wall has been shown to be useful in controlling flow separation in overexpanded nozzles and based on the analysis of the solutions, better coolant conditions which can give higher cooling efficiency will be proposed.

References

References

- [1] R. Stark and G. Hagemann, Current status of numerical flow prediction for separated nozzle flows, 2nd European Conference for Aerospace Sciences (EUCASS), Brussels, Belgium, July, 2007.
- [2]] Ansys-Fluent, Version 19.2, User Guide, 2018, Pennsylvania, USA.
- [3] G .P. Sutton and O. Biblarz, Rocket Propulsion Element, JOHN WILEY & SONS, 2001.
- [4] J. Östlund: “Flow processes in Rocket Engine Nozzles with Focus on Flow Separation and Side-Loads”, Licentiate Thesis, Royal Institute of Technology TR2002:09, Stockholm, 2002.
- [5] A. MCCABE. Design of a Supersonic Nozzle. The Mechanics of Fluids Department, University of Manchester. Reports and Memoranda No. 3440 March, 1964
- [6] M.R. CHEIKH BOUCHRAYE, A. BENAROUS, Caractérisation de l'écoulement dans un convergent à paroi courbée.
- [7] D. Bershader, An interferometric study of supersonic channel flow. Rev. of Sci. Inst., 20, No. 4, 1949
- [8] J. Östlund and B. Muhammad-Klingmann. Supersonic Flow Separation with Application to Rocket Engine Nozzles. Mech. Rev. 58 (2005), pp. 143–177.
- [9] G. P. Sutton. History of Liquid Propellant Rocket Engine. American Institute of Aeronautics Astronautics, 2006.
- [10] G. Guderley and E. Hantsch. Beste formen für achensymmetrische Überschalldüsen. Zeitschrift für Flugwissenschaften 3 (1955).
- [11] G. V. R. Rao. Exhaust Nozzle Contours for Optimum Thrust. Journal of Jet Propulsion 28 (1958).
- [12] G. V. R. Rao. Approximation of optimum thrust nozzle contour. ARS Journal 30 (1960).
- [13] J. D. Anderson. Modern Compressible Flow with Historical Perspective. 3rd edition. McGraw-Hill, 2003.
- [14] Robert d. Zucker, Oscar Biblarz, Fundamentals Of Gas Dynamics, JOHN WILEY & SONS, 2002

References

- [15] Mahfoudi El-Ahcene, 2014, «Contribution à l'étude des profils de tuyères en écoulements supersoniques visqueux par la méthode des volumes finis», Thèse de doctorat d'état, en Énergétique, Département de la mécanique, Université Constantine 1, Constantine, Algérie.
- [16] J. DELERY, Aérodynamique interne, tuyères et arrières corps, Département Aérothermodynamique, E.N.S.A.E, 1989
- [17] M. Summerfield, C. Foster, W. Swan: "Flow Separation in Overexpanded Supersonic Exhaust Nozzles", Jet Propulsion, Vol. 24, No. 9, September-October 1954
- [18] L. Nave, G. Coffey: "Sea Level Side Loads in High-Area-Ratio Rocket Engines", AIAA 1973-1284
- [19] Frey M. and Hagemann, G. Status of flow separation prediction in rocket nozzles, 34th AIAA/ASME/SAE/ASEE, Joint Propulsion Conference & Exhibit (July 13-15, 1998, Cleveland, OH), AIAA Paper 98-3619
- [20] R. Lárusson. Modal Analysis of Supersonic Flow Separation in Nozzles, CHALMERS University of Technology, Gothenburg, Sweden 2017.
- [21] Frey M. et al.: Joint European Effort Towards Advanced Rocket Thrust Chamber Technology, 6th International Conference on Launcher Technologies, 2005
- [22] L. Torngren: "Correlation Between Outer Flow and Internal Nozzle Pressure Fluctuations", Proceedings of the 4th European Symposium on Aerothermodynamics for Space Applications, October 2001, Capua, Italy, ESA SP-487
- [23] A. T. Nguyen, H. Deniau, S. Girard, T. Alziary de Roquefort: "Wall Pressure Fluctuations in an Overexpanded Rocket Nozzle", AIAA 2002-4001
- [24] Frey M., Stark R., Ciezki H., Quessard F., and Kwan W., "Subscale Nozzle Testing at the P6.2 Test Stand", AIAA Paper 2000-3777, 2000.
- [25] H. Kronmüller, K. Schäfer, H. Zimmermann, R. Stark: "Cold Gas Subscale Test Facility P6.2 at DLR Lampoldshausen", 6th Symposium on Propulsion for Space Transportation of the 21st century, May 2002, Versailles, France
- [26] P. Reijasse, L. Morzenski, D. Blacodon, J. Birkemeyer: "Flow Separation Experimental Analysis in Overexpanded Subscale Rocket-Nozzles", AIAA 2001-3556
- [27] P. Reijasse, L. Morzenski, P. Naudin, F. Généau: "Fluctuating Side-Load Measurements in Overexpanded Subscale Rocket-Nozzles", AIAA 2001-3557

References

- [28] S. Girard, T. Alziary de Roquefort : "Study of Flow Separation in Overexpanded Rocket nozzles", 4th French-Russian-Italian-Uzbek Workshop, July 1997, Marseille, France
- [29] P. Reijasse, B. Corbel, D. Soulevant: "Unsteadiness and Asymmetry of Shock-Induced Separation in a Planar Two-Dimensional Nozzle: A Flow Description", AIAA 1999-3694
- [30] Boccaletto, L., Reijasse, P. and Dussauge, J.P., "Dynamic behavior of a separation oblique shock during film cooling transient injection," 37th Fluid Dynamics Conference and Exhibit, Hyatt Regency Miami, Miami, FL, June 25-27, 2007, AIAA 2007-4003.
- [31] Boccaletto, L., Reijasse, P. and Dussauge, J.P., "Influence of film cooling injection on transient side loads," 43rd AIAA/ASME/SAE/ASEE Joint Propulsion Conference & Exhibit, Cincinnati, OH, July 8-11, 2007. AIAA 2007-5474.
- [32] Coponet, D., "Influence du film de refroidissement sur le décollement et les charges latérales dans les tuyères propulsives. Soufflerie R2Ch," (Influence of a film cooling on flow separation and side loads in propulsive nozzles. R2Ch wind tunnel). Onera report, 2/10515 DAFE, October 2006.
- [33] Reijasse, P. and Boccaletto, L. Film cooling mass flow rate influence on a separation shock in an axisymmetric nozzle, IUTAM Symposium on Unsteady Separated Flows and their Control, Corfu, Greece, June 18-22, 2007
- [34] Reijasse, P. and Boccaletto, L., "Nozzle side loads due to non-symmetrical film cooling," 43rd AIAA/ASME/SAE/ASEE Joint Propulsion Conference & Exhibit, Cincinnati, OH, July 8-11, 2007
- [35] Reijasse, P. and Boccaletto, L., "Influence of film cooling on nozzle side loads," 46th AIAA Aerospace Sciences Meeting and Exhibit, Reno, NV, Jan 7-10, 2008.
- [36] J. Mattsson (changed name to Östlund 1999), U. Högman, L. Torngren: "A Sub Scale Test Programme on Investigation of Flow Separation and Side Loads in Rocket Nozzles", European Symposium on Aerothermodynamics for Space Vehicles, November 1998, Noordwijk, Netherlands, ESA SP-426

References

- [37] Kwan, W. Stark, R.: Flow separation phenomena in subscale rocket nozzles. AIAA 2002-4229, 38th AIAA/ASME/SAE/ASEE Joint Propulsion Conference and Exhibit (2002)
- [38] M. Frey, G. Hagemann: "Status of Flow Separation Prediction in Rocket Nozzles", AIAA 1998-3619
- [39] Stark, R., Wagner, B.: Experimental study of boundary layer separation in truncated ideal contour nozzles. Shock Waves, present Issue (2009)
- [40] Gross A., Haidn O., Stark R., Zeiss W., Weber C., and Weiland C., "Experimental and Numerical Investigation of Heat Loads in Separated Nozzle Flow", AIAA Paper 2001-3682, 2001.
- [41] Stark R. and Wagner B. Mach disk shape in truncated ideal contour nozzles. 26th International Symposium on Shock Waves, Göttingen, 15-20th July, Germany, 2007
- [42] Lawrence, R.A.: Symmetrical and unsymmetrical flow separation in supersonic nozzles. Research Report Number 67-1, Southern Methodist University (1967)
- [43] Verma, S.B.: Shock unsteadiness in a thrust optimized parabolic nozzle. Shock Waves (2009, this issue)
- [44] Stark, R., Kwan, W., Quessard, F., Hagemann, G., Terhardt .M. Rocket nozzle cold gas test campaigns for plume investigations. In: Proceeding of the Fourth European Symposium on Aerothermodynamics for Space Vehicles (2001)
- [45] Nave, L.H., Coffey, G.A.: Sea-level side loads in high-area-ratio rocket engines. AIAA Paper 73-1284 (1973)
- [46] Tomita, T., Sakamoto, H., Onodera, T., Sasaki, M., Takahashi, M., Tamura, H., Watanabe, Y.: Experimental evaluation of side-loads characteristics on TP, CTP and TO nozzles. AIAA Paper, 04-3678 (2004)
- [47] Nasuti F., Onofri M. and Pietropoli E.: Prediction of Shock Generated Vortices in Rocket Nozzles, AIAA Paper 2005-317, 2005
- [48] Pilinski C. and Nebbache A.: Flow Separation in a Truncated Ideal Contour Nozzle, Journal of Turbulence, Vol. 20, No. 3, 2004
- [49] P. Reijasse, F. Bouvier, P. Serval: "Experimental and Numerical Investigation of the Cap-Shock Structure in Overexpanded Thrust-Optimized Nozzles", West-East High Speed Flow Field 2002 (WEHSFF) Conference, April 2002, Marseille, France

References

- [50] P. Servel, Modelisation du décollement avec et sans film de refroidissement dans la tuyère a choc interne testée d R2Ch. Programme FSCD, Onera RT 63/03584 DAFE, April 2001
- [51] M. Frey and G. Hagemann, Flow Separation and Side-Loads in Rocket Nozzles, AIAA 99-2815, 1999
- [52] P. Reijasse, P. Servel and R. Hallard, Synthesis of 1998 Onera Works in the FSCD Working Group, Onera RTS 49/4361AY, October 1999
- [53] J. Östlund and M. Varan, Assessment of turbulence models in over-expanded rocket nozzle flow simulations, AIAA 99-2583, 1999
- [54] Reijasse, P. and Boccaletto, L Nozzle Flow Separation with Film Cooling.
- [55] Deck, S. and Thépot, R., P. "ATAC: Simulations numériques avancées de type DES des charges latérales instationnaires en régime end-effet ainsi qu'en présence d'un film d'injection sur des configurations de tuyères optimisées en poussée (ATAC: Advanced DES numerical simulations of unsteady side loads in end-effect regime and with the presence of a wall film on thrust optimized nozzle configurations)", ONERA RTS 1/09791 DAFE/DAAP, November 2006.
- [56] Servel, P. "Synthèse des travaux numériques 2002-2003 sur l'écoulement d'une tuyère optimisée en sur-détente avec influence d'un film pariétal (Synthesis 2002-2003 of numerical works on thrust-optimized nozzle flow in overexpansion regime and with the influence of a wall film)", ONERA RT 1/07572 DAFE, November 2004.
- [57] P. Vuillermoz, H. Lambaré, A. Enzian, P. Steinfeld, L. Lequette, Computational Flow Simulations of Overexpanded Nozzle Flow Field including Unsteady Effects
- [58] F. M. White. Fluid Mechanics, 5th edition, McGraw-Hill, New York, 2003.
- [59] P. Spalart and S. Allmaras. "A one-equation turbulence model for aerodynamic flows". Technical Report AIAA-92-0439. American Institute of Aeronautics and Astronautics. 1992.
- [60] H K Versteeg and W Malalasekera. An Introduction to Computational Fluid 2nd Dynamics, Finite Volume Method, edition , Pearson Education Limited, Edinburgh, England, 2007.
- [61] ANSYS Fluent v19R2 Theory Guide, 2019.

References

- [62] George P. Sutton, Oscar Biblarz - Rocket Propulsion Elements-John Wiley & Sons (2001).
- [63] J. M. Weiss and W. A. Smith. "Preconditioning Applied to Variable and Constant Density Flows". AIAA Journal. 33(11). 2050–2057. November 1995.
- [64] P. L. Roe. "Characteristic based schemes for the Euler equations". Annual Review of Fluid Mechanics. 18. 337–365. 1986
- [65] Lionel Meister, Yves Burtschell & David E. Zeitoun- Etude numérique d'un écoulement réactif dans une tuyère surdétendue: influence de la température de paroi et de l'altitude. 16^{ème} Congrès Français de Mécanique 2003.